UNIVERSITY OF CAPE TOWN
IYUNIVESITHI YASEKAPA • UNIVERSITEIT VAN KAAPSTAD

FACULTY OF ENGINEERING AND THE BUILT ENVIRONMENT

Department of Civil Engineering

Investigated Physical/Strength Properties and Elastic Constants of Fimbul Granular Ice Applied to Ice Cliff Stability Analysis

GEOTECHNICAL ENGINEERING
UNIVERSITY OF CAPE TOWN

Author : Jonathan Arthur Olivu Econi
Supervisor : Prof. Denis Kalumba
Co-supervisor : Dr Keith MacHutchon
Co-supervisor : Prof. Sebastian Skatulla
Co-supervisor : Dr Reuben Govender

A thesis submitted in partial fulfilment of the requirement for award of the degree of Master of Science in Civil Engineering Specialising in Geotechnical Engineering at the University of Cape Town

February 2024

Plagiarism Declaration

1. I know the meaning of plagiarism and declare that all the work in this document, save for that which is properly acknowledged, is my own.

2. I have used the Harvard convention for citation and referencing. Each significant contribution to and quotation in this report from the work or works of the other people has been attributed and has been cited and referenced.

3. This dissertation has been submitted to the Turnitin module.

4. I confirm that my supervisors have seen my report and any concerns have been resolved with my supervisors.

Signature: Signed by candidate Date: 10/02/2024

Student Name: Jonathan Arthur Olivu Econi

Dedication

TO

My dear mom and dad, **Mrs. Lydia Osoa Olivu** and **Eng. Charles Olivu Assedri**, their unwavering love and dedication to both my brother and I are the building blocks for the person I am today.

Acknowledgements

This dissertation stands as a culmination of collaborative efforts and unwavering support from the following individuals who have played pivotal roles in its realization.

I would like to begin by expressing my deepest gratitude to the Almighty God, without whose guidance and blessings, this journey would not have been possible.

I owe a profound debt of gratitude to my principle supervisor, Prof. Denis Kalumba, for his invaluable guidance, mentorship, and the countless hours invested in shaping my research. His expertise and insightful feedback have been instrumental in moulding the progression of my dissertation.

I would also like to extend a heartfelt appreciation to my co-supervisors, Dr Keith MacHutchon, Prof. Sebastian Skatulla, and Dr Rueben Govender. Their guidance and support added sufficient depth to my research, enhancing its overall quality. The constructive criticism and intellectual guidance received has been invaluable.

I am also grateful to my colleagues, Michael Katsoulis for field work support in Antarctica, then Steven McEwen, Nadia Mahomed, Kamva Tabata, and Gerald Otim for their aid as lab partners through the gruelling work in the cold polar lab. Their collective support made the challenges of this research more manageable and enjoyable. In addition to them, special appreciation goes to Mr Nooredien Hassen, Mr Elvino Witbooi, and Mr Christopher Ceasar of the Civil Engineering Laboratory who offered invaluable assistance throughout the course of my research.

Last but not least, I want to express my appreciation to Ayiko Austin, my brother, and all the friends who supported me in various ways throughout this journey. The fun times we spent in Cape Town and collective encouragement were essential in keeping me emotionally rooted, focused, and motivated.

This thesis stands as a testament to the collective efforts of these remarkable individuals who have contributed to my academic success. Thank you for being a part of this monumental chapter of my life.

Abstract

During the 2020-2021 South African National Antarctic Programme Antarctic resupply voyage, a Ground Penetrating Radar (GPR) survey was conducted on the Fimbul ice shelf edge to determine a safe cargo offloading zone from the SA Agulhas II ship. The survey showed subsurface cracks which created concerns of shelf failure, risking the lives of crew and the ship stationed at the bottom of the cliff. To assess the risk of failure, this study was carried out to quantify the stability of the vertical cliff. A slope stability analysis model was required to achieve this, which in turn needed inputs such as cliff geometry and ice material properties. Therefore, laboratory tests to obtain these properties preceded the cliff modelling.

Ice cores were retrieved from the shelf, and these were observed to be granular in structure, with different grainsizes and ice lenses. The analysis began with a core characterisation based on the grainsize percentages, ice lens concentrations, and due to ice's relationship to rock, Rock Quality Designation (RQD) of the cores. The grainsize segmentation was fine, medium, and large grained, with medium grained being the most abundant in the cores. The ice lens concentrations showed areas on the ice shelf with high meltwater which were to be avoided.

The physical properties needed were density, elastic modulus, and Poisson's ratio. The mass/volume method was used to obtain an average density of 569.9±157.7kg/m^3. The elastic modulus and Poisson's ratio were both tested using ultrasonic methods to give 1.66±0.87GPa and 0.37±0.06 respectively. Each of the values were comparable to values mentioned in literature with the granular ice lying between the stiffnesses of snow ice structures and crystalline ice.

The strength value tested was Uniaxial Compressive Strength (UCS), with shear strength and tensile strength determined afterwards. The UCS tests gave a value of 0.9±0.27MPa. The compression was carried out at a strain rate of $10^{-4.3}s^{-1}$ for ductile failure. Shear strength was then determined using the Rock Mass Rating (RMR) method, giving cohesion and friction angle readings of 0.25MPa and 30°. The shear strength was then calculated to 0.77MPa. The tensile strength was equal to the ice bond strength, which was equal to the cohesion value of 0.25MPa.

Modelling was then embarked for a base scenario, horizontal crack variation, and vertical crack depth variation scenario. The base critical Factor of Safety (FS) was 5.56. Failure occurred in both tension and shear, through the Mohr Coulomb failure criterion. In the horizontal variation, the critical crack zone lay between 9 - 20m away from the shelf edge with the lowest FS of 4.24 at 13m. The failure types observed were toppling failure, planar failure, crumbling of the overhanging part of the ice. Finally, the increasing crack depth at the critical horizontal location led to decrease in FS.

The scenarios output FS values showing that the ice shelf cliff is safe. Despite this, the models run were an oversimplification of the entire shelf with a number of factors assumed due to the unavailability of data. To provide a detailed analysis of the entire ice shelf, a thorough survey of the entire shelf would need to be carried out to provide accurate layering data, precise material properties at depth, actual crack locations and dimensions on the shelf edge.

Table of Contents

List of Figures

List of Tables

Abbreviations

asl	Above sea level
CSIR	Council of Scientific and Industrial Research
DMT	Double Microtoming Technique
EAIS	East Antarctic Ice Sheet
FDM	Finite Difference Method
FEA	Finite Element Analysis
FEM	Finite Element Method
FS	Factor of Safety
GPR	Ground Penetration Radar
GPS	Global Positioning System
GSI	Geological Strength Index
$HiDEM_{be}$	Helsinki Discrete Element Model
HV	Horizontal Variation
LE	Limiting Equilibrium
MCC	Modified Cam Clay
MICI	Marine Ice Cliff Instability
MISI	Marine Ice Sheet Instability
msl	Mean sea level
PERG	Polar Engineering Research Group
PLT	Point Load Test
PVC	Poly Vinyl Chloride
P wave	Pressure wave
RMi	Rock Mass Index
RMR	Rock Mass Rating
RMR_{basic}	Basic Rock Mass Rating
RQD	Rock Quality Designation
SANAE	South African National Antarctic Expedition
SANAP	South African National Antarctic Programme
SEM	Scanning Electron Microscopy
SMR	Slope Mass Rating
SRF	Shear Reduction Factor
S wave	Shear wave
UCS	Uniaxial Compressive Strength
UCT	University of Cape Town
VV	Vertical Variation
WAIS	West Antarctic Ice Sheet
WIS	Wilkins Ice Shelf

Symbols

ϕ	°	Angle of friction
A	m^2	Area
D_{av}	mm & mm^2	Average grain size
c	kPa / MPa	Cohesion
ρ	kg/m^3	Density
ρ_m	kg/m^3	Density of material
D	mm	Diameter
ψ_p	°	Dip angle
μ	-	Friction coefficient
H	m / mm	Height
L	m/ mm	Length
m	kg	Mass
m_{air}	kg	Mass in air
m_{liquid}	kg	Mass in liquid
N	kN	Normal force
σ	kPa / MPa	Normal stress / Compressive stress
n	-	Number of grains
ν	-	Poisson's ratio
h_i	mm	Platen initial height
h_f	mm	Platen final height
M	ms^{-1}	Pressure wave modulus
T	kN	Shear force
G	GPa	Shear modulus
τ	kPa / MPa	Shear stress
ψ_f	°	Slope face angle
ψs	°	Surface angle
t	s	Time
γ	kN/m^3	Unit weight
V	ms^{-1}	Velocity
V_p	ms^{-1}	Velocity – P wave
V_s	ms^{-1}	Velocity - S wave
v	m^3	Volume
U_p	kN	Water force (plane)
U_c	kN	Water force (crack)
W	kN	Weight of block
E	GPa	Young's / Elastic modulus

1 Introduction

1.1 Area of study

Antarctica is the fifth largest Southernmost continent and was the last continent to be discovered on earth, containing about 10% of the earth's land coverage. It covers an approximate area of 14.2 million km^2 with 26.5 million km^3 of ice, a volume capable of raising the global sea level by about 60m (Kennicutt *et al.*, 2014). This volume of ice is about 90% of the all the ice on earth and harbours about 70% - 80% of the world's freshwater reserves (Campbell & Claridge, 1987). Together with the freshwater reserves on the continent, Antarctica also regulates the global climatic conditions through influences on oceanic currents, recovery of atmospheric ozone, and uptake of CO_2 by surrounding sea ice, to mention but a few (Kennicutt *et al.*, 2014).

Due to the continent's significance to the global ecosystems (Turner *et al.*, 2014), the Antarctic treaty was signed in 1959 by twelve countries and about thirty-eight others over time. The treaty prevented countries from carrying out military activities, waste disposal, mineral mining and other detrimental activities that would degrade the natural water and ecological resources on the continent (Hanessian, 1960). These agreements allowed for the development and rehabilitation of research bases by a number of countries which include China, South Korea, India, Belgium, USA, UK, and Germany among others. Together with the research bases, counties like South Korea, Japan and South Africa joined the treaty and have obtained sea vessels and ships capable of traversing the icy waters for voyages to the continent (Kennicutt *et al.*, 2014). An example is the SA Agulhas II, an ice-breaker ship, which uses its engine power to mount onto sea ice and its weight to break through the ice during forward traversal. South Africa is currently responsible for the SANAE IV Research Base at 71°40'22"S, 2°50'26"W on the continent. The research base is part of the South African National Antarctic Program (SANAP) that oversees research activities taking place on the Fimbul Ice Shelf and surrounding waters.

98% of the Antarctic continent is covered in ice and 40% of the ice cover is part of ice shelves as illustrated in Figure 1-1. These are masses of ice from inland ice streams, outlet glaciers, and snow, all floating on ocean water (Doake, 2001). Ice shelves in the Antarctic and Arctic areas have become a significant topic of research in recent years. This has partly been due to their impact on global issues such climate change and also the devasting effects that their failures could have on not only the climate, but also global sea levels and freshwater reserves.

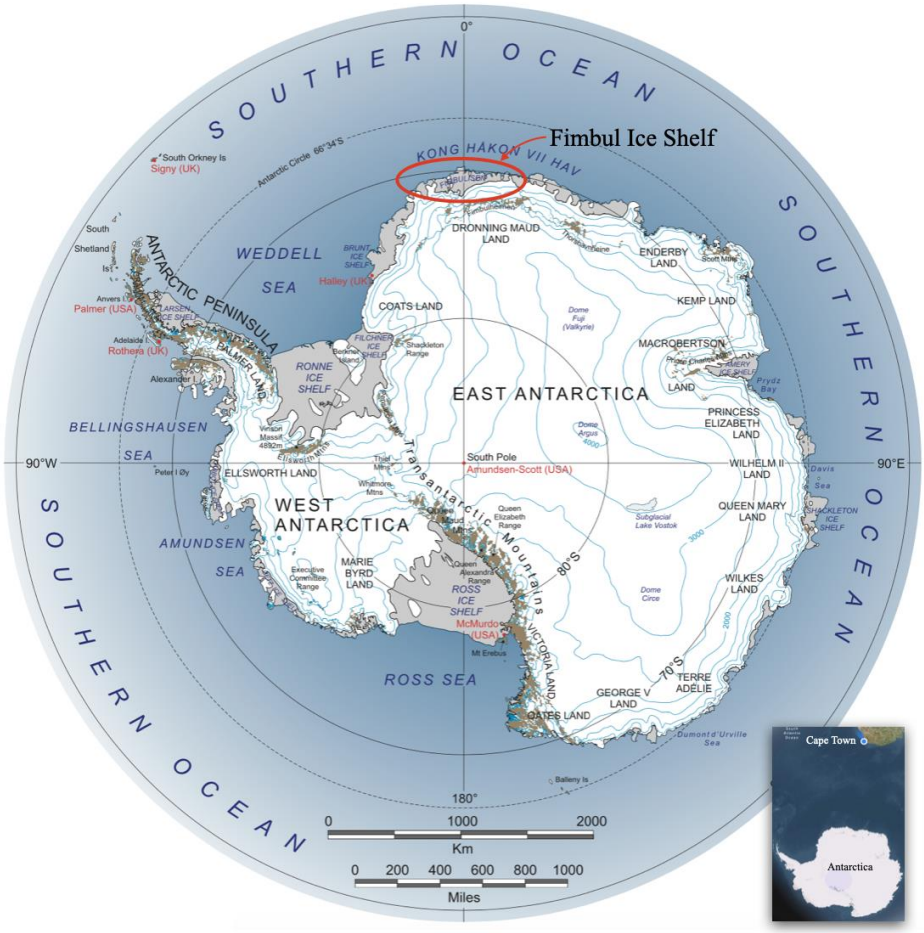

Figure 1-1: Geodetic Map of Antarctica showing the Fimbul Ice Shelf (British Antarctic Survey, 2023)

The ice shelves are surrounded by cyclic sea ice which grows during winter months, vastly expanding over the ocean surface, and retreats in summer when the increase in temperature causes melting (Nøst, 2004). Sea ice by the Fimbul ice shelf is no exception to the cyclic expansion process, making the ice shelf only accessible during the summer months after the sea ice melts. Due to this, the SA Agulhas II carries out annual resupply voyages during the summer months from Cape Town to the ice shelf. It offloads supplies onto the Fimbul ice shelf at 70º15'26.85"S 2º42'0.38"W, on an ice cliff with a freeboard of about 28m above sea level (asl). The voyage resupplies the research base with fuel, food, manpower and other necessities that were depleted during the previous year and carries back waste and empty containers to Cape Town where they are treated, disposed, or recycled. The supplies are transported back and forth over the ice shelf to the research base using CAT Challenger trucks and ice sleds.

1.2 Research background

During previous annual voyages to resupply the SANAE IV research base, the presence of cracks on the Fimbul ice shelf had always been a significant issue. The cracks on the shelf cliff were often covered by a layer of snow, making them invisible to personnel (Luka & Keith, 2021). This caused health and safety concerns with recorded cases of crew members falling into unseen cracks and occasional equipment damages. To mitigate this, a ground penetration radar (GPR) survey was carried out at the offloading area to identify the cracks as seen in Figure 1-2. The severity, frequency, and orientation of the cracks intensified the concerns to potential cliff failure which would risk the lives of crew members and damage the ship docked at the cliff bottom.

These concerns therefore warranted the need for a stability analysis of the cliff to quantify its stability. In addition to this, there was a need to understand the material comprised within the cliff and factors causing the formation of the cracks. Furthermore, these concerns also necessitated an assessment of the effect of global climate change on cliff and the effects it may have, considering the thermodynamic nature of ice.

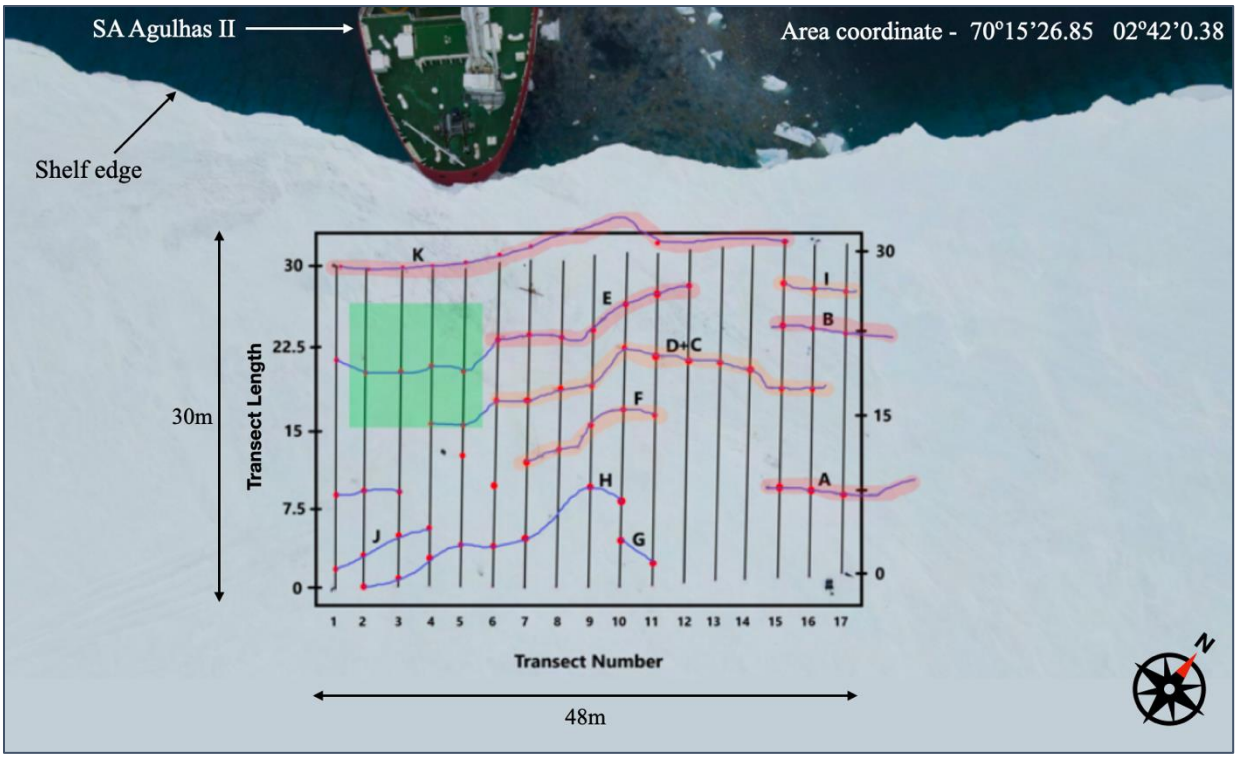

Figure 1-2: Crack mapping during 2020-2021 Antarctic voyage (Luka & Keith, 2021).

1.3 Research objectives

The main objective was to determine and quantify the stability of the ice cliff in terms of a factor of safety (FS). This was achieved through the application of material properties and cracks to a finite element (FE) slope stability model. The method conceptualised to investigate the cliff stability, firstly, involved an analysis of the microscale features within the cliff material. Second to this was testing and determination of some of the macro scale physical properties of the ice, specifically the properties with a significant influence on the deformation behaviour of the material. Third was the investigation of strength properties of the material and finally, fourth was application of all determined properties into a slope stability analysis model.

1.4 Scope of the study

The slope stability analysis was limited to an area within 100m from the shelf cliff face and 200m wide at the offloading site coordinates. This boundary was used as the material sampling area because locations of health and safety hazards were identified using a prior GPR survey. Unavailability of crack location information outside the demarked area increased health and safety risks and was therefore avoided. Sampling within the area involved coring of 1m deep ice cores. Drilling of deeper cores was deemed unsafe and speculated to increase cliff instability due to close proximity of the drill site to the cliff face and ease of crack propagation in ice between discontinuities.

With no ice testing standard published, methods used for testing ice samples were informed from published literature. Equipment available and used for the tests included a GCTS compression machine, Pundit ultrasound, and various mass and length measuring equipment.

1.5 Thesis overview

This chapter briefly introduced the study area, highlighted the problem in need of investigation, and mentioned limits within the study scope. Following this, chapter 2 detailed key takeaways from literature, beginning with an emphasis on ice cliff instability and related phenomena, then the material information required to assess the cliff instability. This included micro scale properties, macro scale properties and strength parameters of the material.

Analysis processes carried through by published authors were then used as inspiration for the methods adopted and described in chapter 3. The chapter detailed procedures used to obtain the material properties first, and then the slope stability analysis using acquired material properties as input parameters. Chapter 4 then outlined the results obtained from the methods, as well as in-depth discussions and analysis of the results. The study was then concluded in chapter 5 with the key takeaways and recommendations at the end of the chapter.

2 Literature Review

This chapter involves a literature review of ice as a material, ice structures such as ice shelves and cliffs, and analysis methods used to access such structures. These 3 segments were used to divide this chapter into 3 parts namely: Part I, Part II, and Part III.

Part I reviewed studies about the micro and macro structures of ice as a material. These were in terms of ice morphology, the physical properties, and strength properties of ice. The specific properties, testing methods, and results obtained by various authors were detailed in this part.

Part II then increased the scale to ice shelves and ice cliffs. This part detailed the formation of the structures, causes of failure, and failure mechanisms experienced by them. It was then concluded by reviewing the relationship between ice and known geomaterials to aid in further analysis of ice.

Part III followed this by reviewing the methods used to model the ice and geomaterial structures. The part was then concluded by reviewing the software used to carry out the modelling, and material classification systems to obtain material parameters.

The chapter was then finally concluded by a chapter summary which highlighted the gap in literature and key aspects from each of the parts.

Part I: Ice Material Properties

2.1 Ice morphology

Morphology in this Section was defined as the form and structure of materials, which was predominantly ice in this study. Materials in nature are comprised of different chemical and physical elements that constitute a large innate variability that makes prediction of behaviour difficult (Park & West, 2001). These behaviours are mechanically controlled by a wide variety of characteristics like mineral composition, matrix types, physical and strength properties, scale, to mention but a few (Pappalardo & Mineo, 2022). This morphology Section therefore contains a review of studies on the types of ice and structures of Antarctic ice following Jaeger *et al.* (2009) description of morphology as the smallest scale by which mechanical properties are studied. The study then sets a basis for the determination of physical and mechanical properties later in the Chapter.

2.1.1 Types of Ice

Ice is formed through the bonding of water molecules comprised of hydrogen and oxygen atoms. Atoms in a water molecule, comprised of one oxygen and two hydrogen atoms (H_2O), bond to

one another using covalent bonding. The hydrogen atoms covalently bonded to a single oxygen atom further bond with neighbouring oxygen atoms in water molecules using hydrogen bonds. This puts a hydrogen atom between two oxygen atoms, with one bonded with a shorter and stronger covalent bond while another with a weaker and longer hydrogen bond (Schulson & Duval, 2009).

Ice is a solid substance with a definite shape that has been investigated to exist in two different types namely: crystalline ice and amorphous ice (Petrovic, 2003). There have been about 20 states of crystalline ice and 2 amorphous ice families discovered (Rosu-Finsen *et al.*, 2023). Crystalline ice is the primary form of ice found in nature formed through the freezing of water under various temperature and pressure combinations (Sinha & Shokr, 2015). Alternatively, amorphous ice, which is the least common of the two, was mainly investigated to originate through local melting. The states in which amorphous ice exist include low density amorphous ice, medium density amorphous ice, high density amorphous ice, expanded high density amorphous ice, and very high density amorphous ice. Evidenced by their names, amorphous ice states are differentiated using their densities. The methods used to obtain these amorphous states include vapour disposition, compression of crystalline ice at low temperatures, heating high density amorphous ice at high pressure, and ball milling to mention but a few (Rosu-Finsen *et al.*, 2023).

In crystalline ice, water molecules bond to form hexagonal crystalline structures. The hexagonal crystal structure is comprised of hydrogen and oxygen atoms bonded together in layered lattices by both covalent and hydrogen bonds. Hexagonal symmetry in the ice molecules can be seen when the oxygen atoms are connected, hence showing the O-O bond paths. The angle between O-O atoms in the hexagonal lattice is 109.47°, the distance between the oxygen atoms is 0.276nm, and the distance between oxygen and hydrogen atoms is 0.0985nm (Randhawa, 2018).

Ice formed naturally from water at 0°C and at atmospheric pressure exists in a crystalline form called Ih which is the most common type of ice. The formation is characterised by a volume increase. Ih is hexagonal in nature with characteristics depending on the conditions of formation, thermal and deformation history of the ice (Cole, 2001). Phase Ih, also known as ordinary ice, exists at temperatures of 0 to -80°C according to Sinha & Shokr (2015) which encapsulates the Antarctic ice being investigated. The various phases of ice formation in relation to temperature and pressure can be seen in Figure 2-1.

To measure the size and crystal texture of ice crystals, thin section analysis was used by Wang, Q. *et al.* (2018), Sinha & Shokr (2015), and Shazly *et al.* (2009). During this method, thin sections of ice were cut to about 1mm and placed between cross polarised paper to allow passage of white light in a single direction. This was made possible due to the translucent nature of ice that does not always allow light to penetrate in a single direction. The method was used to determine the orientation of the crystals' crystallographic axis (c-axis), which can be defined as the axis normal to the basal plane of a single crystal (Shazly *et al.*, 2009) as observed later in Figure 2-2, where light penetrates the crystal in a straight line.

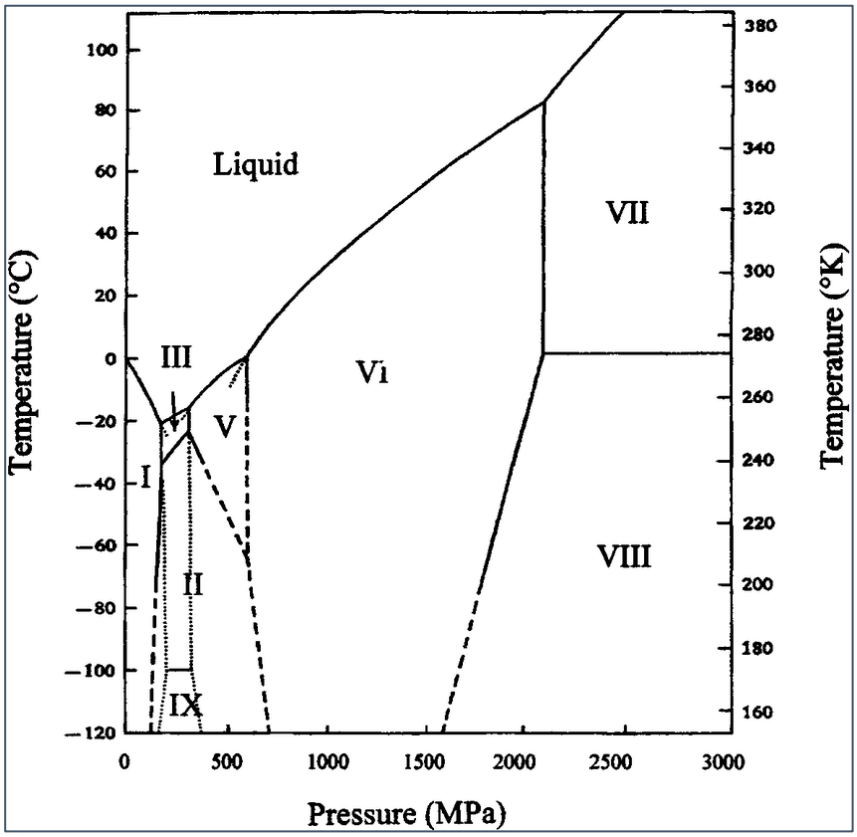

Figure 2-1: Phase diagram of ice (Sinha & Shokr, 2015)

2.1.2 Structure of Antarctic ice

In Antarctica, most of the ice above ground is formed from the accumulation and compression of snow in the area. Water vapour in the atmosphere at temperatures below 0°C freeze into small nuclei on which more water vapour molecules freeze, collectively forming a snow crystal (Libbrecht, 2001). When the snow crystals gain sufficient mass, they begin to fall towards the ground causing snow falls which accumulate over years. As snow falls per year on the ice shelves, past layers of snow get layered and compressed by the new snow (Wang, E. *et al.*, 2021).

As new snow falls, the top layer of the ice settles in a granular matrix due to the particulate nature of snow. After the addition of more snow and pressure, granular snow bonds melt and refreeze through a process called sintering (White & McCallum, 2018). This process allows for the formation of columnar ice at the lower levels of the shelf. Cole (2001) defines granular ice as snow ice formed with deposition of snow and the flooding and freezing of the snow. They also define columnar ice as plate formed ice formed in stable conditions like standing water bodies, but in this case, snow under compression at great depth and high overburden pressures. Columnar ice is divided into three main types based on the different orientations of the c-axes namely S1, S2, and S3, with all found underlaying granular ice. S1 ice have c-axes parallel to the long axis of the columnar grains, S2 have random orientations of the c-axes within a plane and S3 have c-axes aligned with the plane (Schulson, 2001). Granular ice, with the type T1, was

found on the top of columnar ice on icebergs, ice shelves, polar glaciers, and ice islands. Throughout the rest of this report, columnar ice at the bottom of granular ice was referred to as solid ice.

Solid ice, with the more defined crystal structure and packing, is polycrystalline in nature. A purely random orientation of crystals gives rise to the anisotropic mechanical behaviour of the ice (Cole, 2001). This highlights the effect of ice microstructure on its physical and mechanical properties. Cole (2001) mentioned that ice can be modelled as elastic, anelastic, and viscous depending on the type and structure of the ice. More detailed models by Li *et al.* (2018) carry out tensile and compression modelling, taking ice as a viscoelastic material.

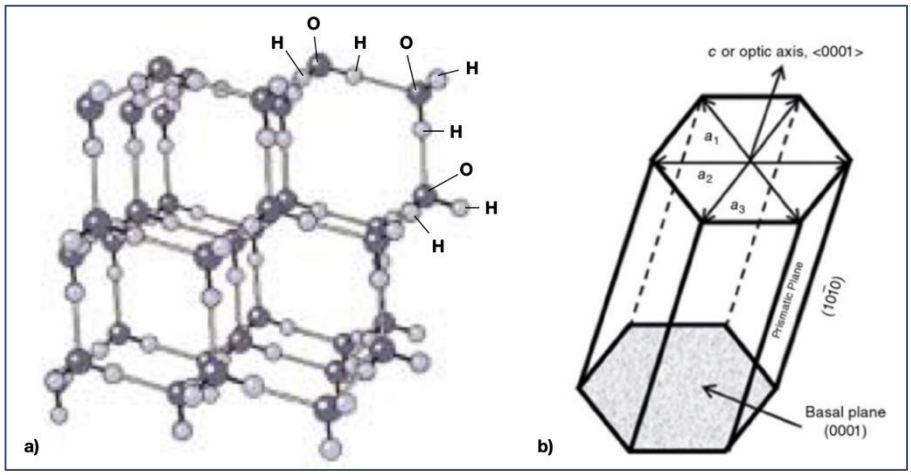

Figure 2-2: **a** Hexagonal ice crystals (Libbrecht, 2001); **b** c-axis schematic (Sinha & Shokr, 2015)

2.2 Ice physical properties

Physical properties can be defined as measurable material parameters involved with material states and behaviours (Burgin, 2016). These properties include bulk density, porosity, elastic modulus, Poisson's ratio, texture, fabric, and salinity to mention but a few (Cole, 2001). Within the scope of the study, this Section describes the physical properties essential for the understanding of ice behaviour and the factors that affect the properties. The chosen parameters were density, elastic modulus, and Poisson's ratio.

2.2.1 Density

The density of pure ice can be defined as the mass per unit volume of the material without impurities like air voids, brine, and others. Density is an essential parameter to be obtained to classify ice types, with it being the main separation factor between amorphous ice forms. This is further emphasised by MacDonell *et al.* (2021), recommending density to be part of the minimum data collected about ice materials.

Despite the importance of density values in ice research and engineering, the measurement of density continues to be notoriously difficult. This has been aggravated by the unavailability of a standard method agreed upon for measuring the parameter (Hutchings *et al.*, 2015). The most documented methods currently used include the use of Archimedes law and the mass/volume ratio method. Archimedes law of buoyancy measures the buoyant force acting on a body and involves reading of an object's weight when suspended in air versus when suspended in a liquid of known density. The equation used to obtain the density of samples using this method is Equation 2-1. The most common liquid used for the test is water and it should be noted that ice is less dense than water, hence its floatation on the liquid. However, Pustogvar & Kulyakhtin (2016) carried out Archimedes principle on ice in a cold laboratory at -10ºC and due to the low temperature which would freeze water, the authors used paraffin to carry out the tests.

$$\rho_{ice} = \frac{M_{air}}{M_{air} - M_{liquid}} \rho_{liquid} \qquad \text{Equation 2-1}$$

where M_{air} = mass of ice in air,

M_{liquid} = mass of ice measured when submerged, and

ρ = density.

The mass/volume method was also used to measure ice density. The mass/volume method can be described as the mass measurement of the material divided by its volume measurement. In the method, the mass of a sample is measured using a suitably accurate weighing scale, dimensions of the sample measured to obtain a volume, then the mass divided by volume to give a density value in kg/m^3. This method was carried out in the tests done by Rist *et al.* (2002), Han *et al.* (2015), and Wang, Q. *et al.* (2018). The mass/volume ratio method is the most common method used for density measurements due to its ease of measurement. But despite its ease, the mass/volume method was proven by Pustogvar & Kulyakhtin (2016) not to be the most accurate due to the higher sources of uncertainty. They describe the uncertainty in the methods as the accuracy of devices used to obtain the required measurements.

Hutchings *et al.* (2015) and Pustogvar & Kulyakhtin (2016) provided in depth analysis of more methods used to determine the density of ice samples. Each of them ranked types of density tests carried out with respect to the percentages of error experienced during the tests. The tests investigated by the authors include the mass/volume method, hydrostatic measurement method, solid/liquid method, and the freeboard method. Uncertainties obtained by the authors are seen in Table 2-1.

Table 2-1: Density measurement methods and uncertainties (Pustogvar & Kulyakhtin, 2016)

Method	Description	Uncertainty (%)
Hydrostatic weighting	Archimedes principle measuring weight in air and weight submerged	0.2
Mass/Volume	Ratio of mass of a sample to the volume of the same sample	3.8 – 4.5
Liquid-solid	Measurement of density and volume of ice meltwater and compared to the volume of solid ice	5.0
Freeboard	Using the heights snow above water level and densities of water	30

Various authors carried out density tests on ice and came up with similar results to confirm the values. Masterson (2009) mentions that the density of pure solid ice is 10% less than that of water which is visually shown by floating ice being 90% below the water surface and 10% above water. This was also mentioned by Nøst (2004) and White & McCallum (2018) who quantified the density of solid ice at great depths on the ice shelves as 900kg/m^3 and 920kg/m^3 respectively. On the ice shelves, density increases in depth up to about 100m where the measurements stabilize at about 900kg/m^3 (Rist *et al.*, 2002).

The ice shelves in antarctica exhibit property relations similar to those seen in Figure 2-3 with the density increasing with an increase in depth and a decrease in temperature (Rist *et al.*, 2002). The increase in density with depth can be attributed to snow accumulation that takes place throughout the year in the metamorphism process described later in this report. Snow that falls gets buried by new snow every recurring season which adds an overburden pressure on the current snow layers. The pressure from the atmospheric snow densifies the old snow through a gradual and slow compression, eventually turning it into solid impermeable ice (Rist *et al.*, 2002). This phenomenon also explains the possibilities of the change of ice type due to pressure increases and temperature decreases according to Figure 2-1.

In addition to the relationship between density and depth, a number of other properties depend on the parameter. Firstly, the uniaxial compressive strength (UCS) is dependent on the density of ice with higher densities exhibiting higher strengths. Both Han *et al.* (2015) and White & McCallum (2018) explain the increase of UCS in a power law manner with increase in density, specifically for values lower that 860kg/m^3. The relationship of density and UCS is applicable for snow as well, with the UCS being directly proportional to the density of snow (Wang, E. *et al.*, 2021). Secondly, the authors observed a linear relationship between the density and critical stress intensity required for the initiation and growth of cracks for snow densities above 560kg/m^3 (Rist *et al.*, 2002). Third, ice was also seen to have similar relationship with elastic modulus as

it does with UCS. An increase in the density influenced an increase in the elastic modulus properties of ice (Rist *et al.*, 2002). Fourth, ice was investigated to have an inverse relationship with both temperature and porosity. A decrease in temperature and porosity led to an increase in density and vice versa (Han *et al.*, 2015). With regard to temperature, Randhawa (2018) attributed the increase in density with reduction in temperature to the decrease in distance between oxygen atoms in the ice lattice.

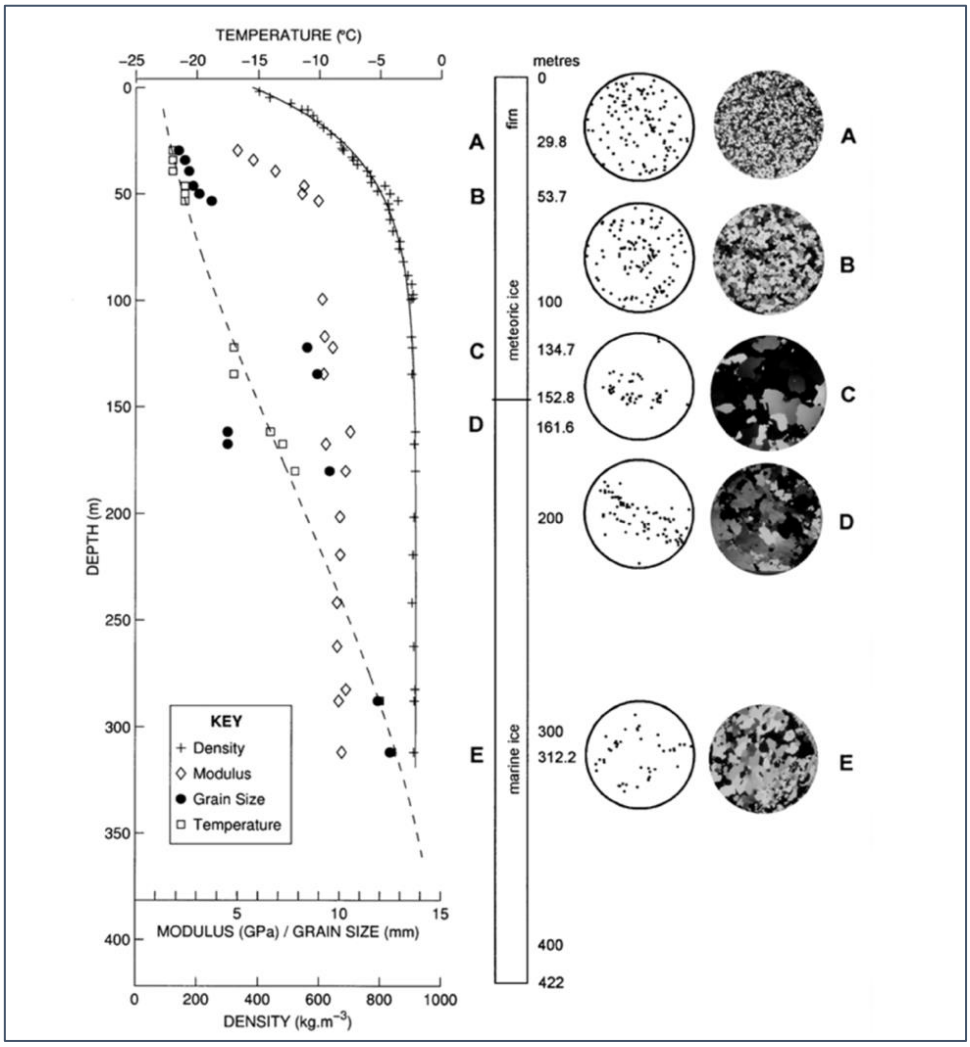

Figure 2-3: Density variation with depth & Crystallographic c-axis orientations (Rist *et al.*, 2002)

2.2.2 Modulus parameters

A number of engineering and scientific applications such as structural member design, vehicle design, and material sciences to mention but a few, require knowledge and an understanding of modulus parameters of materials (Schulson, 2001). Together with the applications mentioned, moduli continue to be a major requirement in material modelling applications (Cole, 2001) and deformation analysis problems (Pappalardo & Mineo, 2022). The frequently required moduli include Young's modulus (E), shear modulus (G), and Poisson's ratio (ν). Young's modulus or

elastic modulus can be defined as a material's ratio of normal stress to normal strain, measuring deformability under applied loads (Brotons *et al.*, 2016), while the shear modulus defined as the ratio of shear stress to shear strain. Poisson's ratio can then be defined as the measurement of the expansion or contraction of a material during loading. This can be interpreted as a ratio of transverse strain to axial strain of the material.

Two methods frequently used to obtain elastic modulus are the static and dynamic testing methods (Brotons *et al.*, 2016). The static methods of testing for *E* involve direct measurement of sample deformations under loading conditions. In the case of *E*, the measurements would involve initial sample height, final sample height, and failure stresses from axial compression tests. Being obtained from axial compression tests, the static tests were further described as destructive tests. In contrast, the dynamic testing methods involve the use of velocity propagation through a sample to determine the moduli (Brotons *et al.*, 2016). This relies on the velocity of sound waves through a sample of interest and was therefore described as a non-destructive. *E* values obtained from the two different methods have been extensively researched and compared against one another giving confident and agreeable results (Cole, 2001). Despite this, dynamically determined *E* values have been consistently found to be higher than those found statically (Pappalardo & Mineo, 2022), with the dynamically determined values diverging greatly for materials with low elastic modulus (Brotons *et al.*, 2016).

The static and dynamic methods have been used across time to measure or determine the moduli mentioned. Firstly, elastic modulus and Poisson's ratio were measured by subjecting ice plates to biaxial bending at a temperature of -10ºC (Petrovic, 2003). Secondly, Rist *et al.* (2002) used acoustic velocity measurements on cylindrical ice core samples to obtain the moduli. Thirdly, Yasui *et al.* (2017) used ultrasonic velocity to examine the properties and finally, Sinha (1989) used matrices, equations and predetermined constants to obtain the values. The tests were carried out by a number of authors on pure ice, sea ice, and different ice shelves in Antarctica, but not primarily the Fimbul ice shelf. Despite the difference in location, values obtained in literature complement each other and fall into similar ranges set by some researchers. Among them, Petrovic (2003) obtained a range of 9.7 – 11.2GPa for Young's modulus and 0.29 – 0.32 for Poisson's ratio from their tests. Yasui *et al.* (2017) also concluded a typical Young's modulus of 9.3GPa, which was a slightly more than the values of 8.7GPa got from their tests. Sinha (1989) carried out the analysis on both granular and pure ice, giving a solid ice elastic modulus of 9.5GPa. The *E* modulus of granular ice was about 6% less than that of ice obtained and a Poisson's ratio of 0.31 was obtained.

Modulus parameters mentioned are affected by a number of factors adversely leading to changes in the deformation characteristics of ice. The major factors include density, grainsizes and material type, temperature, and porosity. Firstly, density was observed to hold a directly proportional linear relationship with elastic modulus (Rist *et al.*, 2002). Material types are also seen to have an effect on the moduli, but not to a substantial degree according to Sinha (1989). A decrease in temperature, however, led to an increase in moduli values with both *E* and *G* increasing by 5%, and Poisson's ratio by 1%. The same inverse relationship was observed

between moduli and porosity. With regard to grain sizes, Schulson (2001) observed that more finely grained ice exhibit higher deformation with decreasing grainsizes. Conversely, more coarsely grained material failed brittlely after minimal strains of 0.02% to 0.04%.

2.3 Ice strength parameters

The strength of a material can be defined as the material's ability to withstand amounts of loading and stress without failure or permanent deformation. In terms of ice, the material strengths, in addition to its behavioural characteristics, provided a detailed understanding of the physical and mechanical limits of the material. This was essential for material application in mathematical and numerical analysis of case studies as material strength properties play a key role in the prediction of breakup, failure, and movements of glaciers and ice shelves over time (Petrovic, 2003). Common material strengths include compressive strength, tensile strength, yield strength, impact strength, shear strength, and fracture strength among others. In this Section, compressive, tensile, shear strengths have been further reviewed due to their direct influence on the analysis of the ice cliff problem.

2.3.1 Uniaxial compression strength

Uniaxial compressive strength (UCS) can be defined as a material's ability to withstand uniaxial loading along the material height without failure or excessive deformation. This strength can be related to the ultimate bearing capacity of ice with significance to the ultimate strength of ice structures like cliffs. An example of this significance was researched by Bassis *et al.* (2021) who explained how the height of ice cliffs was dictated by the strength of ice under marine ice cliff instability (MICI) analysis.

To test the UCS of ice, cylindrical ice core samples were cut to heights of twice the core diameter (2D) and placed under axial loading until failure occurred (Böhm *et al.*, 2022). Two types of failure under compression were observed for the two different types of ice. Solid ice was observed and explained to fail through development of microcracks within the solid ice structure (Cole, 2001) ultimately leading to axial splitting when peak loads were experienced by the samples. In contrast to the solid ice, the rearranging of ice grains was observed in granular ice samples during compression (Kulyakhtin & Høyland, 2014). The values of ice strengths obtained by a number of authors were compiled and summarised into Table 2-2.

2.3.2 Tensile strength

Tensile strength is a material's ability to withstand a stretching load across its cross-sectional area without failure or excessive deformation. This strength carries high significance as it is classified as the critical strength in ice as opposed to compressive strength. Similar to a number of naturally occurring materials, ice is stronger in compression than it is in tension, making its

tensile strength the critical strength when ice is exposed to stresses (Masterson, 2009). The microcracks that occur during compressive loading originate through micro-tensile failures in the ice crystal lattice, which was referred to as crack nucleation (Schulson, 2001). This phenomenon is exploited in the point load test (PLT) where the compressive strength of a sample is tested by making the sample fail in tension (Wyllie & Mah, 2004).

Crack nucleation in tensile failure was explained to be followed by crack propagation through the solid ice materials (Rist *et al.*, 2002). These two processes were concluded to occur when the stresses and strains exerted on the material exceeded the intermolecular cohesion of ice (Schulson, 2001). This cohesion parameter in ice was described as the strength of freeze bonds between individual ice particles and crystals (Kulyakhtin & Høyland, 2014). Following this, Podolskiy *et al.* (2015) directly equated the tensile strength of ice to the cohesion parameter obtained for the material. Therefore, the values of tensile strength obtained by the author, and other references, were summarised into Table 2-2 below.

Table 2-2: Ice strength values from various authors

Author	**Strength Values**	**Material/Criteria used**
(Crawford *et al.*, 2021)	Yield strength = 0.5-1.0MPa	Ice sheet model parameter used
(Han *et al.*, 2015)	Compression = 3.92-5.10MPa	Sea Ice tested
(Masterson, 2009)	Flexure = 1.73MPa	Temperatures lower than -4.5°C
(Petrovic, 2003)	Tension = 0.7-3.1 MPa Compression = 5-25MPa	Testing at -10°C
(Podolskiy *et al.*, 2015)	Tensile strength = Cohesion Tension = 0.9-3.8kPa	Avalanche snow
(Reiweger *et al.*, 2015)	Tension = 0.4kPa	Weak snowpack layer
(Rist *et al.*, 2002)	Uniaxial tension = 1-2MPa Uniaxial compression = 4-30MPa Triaxial compression = 60MPa	Tests were does between -5°C and -50°C. Higher triaxial strength was seen with high confinement
(Schulson, 2001)	Tension = 1 MPa	Uniaxial tension via trans granular cleavage
(Wang, E. *et al.*, 2021)	Compression = 1.24-1.68MPa	Laboratory made snow
(Wang, Q. *et al.*, 2018)	Compression = 2.2-2.9MPa	Arctic fresh ice tested

(White & McCallum, 2018)	Tension = avg. 1.43MPa Compression = 5-25MPa	Testing at -10°C

2.3.3 Shear strength

On a larger scale of cliff analysis, shear strength is observed as the most important strength parameter to be determined. As cracks are formed between two surface areas, frictional strength between the surfaces dictates whether or not failure occurs. When the shear forces within the material exceed its shear strength, failure occurs (Jaeger *et al.*, 2009). This is further reinforced by Wyllie & Mah (2004) who state that the stability of material slopes depend on the shear strength of the material.

The parameters essential in analysis of slopes are shear strength values in discontinuities. Discontinuities in this case refer to cracks formed through tensile failure. For shear strength, the type of analysis was determined by two classes; the discontinuity shear strength and material mass shear strength (Wyllie & Mah, 2004). In most cases, instability occurs through existing discontinuities in material masses, making the discontinuity shear strength the critical and governing shear strength in most analysis scenarios (Pantelidis, 2009).

There are a number of factors that lead to the reduction of shear strength in materials. Pantelidis (2009) provided a comprehensive list of these including water pressure in cracks, expansion of freezing water, erosion of material, and velocity of water flow to mention a few. The fact that a majority of these factors involve the presence of discontinuities emphasises the governance of these cracks in shear failure, making shear strength an important component in analysis.

In 1699, Amontons' law was made stating that when two bodies are in contact with a planar surface of area *A* and pressed together by a normal force *N*, there is a critical value of a force *T*, exerted parallel to the plane of contact that will cause sliding. The formula used for this law is Equation 2-2. The two forces are related by a coefficient of friction μ, which is mainly measured using a triaxial test (Jaeger *et al.*, 2009). From the law, shear strength is now measured using the Mohr-Coulomb criterion and is expressed in terms of cohesion and an internal angle of friction. The direct shear test, shown in Figure 2-4, can be used giving normal vs shear strength graphs to obtain the cohesion and frictions angles as seen in Figure 2-5. This also provides the peak and residual strengths of the material (Wyllie & Mah, 2004).

$$T = \mu N \qquad \text{Equation 2-2}$$

$$\tau = c + \sigma' tan\phi \qquad \text{Equation 2-3}$$

where T = shear force,

N = normal force,

μ = coefficient of friction,

τ = shear stress,

c = cohesion,

σ' = effective normal stress, and

ϕ = angle of friction.

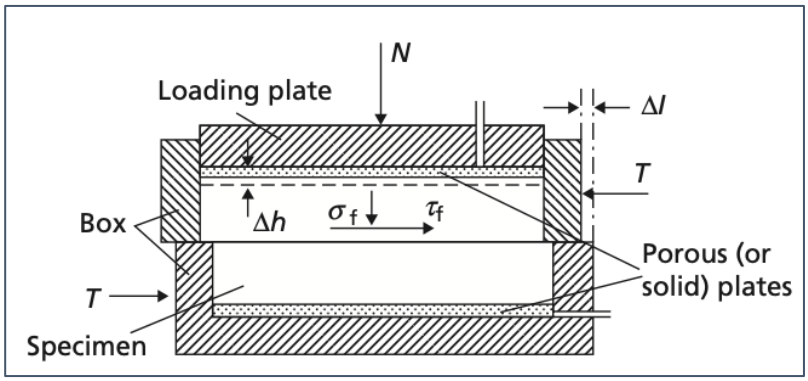

Figure 2-4: Direct shear test schematics (Craig, 2004)

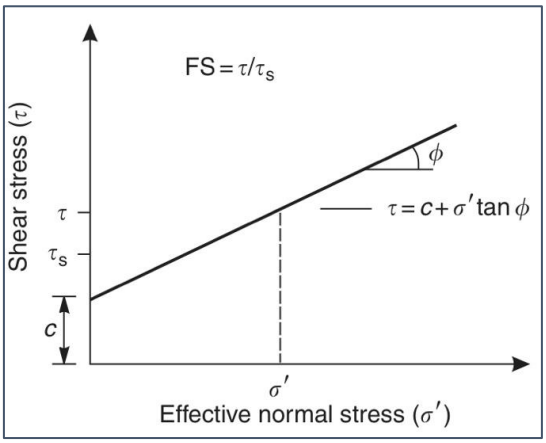

Figure 2-5: Mohr - Coulomb diagram (Wyllie & Mah, 2004)

When the parameter in Equation 2-3 were related to ice, cohesion was the strength of freeze bonds within the ice (Kulyakhtin & Høyland, 2014) and the angle of friction determined to be the residual strength in particle interlocking after the freeze bonds are broken (Serré, 2011). Shear strength was also seen to depend on a host of factors namely grainsize, strain rates, and distribution of internal faults (Bassis & Walker, 2012). More factors mentioned by Zhang, Yongjie *et al.* (2022) include crystal structure, salinity, temperature, and loading directions. The factors are experienced by both granular and columnar ice.

Despite the high importance of shear strength in ice, it remains extremely difficult to measure and this is further influenced by the absence of an official standard to be used for measurement (Lou & Wu, 2022). So far, rock measurement methods have been implemented to,

directly or indirectly, measure shear strength in ice. Such methods include unconfined single sided shear test, confined single sided shear test, and double sided shear test to mention but a few, as observed in Figure 2-6 (Zhang, Yongjie *et al.*, 2022). Lou & Wu (2022) used the double-sided direct shear testing method in their paper on plain ice. They observed a sudden brittle failure of their ice samples without warning. The failure observed was governed by crack nucleation in the samples. Cracks have been observed to appear in various orientations, which was explained to be caused by differences in confining pressures and boundaries (Schulson, 2001).

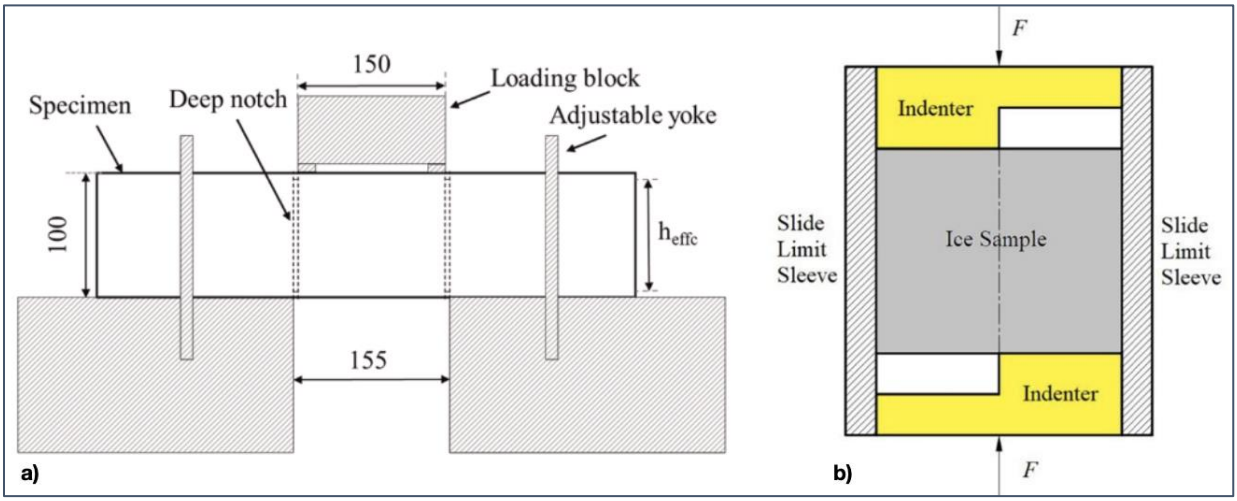

Figure 2-6: Ice direct shear schematics: **a** Single (Lou & Wu, 2022); **b** Double (Zhang, Yongjie *et al.*, 2022)

2.4 Factors affecting physical and mechanical properties

Kovacs (1997) stated that the strength of a material is a function of its solidity and therefore leads to a significant incorporation of bulk density and bulk porosity of the material. In addition to density and porosity, the statement was backed by multiple authors such as White & McCallum (2018), Wang, E. *et al.* (2021), and Wang, Q. *et al.* (2018), who listed other factors such as temperature, grain size, strain rate, crystal size, and applied stress to mention but a few. This Section therefore focuses on the temperature, strain rate and grainsize within the scope of the study.

2.4.1 Temperature factors

Ice is a thermodynamically formed material which exhibits variable behaviour types depending on the temperature around it (Sinha & Shokr, 2015). Being so temperature sensitive, all activities involving the material were temperature regulated to reduce uncertainty in results in terms of phase changes. To cater for this, various authors like Petrovic (2003), Yasui *et al.* (2017), and Schulson (2001) carried out their ice material testing in laboratories at -10ºC, all giving repeatable strength values and no effects of material degradation due to melting. The requirement

for cold temperature testing is further emphasised by Dierckx & Tison (2013) mentioning that tests at lower temperatures produce more precise test values and less uncertainty of readings. In accordance with the graph in Figure 2-3, a stable trend is viewed in temperature against depth in ice. The temperature is seen to decrease steadily with an increase in depth.

The different ice properties affected by temperature include density confirmed to increase with a decrease in temperature, moduli like Young's modulus tested to increase with a decrease of temperature, and ice compressive strength observed to increase with a decrease in temperature as plotted in Figure 2-7 (Rist *et al.*, 2002).

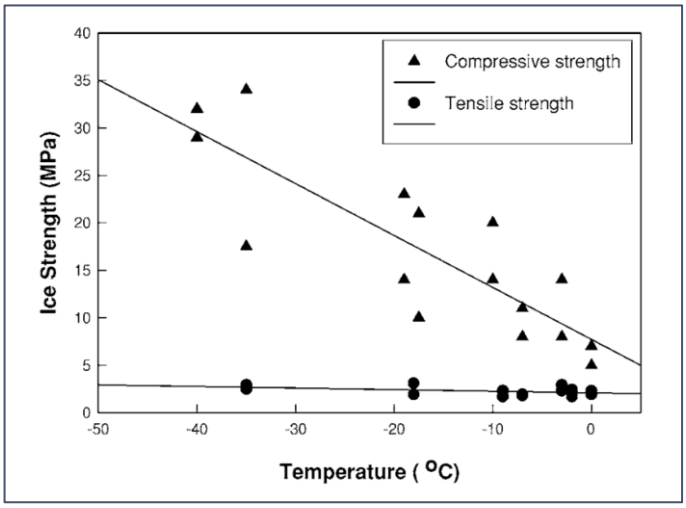

Figure 2-7: Regression plot of ice strengths against temperature (Rist *et al.*, 2002)

2.4.2 Strain rate factors

The strain rate can be defined as the rate at which the ice is loaded. Machinery used for various material testing usually have the capability to select the rate at which a material is loaded in terms of strain. The strain rate is important in material testing of ice because it directly determines the type of failure experienced by the ice.

Ice exists as a viscoelastic material, failing in both brittle and ductile patterns based on the rate at which strain is exerted on the material. There are three well documented and tested regimes of strain rates leading to varying methods of failure namely; ductile regime, transitional regime, and brittle regime (White & McCallum, 2018). This variable method of failure is mentioned to make ice a complicated material to test and understand (Wang, E. *et al.*, 2021). Various authors carried out tests on ice samples to determine the limits of the three mentioned regimes. Examples of these include Shazly *et al.* (2009) found the transition from ductile to brittle at 10^{-3} s^{-1}, Yasui *et al.* (2017) between 10^{-3} s^{-1} and 10^{-2} s^{-1}, and (Cole, 2001) between 10^{-4} s^{-1} and 10^{-3} s^{-1}. The transitional regime between the brittle and ductile ranges was determined to be the strain rate at which ice samples had their highest strength (Schulson, 2001) as observed in Figure 2-9. For low strain rates 10^{-7} to 10^{-3} s^{-1}, ice strength was seen to be independent on strain rate. However, grainsize of the ice was found to play the biggest role in the study by Schulson (2001).

This is further backed by Yasui *et al.* (2017) saying that strain rate could be scaled as a function of grainsize. They also include confining pressure as another factor affecting the possible of the transitional regime. Shazly *et al.* (2009) exclaimed that the orientation of crystals and grainsize affected ice strength in the transitional regime by a factor of 3. They called the transitional regime the quasi-static regime. Han *et al.* (2015) also added temperature to one of the factors, but Schulson (2001) stated that temperature offers a minimal influence when compared to microstructure. Coulomb criterion was used in the instances with brittle failure while Hill's criterion was used in the ductile failure region (Schulson, 2001). Despite the fact that brittle failure is greater understood with the Coulomb's method, Masterson (2009) urges the need for ductile failure analysis with regard to long term creep behaviour of ice.

Using varying strain rates, tests carried out by Böhm *et al.* (2022) elude to lower compressive strengths at strain rates higher than 4 x 10^{-3} s^{-1}. Similarly, Wang, E. *et al.* (2021) observed a critical loading rate in the range between 10mm/min and 30mm/min, below which the granular ice failed plastically into a round cake, and above which failure occurred in a brittle manner. Despite this, failure stress is independent of strain rate at high rates in the range of 10^{-2} s^{-1} to 10^{-1} s^{-1} (Cole, 2001).

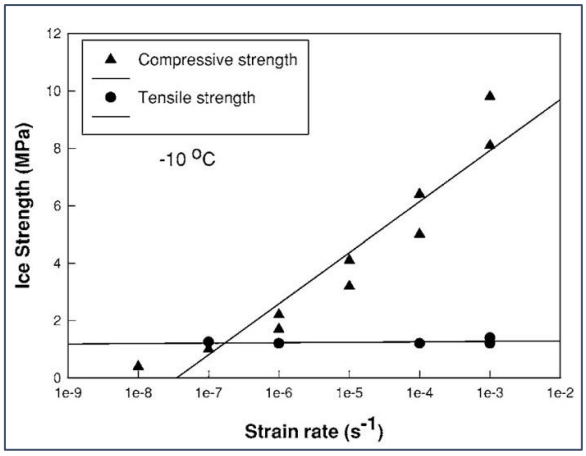

Figure 2-8: Regression plot of ice strength against strain rate (Rist *et al.*, 2002)

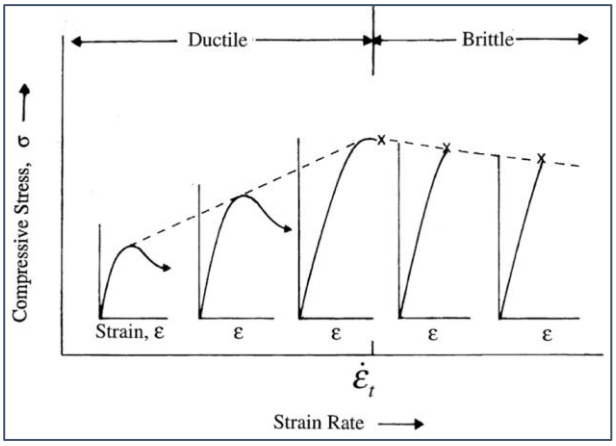

Figure 2-9: Ductile and brittle failure at varying strain rates (Schulson, 2001)

2.4.3 Grain sizes

One of the highly regarded importance of the Antarctic region lies in the ability to explore events in time trapped in the ice structure. This involves studies of gaseous atmospheric components, precipitation, volcanic activity, and more trapped inside the grain structure of the ice. This is one of the motivations for continued developments in methods of determining the accurate grain sizes on the continent (Spaulding *et al.*, 2010). Another reason for grain size collection is that the parameter was mentioned to be part of the minimum amount of data to be collected about ice (MacDonell *et al.*, 2021) and a key characterisation component together with grain orientation, morphology and densities (Cole, 2001). In relation to data collected, there was a misconception between the use of the terms crystals and grains of materials. Spaulding *et al.* (2010) offered an explanation saying that there can be about three crystals contained in a grain of a material, but in a polycrystalline material like ice, each grain contained a single crystal.

Various methods have been used to determine the grain sizes of ice in the past, with various authors adapting the use of the different methods. Andrews (1985) used polariscopes to obtain grainsizes, and further using Equation 2-4 to obtain the average grain size in the sample. Spaulding *et al.* (2010) then used scanning electron microscopy (SEM) to obtain more definitive visuals of grains to measure sizes in samples. It was mentioned that the method allows for visual definition to see grains up to 57% smaller than is possible with less complex methods. One of the less complex methods that is extensively used due to its cheaper cost and ease of use is the use of imagery through cross polarized paper. It is a well-documented method used by authors such as Rist *et al.* (2002), Sinha & Shokr (2015) and Zhang, Yujia *et al.* (2022) which uses refraction of light through crystals to differentiate individual crystals and hence obtain size measurements in mm or mm^2. For this method, samples would need to be cut to micron thicknesses to clearly view crystals. A less destructive and less detailed method used by MacDonell *et al.* (2021) involved the use of direct light from a light box to categorise grain sizes in fine, medium, or large sizes. Fine grained samples allowed the least amount of light to penetrate the samples, while large grains allowed higher amounts of light to penetrate. Grain sizes obtained by Schulson (2001) in granular ice typically ranged from 1mm to 20mm in size, while those found by Dierckx & Tison (2013) on the Nansen Ice Shelf were homogenous with a mean size of $1.65mm^2$. Ice grain diameters increase with depth (Cole, 2001).

$$D_{av} = \sqrt{A/n} = 2\sqrt{A/\pi n} \qquad \text{Equation 2-4}$$

where D_{av} = average grain size in mm,

A = sample area, and

n = number of grains in the sample.

The strength of ice and snowpacks are dependent on grain sizes along with density, temperature, and strain rate. However, the way the strengths in ice and snow vary with grainsize

differs. The strength of coarse-grained snow was observed to be higher than the strength in fine grained snow (Wang, E. *et al.*, 2021) while smaller grain sizes in ice exhibited higher strengths (White & McCallum, 2018). Grain sizes were also found to heavily affect tensile strength of ice but play a less significant role in compressive strength (Cole, 2001). In terms of deformations, fine grained ice exhibited higher inelastic deformations and more coarse-grained material fractured under minimal elongation of 0.02% - 0.04% in Schulson (2001). Grain size was also observed to affect the position of the transition zone between ductile and brittle failure modes. Increases in grain size were seen to shift the transition zone toward lower strain rates (McCallum, 2014).

Part II: Ice Shelves and Cliffs

2.5 Formation of ice shelves and cliffs

2.5.1 Ice shelf formation

The formation of ice shelves is a common occurrence in Antarctica and areas with high glacial concentrations. The glaciers can be defined as large masses of ice formed inland due to the accumulation and densification of fallen snow into ice. Glacial presence is a major contributor to the formation of ice shelves as the shelves are a direct resultant of ice movement from the glaciers as depicted in Figure 2-10a. This ice flow is the primary method of ice shelf formation as large quantities of ice flows from inland glaciers toward open water bodies through ice streams and outlet glaciers (Doake, 2001). Other methods of formation include sea ice welding of icebergs in water bodies and surface snow accumulation. The different methods of formation or combinations of them have led to development of ice shelves in a variety of sizes and can grow to areas over 500,000km^2 and 2000m in thickness (Doake, 2001).

The mechanism which causes ice shelves to float on water is a resultant of buoyancy. As flow from inland glaciers continues outwards into open water bodies, the ice and snow begin to float on top of the water due to the buoyant force exerted by the water on the less dense ice (Pollard *et al.*, 2015). The process of ice growth, in addition to the ice flow, continues through basal freezing of the water under the ice shelf and snow accumulation at the top of the flow. This growth further increases the thickness of the ice sheet until the thickness and weight of the ice equals the buoyant forces from the water, hence forming an ice shelf (Pattyn, 2018). Inland, away from the shelf-ocean interface, is a point where the ice detaches from the continental rock and begins to float. The point of detachment is known as the grounding line as shown in Figure 2-10b (Pollard *et al.*, 2015).

2.5.2 Ice cliff formation

In Antarctica, the ice shelves created are frequently seen to terminate at near vertical cliffs at points where the ice meets the ocean (Bassis *et al.*, 2021). The cliffs are observed to stand at heights as high as 25m above sea level (asl) and depths greater than 100m below the water level (Nøst, 2004). Formation of such cliffs was observed to be due to loss of ice previously buttressing the larger shelf, and continuous retreat of the grounding line through basal melting (Crawford *et al.*, 2021). The basal melting is part of a constant cycle of mass increase and decrease experienced by ice shelves where cold water currents support freezing at the bottom of the ice shelves and warm water currents cause melting. On the surface of the ice shelves, the mass increase and decrease also occurs due to snow accumulation during the colder winter months and melting during the warmer summer periods (Pollard *et al.*, 2015).

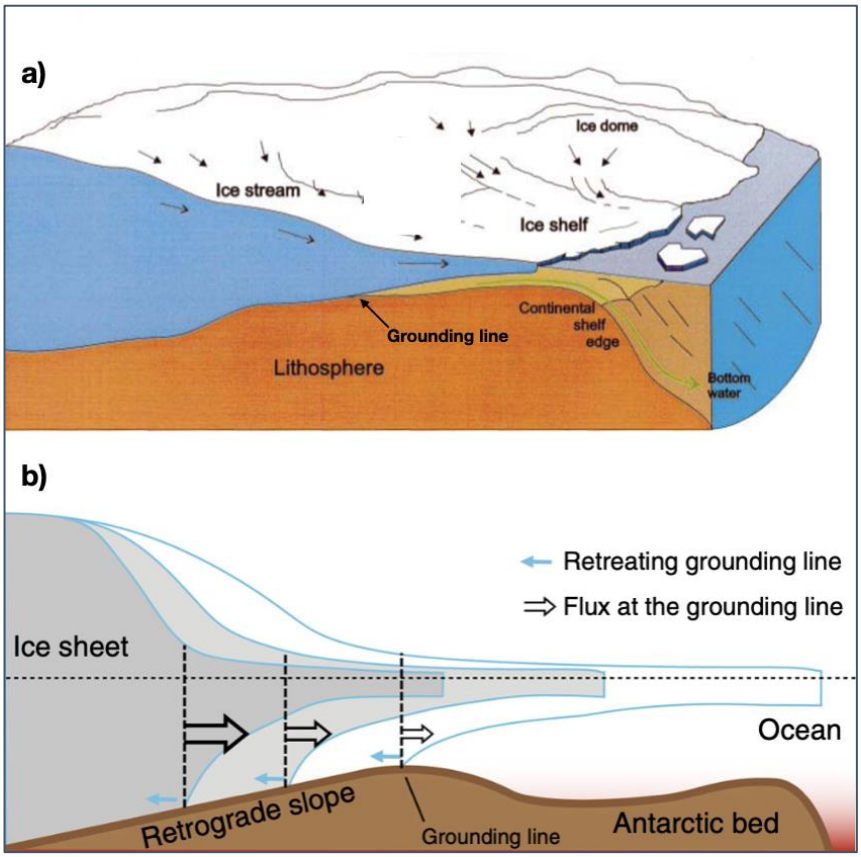

Figure 2-10: **a** Schematic 3-dimentional ice shelf formation (Doake, 2001); **b** Schematic 2-dimentional ice shelf (Pattyn, 2018)

2.6 Causes of ice shelf and cliff failures

Failures experienced in ice particularly tend to occur abruptly (Lou & Wu, 2022), which can lead to loss of life and destruction of property. This necessitated the need to study the potential causes of these ice failures and the material load bearing capacities (Masterson, 2009).

2.6.1 Global environmental warming

Antarctica is one of the regions on earth that is heavily affected by atmospheric warming and climate change (Turner *et al.*, 2014). This occurs in terms of continental ice warming of about 0.34°C per decade, reduction in sea ice development, sea level rise from ice melting, and increases in 'above melting' temperature days on the continent (Turner *et al.*, 2014). The continent and adjacent ice shelves carry importance as indicators of climate change through their sensitivity to temperature changes (Weller, 1992) experienced through ice mass addition and reduction (Doake, 2001). Doake (2001) explained how the more recent ice shelf disintegrations were attributed to atmospheric warming, which has been taking place since the 1950s. Scambos *et al.* (2009) also documented the trend showing that a high number of recent failures took place

in regions with strong climatic warming. With increasing global warming, expected retreat of glaciers and loss of ice shelves has the potential to expose high and unstable ice cliffs, which in turn increase the risk of ice cliff failure (Crawford *et al.*, 2021).

2.6.2 Crevasse formation

One of the methods global warming leads to ice shelf failure is through reduction of ice strength properties. Ice, being an active thermodynamic material (Sinha & Shokr, 2015), has strength properties with an inverse relationship to increases in temperature. One such property that decreases with temperature increase is the tensile strength of ice. Loss of tensile strength of ice leads to tensile failure which occurs through the formation of cracks (Schulson, 2001).

The cracks formed during tensile failure begin through the process of crack nucleation on a microscale of ice. Brittle materials, including ice, are seen to have pre-existing sharp cracks called Griffith flaws and explained in the Griffith theory (Lawn, 1993). These microcracks are the starting point of all crack nucleation, which occurs when tensile forces exceed intermolecular bond strengths or cohesion (Schulson, 2001).

The tensile failure experienced in ice is frequently referred to as fracture. When assessed in a fracture mechanics perspective, fracture occurs when stress intensity due to applied stresses equals the critical stress intensity factor of the material (Lawn, 1993). This material factor is referred to as the fracture toughness and fracture in the material occurs according to the expression in Equation 2-5 below. The fracture toughness of ice was stated to lie between 50 – 150KPa $m^{1/2}$ (Petrovic, 2003).

$$K = \sigma\sqrt{\pi a} = K_c \qquad \text{Equation 2-5}$$

where K = applied stress intensity,

K_c = fracture toughness,

σ = applied stress, and

a = crack length.

The stress required for crack nucleation was stated to be greater than the stress required to propagate the crack further into a material (Schulson, 2001). This eludes to the fact that propagation of the crack further through ice occurs immediately a crack is initiated. This propagation begins within the tensile stress field in the material (Rist *et al.*, 2002), up to a point where the stress concentrations at the crack tip are less than the intermolecular cohesion forces. When looking at an ice shelf, this crack propagation leads to the formation of large scale tensile cracks called crevasses, which are discontinuities within the mass and stand as the fundamental cause of majority of the failures experienced by ice.

In addition to crevasse formation due to loss of strength, some shelf failure can be driven by buoyancy and bending of the ice shelf. Considering that the shelves are floating masses of ice, differential displacement of the entire floating shelf has been observed to open up surface crevasses which ultimately have the potential to cause failure (Crawford *et al.*, 2021).

2.6.3 Hydrofracturing

The impact atmospheric warming has on ice in general is direct as it induces melting of the ice. Melt water has devastating effects on the existence and stability of the shelves and surrounding cliffs. The presence of surface melt water and crevasses has been proven to be the primary cause of hydrofracturing on ice shelves and an initialisation of the failure process. Pattyn (2018) defined hydrofracturing as the process that increases the water pressure on ice shelves from surface melt water and showed the effects in Figure 2-11. Alley *et al.* (2018) explains the hydrofracturing process more stating that it occurs when the water pressure at the tip of crack in crevasses equals the fracture toughness of the ice and compressive stresses perpendicular to the crack orientation. In addition to exceeding internal glaciostatic stresses, hydrofracturing would also cause toppling of ice masses from ice cliffs in the case when fractures exist closely spaced and in the absence of buttressing ice (Alley *et al.*, 2018).

In the past before failures occurred, excessive summer melting was experienced, leading to a high saturation of firn ice pores and melt water ponding (Scambos *et al.*, 2009). The high pressures generated by the water led to creation and deepening of crevasses which led to further instability (Pollard *et al.*, 2015). Despite this, areas with high winter snow accumulation and high firm permeability can alleviate the formation of surface ponds and crevasses formation. However, in the case that the firn gets saturated with melt water and refreezing occurs, efficient seepage of water into the firn gets hindered by the newly formed ice lenses (Alley *et al.*, 2018), and ultimately causes hydrofracturing through the area expansion of freezing water.

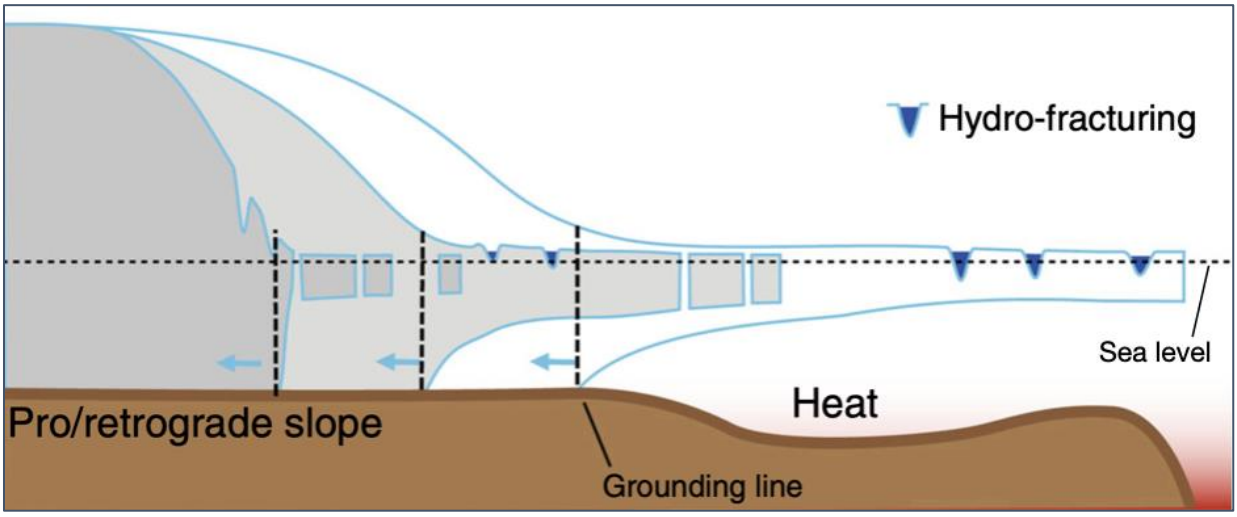

Figure 2-11: Large-scale shelf failures through Marine Ice Sheet Instability (Pattyn, 2018)

2.6.4 Sub-surface crevasses

Failure of ice shelves is not only caused by deep surface crevasses, but also the development of sub-surface crevasses. These are crevasses caused by melting of ice at the submerged base of ice shelves. Sub-surface melting can be caused by changes in oceanic temperatures or wave action from the water on the ice. Basal crevasses get deeper with penetration of sub-surface water up into the ice (Pattyn, 2018), causing further shelf weakening. A combination of the higher temperatures, leading to a reduction in ice fracture toughness, surface crevasses, and basal crevasses, could lead to failure of an entire ice shelf, especially when the basal and surface crevasses intersect (Doake, 2001) as seen in Figure 2-12.

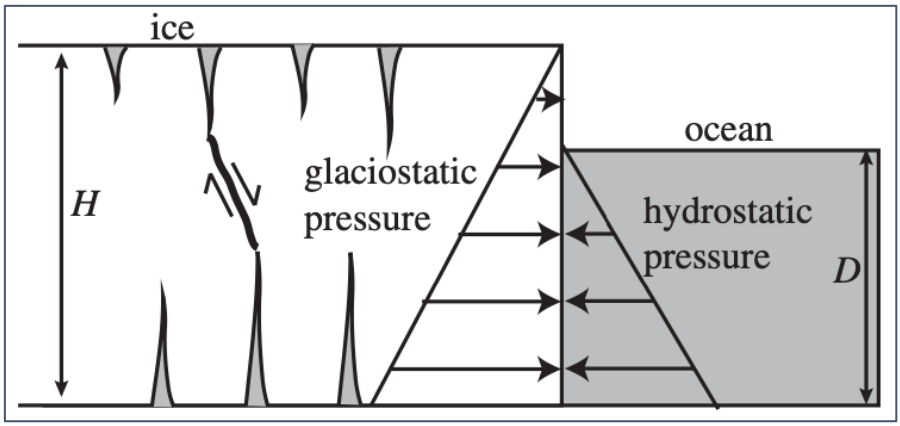

Figure 2-12: Surface and Basal crevasse intersection (Bassis & Walker, 2012)

Examples of failures that occurred in the recent past included the Larsen B failure and Wilkins Ice Shelf (WIS) failure. The Larsen B failure aggravated by sub-surface melting and lack of buttressing (Doake, 2001) and WIS by a significant warm weather period leading to high amounts of surface melting before March 2008, when the failure occurred (Scambos *et al.*, 2009). Both failed through calving, which is a form of shelf failure. Further reviews on calving and other shelf and cliff failures are detailed in the next Section.

2.7 Ice failure mechanisms

There are two main ice failure mechanisms observed in literature. First, the extreme heights of ice cliffs being formed along shelf edges developed concerns among polar researchers about the possibilities of brittle catastrophic failure of ice within the cliffs (Bassis *et al.* (2021), Crawford *et al.* (2021), Pattyn (2018)). The concern assumed an instant crushing of ice within ice shelves and cliffs due to an exceeded ice yield strength by the glaciostatic stresses in the ice mass. The increase in glaciostatic stresses was understood to be caused by an increase in the height of ice shelves and cliffs. This assumed method of failure was termed Marine Ice Cliff Instability (MICI) (Bassis *et al.*, 2021). Crawford *et al.* (2021) elaborates more on the method of failure explaining that the susceptibility of cliff faces to this type of failure may increase when glaciostatic stress

in the ice exceed about 500kPa to 1MPa, which was the approximate yield strength of ice. The cliff height to exceed the yield stress value was stated as 136m (Crawford *et al.*, 2021). There also exists the concept of Marine Ice Sheet Instability (MISI) which involves instability of ice sheets grounded on continental rock below the mean sea level (msl) (Pattyn, 2018). It is a large-scale instability of ice masses as big as continents and therefore not a pressing concern for this study. One such example of this instability is the concern for the entire West Antarctic Ice Sheet (WAIS), which is half of the Antarctic continent, whose grounding lines lie below msl, compared to the more stable East Antarctic Ice Sheet (EAIS) whose grounding lines lie above msl. A factor preventing this kind of instability is the buttressing of continental ice by ice shelves (Pattyn, 2018).

The second failure mechanism was viewed in a smaller scale of ice shelves. Scambos *et al.* (2009) described the other type of failure as shelf disintegration which is the breakup of ice from ice shelves through the formation of icebergs parallel to the shelf edge. They further delved into the disintegration describing it as being characterised by rapid successive calving of the icebergs along the shelf edge. Calving can be described as the breakaway of ice masses from parent ice structures (Doake, 2001). Icebergs formed after the calving process tend to topple outwards into the adjacent water bodies and later crumble into smaller ice rubble. With this, the following methods of failure were identified; toppling failure, and ice crumbling (Scambos *et al.*, 2009) with an example seen in Figure 2-13.

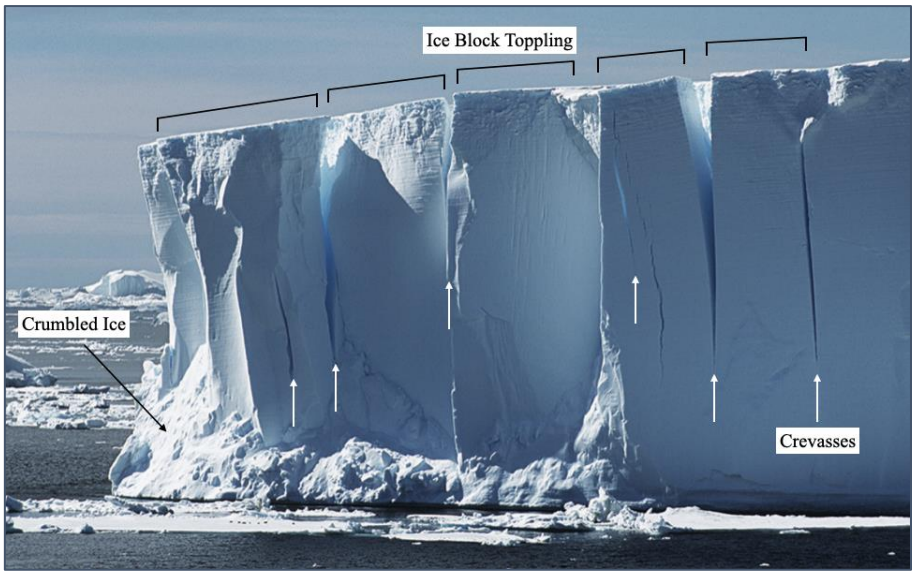

Figure 2-13: Ice block toppling & crumbling failures (Pollard & DeConto, n.d.)

In the failure types mentioned above, crevasses formation and propagation due to tensile failure is the key driving factor for failure. This in turn relates back to the crack nucleation, propagation, and the fracture mechanics that initially caused crevasse formation. In contrast to the physics behind crevasses formation, Rist *et al.* (2002) noted that the application of fracture mechanics to shelf failure would be difficult due to the low deviatoric stresses experienced in ice

shelves. They noted that the stresses remain lower than 1MPa, which is less than the fracture strength of ice between 1 - 2MPa. In addition to the low deviatoric stresses, it was also stated that air filled crevasses stabilise at depth due to back stresses caused by the glaciostatic stresses (Rist *et al.*, 2002). At back stresses greater than 200kPa, it was noted that crevasse penetration would be halted due to the inability of the stress intensities to reach the critical stress intensity at the material fracture toughness as seen in Figure 2-14 below.

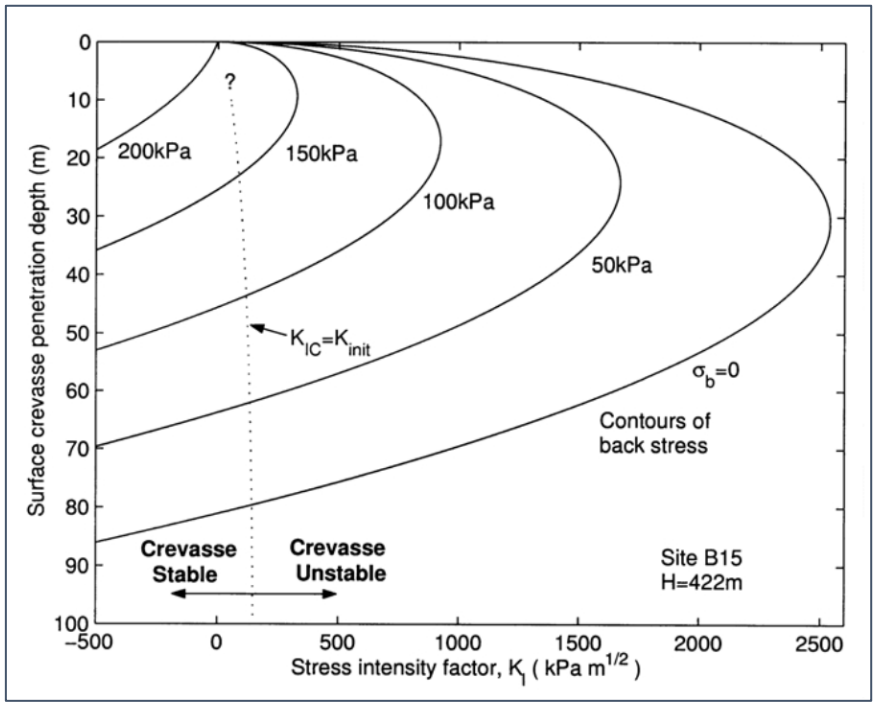

Figure 2-14: Crevasse depth against stress intensity factor relationship (Rist *et al.*, 2002)

Despite all that, calving has been observed to be the most common type of ice shelf failure with successful attempts being made to model the failure. It has been researched to be caused by tensile propagation of fractures through crevasses due to high stress fields, basal boundaries, and presence of surface water (Doake, 2001). However, a major difficulty in understanding and modelling the calving behaviour of ice has been in the vast range of calving styles experienced in polar and glacial environments (Bassis & Walker, 2012).

2.8 Ice - Rock relationship

Throughout the review of ice material properties, ice structures, and behaviour of the ice structures, a common trend was observed; ice material and structures exhibited similar characteristics to rock materials and structures. Similarities were viewed in microstructures, macrostructures, material behaviours, analysis methods, and failure modes. This Section therefore aims to provide a detailed description of the similarities between ice and rock found in literature. This was motivated by Schulson (2001) who stated that having a detailed

understanding of rock and geotechnical engineering methods plays a role in understanding ice as a material. The similarities are therefore explained in terms of formation, morphology, material behaviour, testing methods, and analysis.

2.8.1 Formation and morphology

The formation processes of ice are affected by temperature, environmental composition, and pressure to mention but a few (Zhang, Yongjie *et al.*, 2022). The pressure is a major contributor to the formation of shelf ice as it directly influences the formation of granular ice above the water level. The granular ice, also called snow ice, is formed through the deposition and consolidation of snow under overburden pressures (Cole, 2001). The granular ice formed is a porous medium, with a lattice comprised of mainly compacted snow particles and air. It is mentioned that the particles are sintered together by metamorphic processes under pressure (Kinar & Pomeroy, 2015). Sintering is the formation of bonds in snow as the snow melts and refreezes (White & McCallum, 2018). The metamorphism process changes the structure of snow grains and crystals and influences the mechanical properties of the material at large (Wang, E. *et al.*, 2021).

It is then mentioned that the metamorphic process and sintered bonds lead to the formation of an attractive force between the particles, which is referred to as cohesion among the glaciologists, with a similar effect to the cohesion used in geotechnical engineering. The two types of cohesion when referring to ice, are wet and dry cohesion which are formed due to the presence of refreezing water and pressure respectively (Ligneau *et al.*, 2022).

In terms of rock formation, metamorphic rocks are formed by the same temperature and pressure method with which shelf ice is formed. The difference however is the higher pressures and temperature experienced by the rocks in the earth's crust (Craig, 2004). As the metamorphic process for rocks occurs at such high pressures and temperatures, there are differences in properties between the ice and rock. However, ice exhibits similar properties to metamorphic rocks that have experienced high amounts of weathering, and soft rocks. The soft rocks in this context are defined as a transitional group between hard rocks and soil, with lower UCS strengths of about 0.5 - 25MPa, and have porous mediums with finer particles (Nguyen *et al.*, 2017).

From the type of rock formation mentioned, Jaeger *et al.* (2009) classified the existence of rocks in both crystal and amorphous particles joined by amounts of cementing materials. Like the rock, ice was also viewed to exist in a number of crystalline and amorphous forms (Petrovic, 2003) with Shazly *et al.* (2009) confirming 13 crystalline and 2 amorphous forms. Ice was then seen to naturally exist in a polycrystalline form which influenced the anisotropic behaviour of ice (Cole, 2001), similar to the anisotropy experienced in rock materials. Granular ice was then observed to consist of equidimensional grains with no apparent organisation (MacDonell *et al.*, 2021), which is also seen in the grains of both soft and weathered rock.

2.8.2 Material behaviour

The deformation of individual rock crystals was viewed to link to the deformation of the rock itself (Jaeger *et al.*, 2009). In addition to this, the mechanical behaviour of rock is influenced by mineral composition, matrix types, and physical properties like density and elastic modulus (Pappalardo & Mineo, 2022). When looking at soft rocks, they are discussed to they have a high deformity and softening behaviour at a macroscale, with irreversible strain (Nguyen *et al.*, 2017). In ice, the material is typically modelled as either elastic, anelastic, or viscous with effects from the microstructure (Cole, 2001). In addition to these, a number of authors like Sinha (1989), Han *et al.* (2015), and Li *et al.* (2018) have modelled ice as a viscoelastic material. Like the soft rock, authors also incorporated the deformity, hardening, and softening in their models of ice depending on volumetric activity (Serré, 2011). With the viscoelastic nature of the material, the elastic domain is mentioned to be governed by Hooke's law (Serré, 2011) with the elasticity playing a major role in shaping the viscoelastic response of the ice (Sinha, 1989).

2.8.3 Testing and analysis methods

There have been standardised procedures published for testing different materials like soil, rock, and concrete among others. However, there are no standard methods of testing the physical, deformation, and strength properties of ice. Due to this, a number of authors incorporated existing and well established geotechnical engineering methods to test their ice materials (Lou & Wu, 2022). Examples of these include McCallum (2014) who used triaxial testing methods to test ice, Lou & Wu (2022) who used double sided direct shear methods, and Serré (2011) who used laboratory direct shear tests.

Together with the geotechnical engineering tests, multiple authors also used rock material behavioural laws to analyse ice as well. An example of this was the use of the Mohr Coulomb criterion by authors like Serré (2011), Kulyakhtin & Høyland (2014), Ji *et al.* (2017), and Li *et al.* (2018). In addition to the Mohr Coulomb method used, more rock and soil analysis methods have been used on ice. Examples include Reiweger *et al.* (2015) who used a modified Mohr Coulomb model called the Mohr Coulomb Cap model, Serré (2011) who incorporated a Drucker-Prager type surface, and Kulyakhtin & Høyland (2014) who used a Modified Cam Clay (MCC) method to model the deformation of ice.

In rock mechanics, all shear type failures lead to the use of the Mohr Coulomb method expressed in terms of cohesion and angle of friction, which are parameters got using the direct shear test (Wyllie & Mah, 2004). Similar to rock, ice has been expressed in terms of cohesion and angle of friction as well, an idea which has been used and implemented since ice modelling in 1963 (Podolskiy *et al.*, 2015). The cohesion in ice is associated with the time dependent inter-crystalline bonding while internal friction is the residual strength after the sintered snow bonds are broken (Podolskiy *et al.*, 2015).

The concept of failure in rocks is observed to occur due to cracking of the cementing bridges between particles, followed by frictional resistance between the cracked surfaces (Nguyen *et al.*, 2017). The same concept is repeatable to failure in ice through the failure of sintered bonds (cohesion) followed by the friction resistance of ice residual strength (friction angle). In addition to frictional resistance, Craig (2004) highlights the importance of the residual strength especially in slope stability assessments.

In slope stability scenarios, rock masses experience strength disruptions by displacements, in form of cracks, subjected to tension and fluid pressures (Jaeger *et al.*, 2009). This issue has been highlighted in ice too as one of the most critical factors leading to failure of ice slopes and cliffs. Tension and fluid pressures cause hydrofracturing which lead to the development and deepening of crevasses (Bassis & Walker, 2012). This issue, as experienced in rock masses, is also further highlighted by authors like MacDonell *et al.* (2021) and Alley *et al.* (2018) who elaborate on the possible failure of ice masses in modes like toppling failure which are also experienced by rock masses.

Part III: Cliff Failure Analysis

2.9 Ice cliff modelling

Predictive models for ice lie at the forefront of advancements in knowledge and technology related to ice. They range from ice melting models and climate change based on historical and current data, to ice - ice and ice - ship interaction models used in the design of icebreaker ships (Cole, 2001). Models require a detailed knowledge of the physical and structural properties of ice materials. These include density, grainsize, porosity, flaw structure, compressive strengths, and shear strengths (Cole, 2001). With these properties in mind, models of ice also require application of material laws that ice follows.

Various authors model ice with similar material properties for example, Li *et al.* (2018) modelled ice with viscoelastic tensile and compression properties, Cole (2001) described models using elastic, anelastic and viscous properties, Bassis & Walker (2012) used a viscous model, Doake (2001) used a nonlinear viscous model for ice, and Crawford *et al.* (2021) modelled their ice as brittle - elastic and viscoelastic materials. In addition to these, more authors named in Section 2.8.3 used Mohr Coulomb related material laws for ice and snow modelling.

Another common factor in most models of ice shelves is the use of a near vertical cliff at the end of the shelves seen in Crawford *et al.* (2021) and Bassis *et al.* (2021), caused by previous calving events and failures. In the models, a mode of failure is first determined, then addition of model parameters is carried out to support the failure modes (Crawford *et al.*, 2021). When shear strengths of the ice are high, calving will occur through tensile failure (Crawford *et al.*, 2021). Doake (2001) explained that calving is the most common method of ice shelf failure through the propagation of tensile fractures. This further influences the need for implementation of fracture mechanics in models.

Conversely to the models run, there are difficulties in modelling ice shelves mainly due to the variety of ways ice shelves have been observed to fail in the Antarctic regions and glaciological regimes (Bassis & Walker, 2012). Another factor making modelling difficult is the presence of firn aquifers, ponded surface water, and hydrofracturing processes, which all induce fracture mechanics on ice. Implementation of these mechanisms in a realistic manner on ice shelves has proven to be an immense challenge in ice modelling due to the limited amount of knowledge available on features like the firn aquifers (MacDonell *et al.*, 2021). Another challenge to the realistic modelling of ice shelves is the inclusion of the top granular structure of ice to large scale models. This was noted by Crawford *et al.* (2021) who opted to ignore the top granular parts of their Helsinki Discrete Element Model ($HiDEM_{be}$) of the ice shelf, observed in Figure 2-15. Crawford *et al.* (2021) stated that it would be impractical to incorporate the layer due to the scale and complexity of the model. Omission of the top layer therefore aided the modelling process by allowing the ice to be treated as a homogenous material, producing reliable results for the ice shelf scale used.

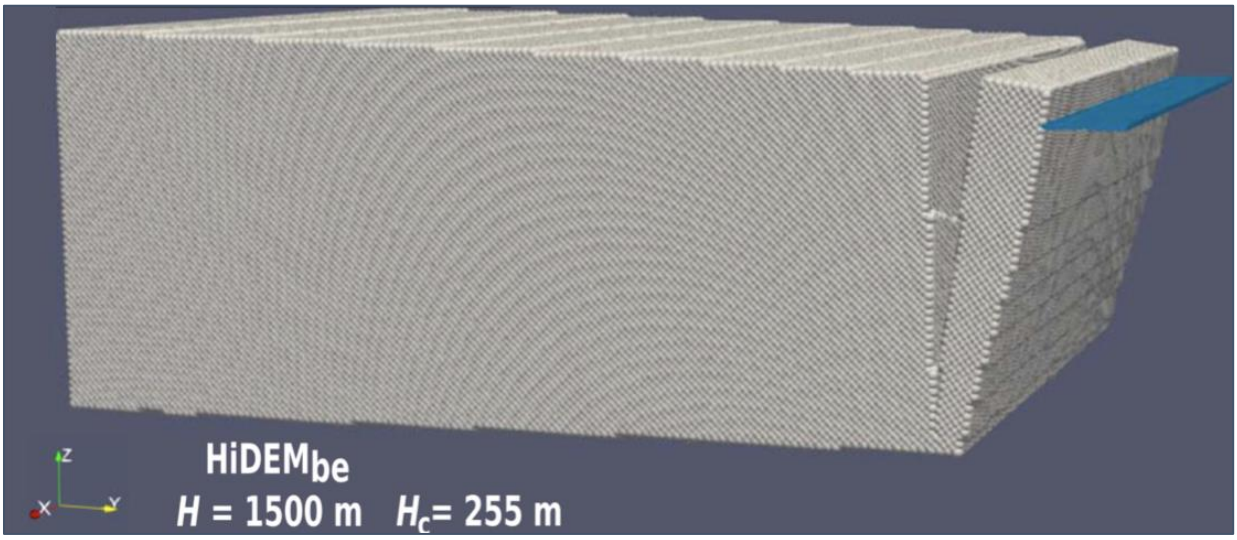

Figure 2-15: Helsinki Discrete Element ice shelf failure model (Crawford *et al.*, 2021)

Despite the successful models run by authors in this Section, the difficulty experienced when modelling the complex behaviours of ice cannot be understated. This has led to simplification of models used, which in turn has effects on the accuracy of results obtained. To therefore attempt to understand ice in terms of more largely documented methods, the next Section introduces methods used to carry out slope stability analyses in rocks.

2.10 Rock slope modelling

Analysis of slopes is a fundamental part of civil engineering as a number of structures are constructed on angled or vertical rises of earth masses. These include excavations, embarkments, foundations, mines, and many more. These earth structures angled to the horizontal can be referred to as slopes and can be either natural or man-made. Earth masses, both soil and rock, elevated at an angle to the horizontal ground tend to degrade to a flatter or an ultimate angle of stability through landslides and creep (Howland & Gardiner, 1986). The action of the degradation is referred to as slope stability failure as a slope's movement from its initial geometry to a final state involves shear failure of the material keeping the slope mass intact.

Such an occurrence has the potential to move millions of tonnes of soil, rock, or water downstream of the slope and could lead to property damage and loss of life. One such example is the Vajont Dam failure in 1963, Italy which was attributed to the failure of adjacent valley slopes caused by the filling and drawdown of the reservoir (Paronuzzi *et al.*, 2013). Due to the rock slope failure of the valley walls, the reservoir water was forced over the dam walls, flooding the immediate town of Longarone. This resulted in the complete destruction of all infrastructure and over 1200 fatalities in the town and 2500 further downstream.

With the consequences of failure being catastrophic, Hoek & Bray (1981) provide designers with methods that can be used to recognise potential slope stability issues in the early design stages to design slopes to function effectively and safely. This can help prevent damage to property and ultimately, loss of life. Therefore, this Section describes literature available that provides an understanding of both soil and rock stability and how that can be used to understand the mechanisms in ice cliffs in Antarctica and the Fimbul ice shelf.

2.10.1 Methods of rock slope stability analysis

According to the 2010 Geotechnical Engineering Code of Practice, a site investigation is required to precede any on-site construction or engineering analysis. The need of such an investigation provides information like site geometry, constraints, surrounding structures, among other site-specific details. This allows for an understanding of forces driving or resisting instability on the site.

In the case of rock cliffs, kinematic analysis and limiting equilibrium (LE) methods are the conventional methods used for slope stability analysis (Eberhardt, 2003). Limiting equilibrium can be described as the condition where the forces on a slope driving failure are exactly equal to the resisting forces on the slope (Wyllie & Mah, 2004) hence the use of the term 'limiting'. The method rationalises resisting forces against the failure driving forces to form Factor of Safety (FS) equations, with the base equation shown in Equation 2-6. Limiting equilibrium methods are the most commonly used methods due to their simplicity and minimal computer power requirements. Kinematic methods, on the other hand, use slope geometry and detailed positioning of discontinuities to carry out a feasibility and probabilistic modelling of the slope. They use the detailed information to predict possible modes of failure. The method is data intensive and requires more investment in field work surveys than the LE method.

$$FS = \frac{Resisting\ forces}{Driving\ forces} \qquad \text{Equation 2-6}$$

In the case of large intact rocks, weak rocks, soil like materials and heavily jointed rocks, Eberhardt (2003) advises the use of numerical and continuum modelling as well to address the limitations of limiting equilibrium. More complex geometries, non-linear material properties, and more variable slope scenarios can be modelled using numerical methods. However, this method requires intensive computational power and numerical modelling knowledge to run and understand the program output.

With LE methods being the most common, various equations have been made to analyse different methods of failure based on the driving and resisting forces. Following the base FS equation shown in Equation 2-6,the factor of safety in soil and rock is primarily calculated using the more detailed formula in Equation 2-7 with the main factors offering resistance to failure

being cohesion and the material's internal angle of friction. The driving forces in the equation are shear forces caused by factors like weight under gravity, overburdened pressures, and water pressures.

$$FS = \frac{cA + \Sigma N tan\phi}{\Sigma T} \qquad \text{Equation 2-7}$$

where c = cohesion,

A = area,

N = normal force,

T = shear force; and

ϕ = angle of internal friction.

2.10.2 Rock slope failure mechanisms

Rock slope analysis carries with it multiple similarities with the analysis of soil slopes. Firstly, both stability considerations are affected by the properties of the encased materials and secondly, similar base analysis methods and criteria are used. Despite the similarities, rock stability analysis is distinct in that the most important failure determination factor is the orientation of rock behind the rock face (Wyllie & Mah, 2004). This orientation is based on the slope angle, orientation of discontinuities in the rock, dip angle, dip direction and strike. The dip angle can be defined as the maximum inclination angle of a discontinuity to the horizontal and the dip direction is the direction an angle of the dip line measured clockwise from the North (Wyllie & Mah, 2004). Together with the dip angle and dip direction, strike is alternatively used to analyse discontinuities as it is the line of intersection between the horizontal and an inclined plane (Wyllie & Mah, 2004).

Each of the mentioned factors are in turn used to draw stereonets, that aid in the determination of rock failure mechanisms illustrated in Figure 2-16. The dip, dip direction, strike and discontinuity data are fed into graphical analysis software to graph the data and show intersections between discontinuities or steep dip angles. This in turn aids in the determination of possible slope stability failure modes. There are four main types of rock failure observed from stereonet drawings. They include plane failure, wedge failure, toppling failure, and circular failure. With reference to the failure types observed in ice cliffs, plane failure and toppling failure are the most relevant in the list.

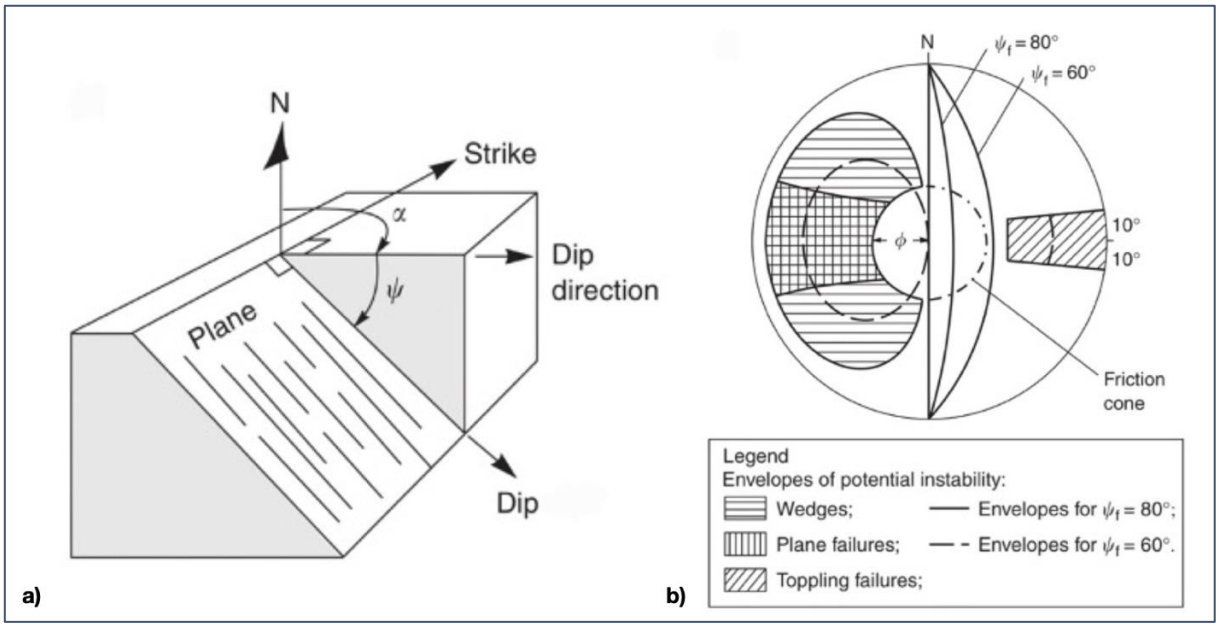

Figure 2-16: **a** Dip, dip direction and strike of a geological formation; **b** Instability envelops for rock slope failures (Wyllie & Mah, 2004)

2.10.2.1 Plane failure

Plane failure occurs when a block slips along a single plane away from the rock mass and towards the slope face and valley. In order for this to occur, Wyllie & Mah (2004) mention the following factors:

- The strike should occur approximately parallel to the slope face with a leeway of ±20°.
- The dip plane must be less than the angle of the slope.
- The angle of the dip must be greater than the angle of friction.

In addition to the factors mentioned, presence of a tension crack increases the chances of plane failure by acting as an infiltration point for water which adds water pressure as a driving force and can lead to erosion of cementitious material along the sliding plane. Surface drainage and ground water conditions are key internal factors influencing plane failure (Raghuvanshi, 2019). The tension crack could be caused when shear stresses in the rock exceed the shear capacity of the rock and sliding would occur when the shear forces exceed the sliding resistances along the sliding plane (Raghuvanshi, 2019). Together with the internal factors mentioned, external factors influencing plane failure include rainfall, seismic activity, and human activities like excavations (Alemdag *et al.*, 2014).

An example of a plane failure occurred in Gumushane, Turkey on 09th August 2008 which was caused by excavations at the bottom of a hill. The case study was carried out by Alemdag *et al.* (2014), viewing three discontinuity planes which acted as slip surfaces in the highly fractured granite rock as seen in Figure 2-17 (Plane failure schematics from Wyllie & Mah (2004)). The authors carried out a kinematic analysis which confirmed a plane failure possibility and further

LE and numerical modelling to obtain factors of safety for the slope. They found the FS of the slope before excavation as 1.33, which was stable, and the FS after excavation at the bottom of the hill as 0.98 which confirmed the slope instability. They used Rocscience's Dips for the kinematic analysis, RocPlane for the LE method and RS2 for numerical modelling.

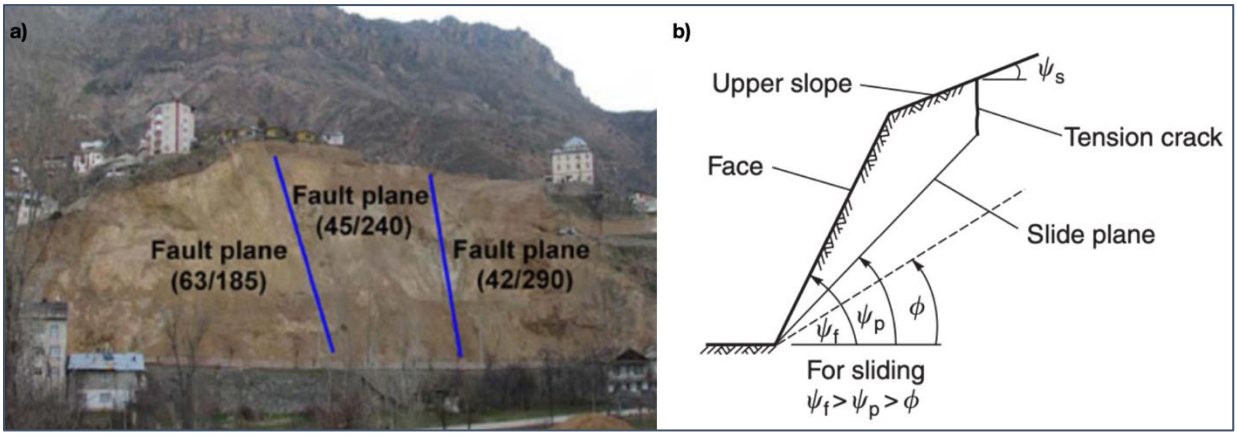

Figure 2-17: **a** Plane failure slide planes (Alemdag *et al.*, 2014); **b** Plane failure schematics

Limiting equilibrium is the most commonly used method in analysis of plane failures and widely used in engineering practice. In line with the base factor of safety formula in Equation 2-6, the FS for plane failure slope configurations can be obtained using the following equation first established by Hoek & Bray (1981):

$$FS = \frac{cA + (W cos\psi_P - U - V sin\psi_P) tan\phi}{W sin\psi_P + V cos\psi_P} \qquad \text{Equation 2-8}$$

where A = area,

c = cohesion,

ϕ = angle of internal friction.

U = water force acting on the sliding plane,

V = water force acting in the tension crack,

W = weight of the sliding block, and

ψ_P = dip.

2.10.2.2 Toppling failure

Unlike plane, toppling failure occurs due to rotation of a rock column about a fixed base. Such rotation is caused when the centre of gravity of a rock column lies outside the fixed base of the rock. It occurs in four different types namely: block toppling, flexural toppling, block-flexural toppling, and secondary toppling (Adhikary *et al.*, 1997). However, block and flexural toppling

are the most common types analysed in depth by Hoek & Bray (1981). Block toppling occurs when smaller rock columns are pushed outwards by larger rock columns whose centres of gravity lay outside their base area. Flexural failure on the other hand occurs due to flexural failure of the rock slanted over the edge of a steep slope (Wyllie & Mah, 2004).

In flexural topping, being the most common mechanism of the two, the slanted rock columns are visualised as cantilever beams fixed at a certain depth. When the rock columns bend forward under their own gravitational weight, they exert tensile and compressive bending forces onto the adjacent columns, subsequently causing failure when tensile strengths are exceeded (Adhikary *et al.*, 1997). Failure in this mechanism was seen to occur plastically with either fractures or non-fractures depending on the type of material used. Strong rocks failed with the fractures, while weak rocks or highly weathered rocks failed without the fractures (Adhikary *et al.*, 1997).

Toppling failure can also be identified in highly jointed rock using kinematic analysis with a stereonet result shown in Figure 2-16b. A limiting equilibrium analysis of toppling failure can also be carried out through an iterative analysis of each block under the method conditions, starting with the highest block to the lowest (Wyllie & Mah, 2004). A result of the experiments carried out by Adhikary *et al.* (1997) on toppling failure can be seen in Figure 2-18 with the LE schematics by Wyllie & Mah (2004).

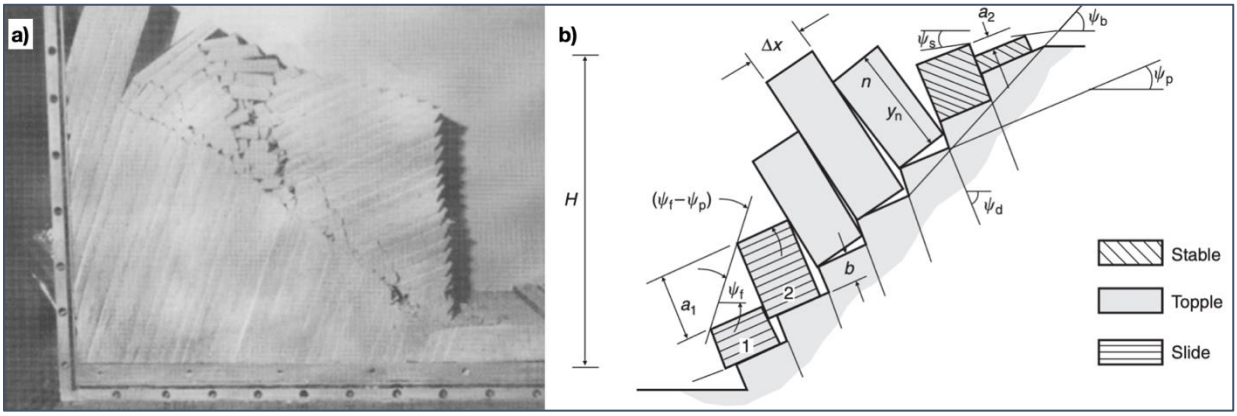

Figure 2-18: **a** Toppling failure experiment (Adhikary *et al.*, 1997); **b** Toppling failure schematics

2.10.3 Rock modelling software

Modelling of natural materials, despite the challenge, has enabled advancements in multiple sectors like engineering, climatography, medical fields, and sustainability to mention but a few. In geotechnical engineering, there are a number of methods used to carry out modelling for rocks and slopes. These can be separated into 3 methods namely: deterministic methods, empirical methods, and numerical methods.

The conventional methods of rock slope modelling are limiting equilibrium (LE) and kinematic analysis (Eberhardt, 2003). The use of the two methods is termed a deterministic

approach. Similar to deterministic models are the empirical models that are based on rock classification systems like rock mass rating (RMR), slope mass rating (SMR), slope stability probability classification (SSPC), and others (Raghuvanshi, 2019). The numerical methods of slope analysis then involve continuum modelling, discontinuum modelling, and hybrid modelling (Stead & Wolter, 2015).

The three methods of analysis have been implemented into different geotechnical engineering software. Modelling in the geotechnical engineering sphere is commonly carried out using the following software packages: FLAC, GeoStudio's Slope/W, PLAXIS, and Rocscience's RS2. Each of the software were analysed individually to obtain their capabilities and limitations. These are summarised in Table 2-3 below. Different software packages and modelling methods have their advantages and limitations, with Eberhardt (2003) emphasising the need to understand the methods' strengths and weaknesses to maximise usage of the software.

Table 2-3: Geotechnical modelling software comparisons

	FLAC	**PLAXIS**	**Rocscience RS2**	**GeoStudio Slope/W**
Capabilities	Multiple Geotech applications	Comprehensive Geotech modelling	2D numerical modelling of slopes	Integrated package for slope modelling
	Diverse material models	Advanced material models	Advanced soil & rock models	Variety of slope stability models
	Strain controlled	Stress controlled	Stress controlled	Stress controlled
	FDM	FEM	FEM	FEM
	SRF analysis	SRF analysis	SRF analysis	LE analysis
	Built-in Python		Intuitive UI	Intuitive UI
Limitations	Crude mesh setup	Medium to high learning curve	Specified to slope analysis	Specified to slope analysis
	High learning curve	May require other software to run analysis	Limited to 2D	May require other software to run analysis
	Resource intensive	Resource intensive		Limited to 2D
	Command driven			

Effective modelling of natural materials therefore requires an assortment of input parameters to define the material and environmental conditions to be simulated. Examples of these are material boundaries with respect to the real world geometries, material laws followed, micro scale material behaviour, macro scale material properties, and material strengths. The classifications used to obtain a selection of these properties are detailed next.

2.10.4 Rock classification methods

Throughout geotechnical engineering history, rocks have had extensive studies carried out on them from periods as early as 1946 when Terzaghi's rock load classification system was published. Like in soils, rock investigations involve intrusive methods of coring into the material to withdraw representative samples of the area.

To obtain information about the samples and material as a whole, rock classification systems were developed by various researchers to determine estimates of the material properties quickly and easily. The most common of these classifications include the rock quality designation (RQD), Q – system, geological strength index (GSI), slope mass rating (SMR), rock mass index (RMI), and rock mass rating (RMR) to mention a few, listed by Kundu *et al.* (2020) and Salaamah *et al.* (2018). RQD is defined as a ratio of the sum of sound sections of core greater than 10cm to the total length of the core (Zhang, 2016). It is calculated using Equation 2-9. RMR is a cumulative function of 6 parameters, each classifying the rock mass properties, to give a broader rating of the rock mass as a whole (Singh & Goel, 1999). The Q – system, like the RMR, involves the use of ratings given to different rock properties but primarily focused on the rock joint properties. These include number of joints, joint roughness, joint alteration, and joint water reduction. The joint properties are combined using Equation 2-10 (Singh & Goel, 1999).

$$RQD = \frac{\Sigma\,(core\ lengths > 10cm)}{Total\ core\ length} \qquad \text{Equation 2-9}$$

$$Q = \left[\frac{RQD}{J_n}\right]\left[\frac{J_r}{J_a}\right]\left[\frac{J_w}{SRF}\right] \qquad \text{Equation 2-10}$$

where RQD = rock quality designation,

J_n = joint set number,

J_r = joint roughness number,

J_a = joint alteration number,

J_w = joint water reduction number and

SRF = shear reduction factor (Singh & Goel, 1999).

The RQD, introduced by Deere & Deere (1988) gained popularity in the geotechnical field primarily due to its ease of use. It gives an indication of the degree of jointing and fracturing

in a core mass based on the cores extracted (Lucian & Wangwe, 2013). In recent studies like Zhang (2016), RQD is also being correlated to a number of critical rock properties like uniaxial compressive strength and elastic modulus. With advancements in technology, new methods of obtaining RQD have also been developed for example the use of seismic velocities to determine the RQD percentage of jointed rock masses. Despite the ease of use, RQD has been ruled as a conservative method to only be used for preliminary estimation of material properties (Zhang, 2016). This is primarily due to the lack of detailed information obtained from the method. To tackle this limitation, the other rock classification methods like the RMR provide far more detailed analysis of rock masses and can be correlated in a less conservative way to the RQD. The method used to calculate RQD is detailed in Figure 2-19 below.

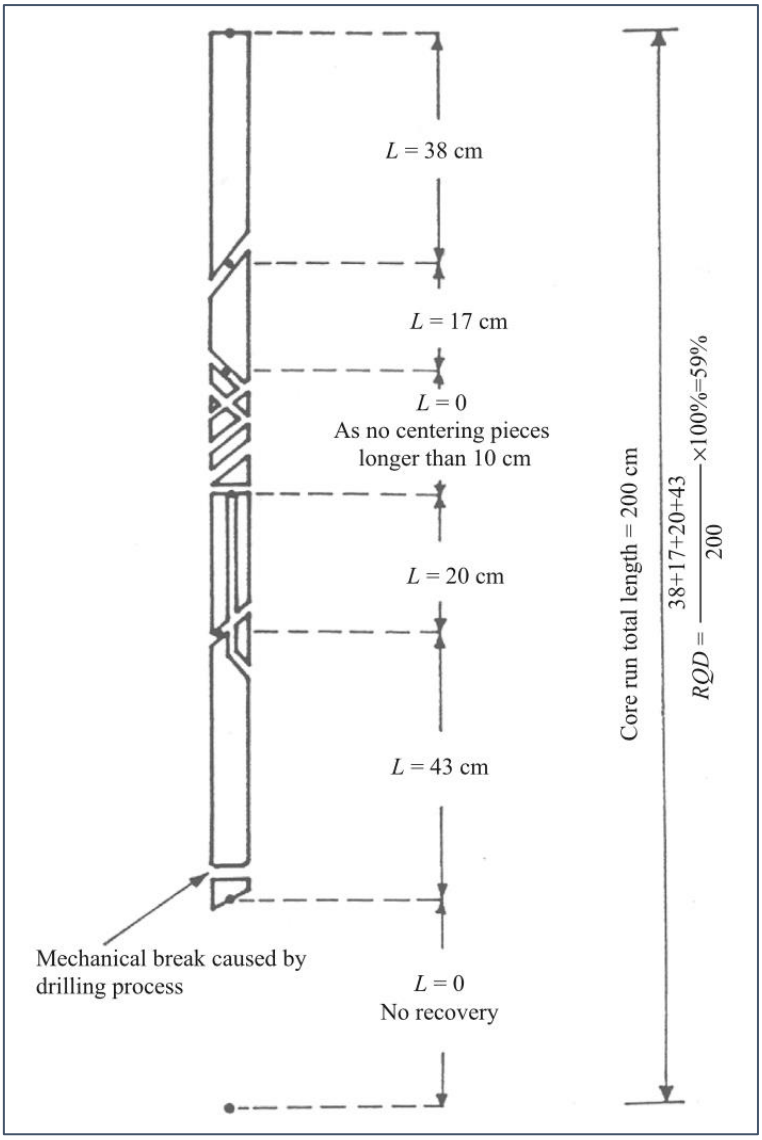

Figure 2-19: RQD determination (Zhang, 2016)

The RMR is also a widely used method due to its approachability, responsiveness, economic and adaptive nature (Kundu *et al.*, 2020). It was developed in 1973 by Bieniawski at the South African Council of Scientific and Industrial Research (CSIR) (Singh & Goel, 1999) and has had revisions and additions since then (Aksoy, 2008). RMR functions as a cumulative rating system from a number of rock parameters obtained from samples. It used 6 parameters namely: UCS, RQD, discontinuity spacing, discontinuity condition, ground water, and discontinuity orientation with the first 5 called the basic RMR. Each of these carry a rating, with a cumulative rating from all adding up to the RMR rating at the end (Aksoy, 2008). With the RMR rating, various rock parameters can be estimated. These include: cohesion, internal angle of friction, elastic modulus, and shear strength, with the values of cohesion and friction angle acceptable for use in slope analysis (Aksoy, 2008). Despite its advantages, RMR is a subjective method to be effectively performed by an experienced professional in rock engineering. Singh & Goel (1999) suggest the use of ranges to quantify RMR instead of single values. However, to counter the subjectivity, Kundu *et al.* (2020) made quantified equations relating the RMR to each of the rock parameters mentioned. Singh & Goel (1999) also emphasise that RMR is to be used for saturated and weathered rock slopes in conjunction with in-situ tests and numerical modelling for more detailed design and engineering outputs. The study of these characteristics therefore improves the modelling capabilities needed to test and apply natural materials in structural, climate, industrial, and other developments (Cole, 2001).

2.11 Summary of chapter

Ice in Antarctica exist as hexagonal crystalline Ih ice, which is also referred to as ordinary ice. Snow that falls in the area forms granular ice, which in turn undergoes metamorphism into columnar (solid) ice under increased overburden pressure and decreasing temperature.

To measure the density of ice, the most common and efficient method reviewed was the mass/volume method, giving density results for solid ice around 900 - 920kg/m^3. Density was observed to increase with increase in depth in the ice shelves. Elastic modulus and Poisson's ratio were both obtained using dynamic and static methods, giving results of 9.7 - 11.2GPa and 0.29 - 0.32 for E and v respectively. UCS were also observed to range between 4 - 30MPa, while tensile strengths of about 1 - 2MPa were directly equal to the cohesion forces in the ice.

Following an understanding of the ice material properties, ice shelves were reviewed to be primarily formed through ice flow from inland glaciers. The shelves were also observed to terminate in near vertical cliffs where the flowing ice met the ocean, forming ice cliffs. The causes of failure of these structures included global atmospheric warming, formation of both surface and basal crevasses, and hydrofracturing. These led to calving failures which occurred in form of planar, toppling, or crumbling failure types. Authors had successful analyses for failures of the ice structures through Finite Difference Method (FDM) and HiDEM models but noted considerable simplifications and challenges when modelling the structures.

Through the review to this point, two gaps were identified in the literature. Firstly, as sufficient data on solid ice properties existed, little to no data was obtained on the properties of shelf granular ice, and particularly granular ice on the Fimbul ice shelf. Secondly, homogenous solid ice was used in multiple ice shelf models, ignoring the effect that a granular ice layer would play on the stability of the ice shelves. This motivated the need to test the physical properties of the Fimbul granular ice and run cliff stability models incorporating the properties of the measured granular layer and observed solid ice properties.

To obtain the properties and carry out the modelling, the relationships between ice and rock materials in literature were reviewed due to the well documented methods used for rock analysis as opposed to the absence of standardised ice analysis methods.

3 Methodology

This methodology chapter describes the procedures and equipment used to achieve the objectives of this study. It was divided into four parts following the chronological order of events. Part I commenced this chapter by detailing the study area, its location and the boundaries used throughout the fieldwork. Part II then described the material used in the study and listed the equipment used for both fieldwork and laboratory experiments. Part III followed this, describing the procedures undertaken to obtain repeatable results in the study. It contained the fieldwork, morphology test, physical property test, and strength test procedures. Part IV then concluded the chapter by detailing how the field and laboratory work outputs were incorporated into a cliff stability model of the ice shelf. This contained the process used to build the model and analysis methods used by the model.

Part I: Study Area

3.1 Location and features

On the Antarctic continent, the Fimbul ice shelf is located on the 2.5°W longitude. The ice shelf is comprised of an ice sheet floating on the Atlantic ocean, with a grounding line about 200km inland from where the shelf meets the open water body (Nøst, 2004). The shelf is also characterised to terminate in a vertical cliff towering to about 28m asl (Luka & Keith, 2021). Throughout this report, the distance from the cliff face to 5m inland was referred to as the cliff edge. Inland from the vertical cliff, the area was observed to have a relatively flat topography which was fully covered in both ice and snow.

The area undergoes seasonal transitions throughout the year. It experiences summer between the months of November and February and winter between May and August. The average temperatures recorded in the summer months ranged between -10 and -20°C while winter months averages between -30 and -40°C with limited sunlight (Turner *et al.*, 2021). In addition to the cold temperatures, and as Antarctica is considered the driest continent on earth, the area receives little amounts of rainfall throughout the year. Majority of the rainfall experienced by the area was observed to occur in the summer months, specifically December and January, producing an average precipitation range of 1 - 10mm per year (Vignon *et al.*, 2021). Despite the low rainfall, the area experiences high wind speeds averaging 40 - 50km/hr and recorded gusts of up to 200km/hr. An image of the shelf edge can be observed in Figure 3-1 below.

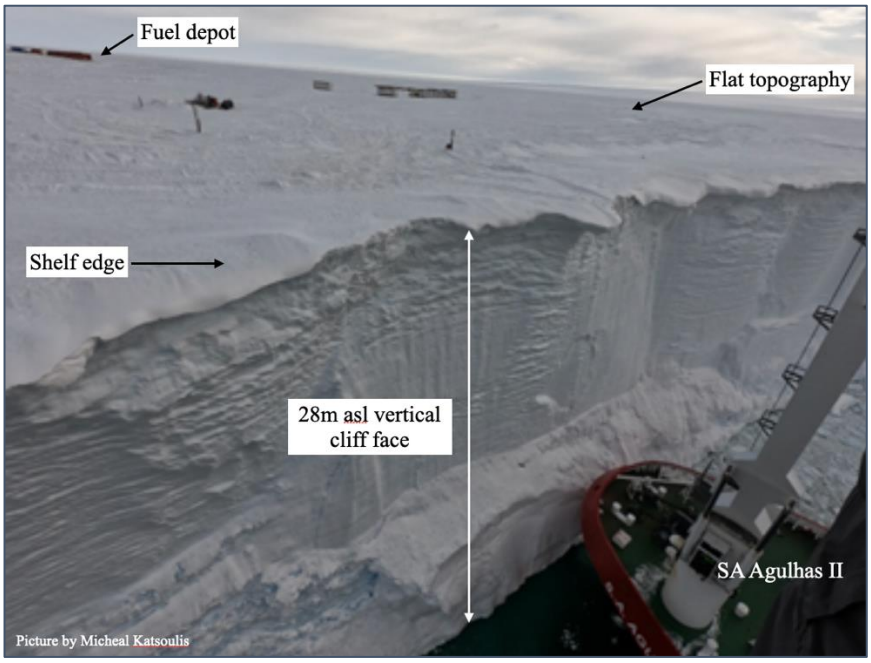

Figure 3-1: Fimbul shelf cliff face

On the ice shelf, the specific area of study was located at 70º15’26.85”S 2º42’0.38”W, covering an approximate 100 x 200m area from the shelf edge. This area was specifically used for its practicality, offering a direct route from the ice shelf to the SANAE IV research base located at 71°40’25”S 2°49’43”W inland. It was also in close proximity to a fuel depot established on the ice shelf that can be seen in both Figure 3-1 and Figure 3-2.

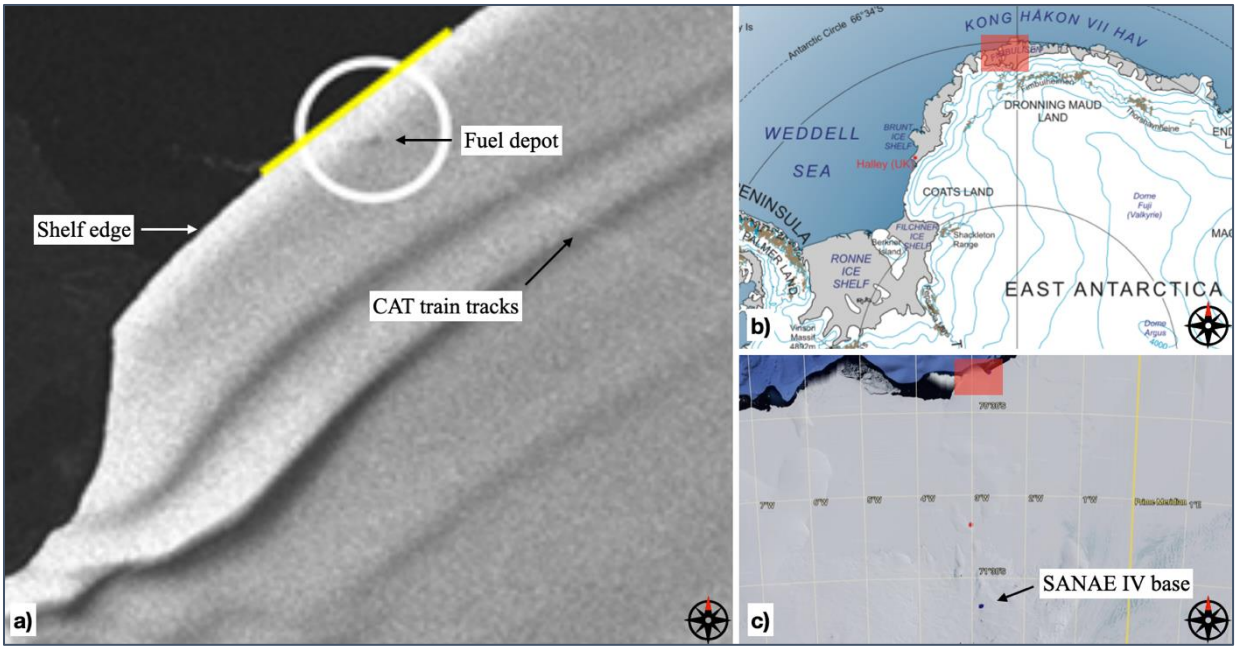

Figure 3-2: **a** Satellite imagery of Fimbul Ice Shelf; **b** Geodetic map showing Fimbul; **c** Map showing the shelf edge relative to SANAE IV

Part II: Materials and apparatus

3.2 Material

The material used in all experiments was ice. The ice used was directly obtained from the Fimbul ice shelf, Antarctica, at the study area described in Section 3.1 above. The ice was naturally formed ice, referred to as Ih or ordinary ice. The ice was comprised of H_2O molecules bonded together with hydrogen bonds (Libbrecht, 2001) which formed a polycrystalline material, with crystals existing in hexagonal shapes. The same type of ice was found throughout the study area as the pressures within the ice mass did not exceed 150MPa and temperatures of -80°C required to change the type of ice.

The ice was formed through the accumulation and metamorphism of snow. When snow fell in the area, it underwent metamorphism through overburden pressure from newer snowfall and sintering to form the top layers of ice on the shelf (Kinar & Pomeroy, 2015). The properties of this ice were investigated further in this Chapter.

3.3 Fieldwork equipment

The equipment used during field work at the study area was categorised into safety equipment, ice extraction equipment and ice storage equipment. Safety equipment was used to maintain personal vitality during the field work carried out on the shelf. The equipment therefore included cold weather gear and fall rescue equipment. To keep warm during field work, inner liners, over coats, over pants, snow boots, gloves, balaclavas, ski-googles were used. For fall rescue, personnel wore harnesses which were always tethered together using a safety line. In addition to the safety line, each member carried an ice axe, extra rope, an ice anchor, and a pulley to be able to initiate a rescue in case a colleague slipped off the edge or fell into a crevasse.

To retrieve the ice, coring was carried out. The coring was carried out using a Mark II Kovacs ice corer with attachable extensions as shown in Figure 3-3. It was comprised of a hollow lightweight filament and an aluminium head with heat treated steel blades. The blades of the corer were designed to bite into solid ice, trapping an ice core inside the filament while ejecting ice debris from the plastic flighting wound on the filament. The corer was used with a T-bar handle for manual drilling and a battery powered Makita hand drill for easier and faster mechanical drilling. A handheld Global Positioning System (GPS) device was then used to mark core coordinates.

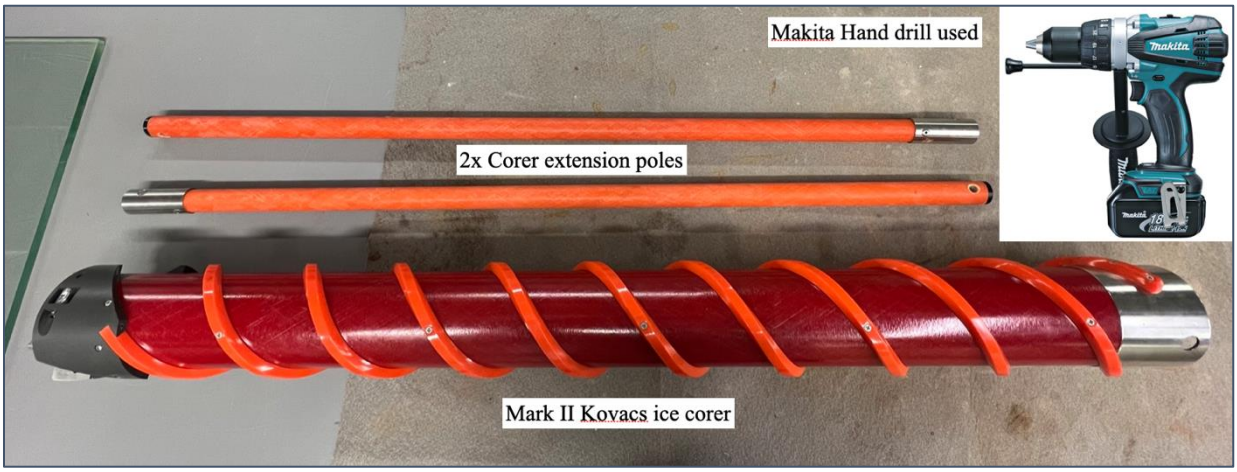

Figure 3-3: Kovacs ice corer used

To mark and store the cores, soft flexible poly vinyl chloride (PVC) piping was used. The PVC piping was chosen due to its malleability, low thermal conductivity, and exact dimensions required to fit cores from the corer. Wooden boxes of dimensions 1500 x 300 x 500 mm were then used to fit the cores housed in marked PVC piping. Wooden boxes of this size were made due to their light weight, ease of construction, and low thermal conductivity. To further regulate the temperatures in the boxes, they were lined on the inside with Styrofoam to insulate and maintain the cold core temperatures within the box.

3.4 Laboratory apparatus

Different types of apparatus were used in the laboratory during this study. These were categorised into sample preparation which detailed equipment used to prepare samples for tests, physical property measuring which detailed equipment used to measure density, elastic modulus and Poisson's ratio, and strength property measuring which described the compression machine used to carry out UCS tests.

3.4.1 Sample preparation equipment

Before any tests were carried out, all samples obtained were logged. This was done in log sheets designed to capture sample information like stratigraphy, sample image, sections to be tested and descriptions of sections. To capture clear sample images, a lightbox in Figure 3-4 was designed and used. The lightbox was wooden 1200 x 200 x 200 mm hollow box, housing an LED strip light on the inside, and topped with a translucent perspex sheet. The LED light below the perspex sheet was used to illuminate the entire sheet, creating an even distribution of light on top of the box.

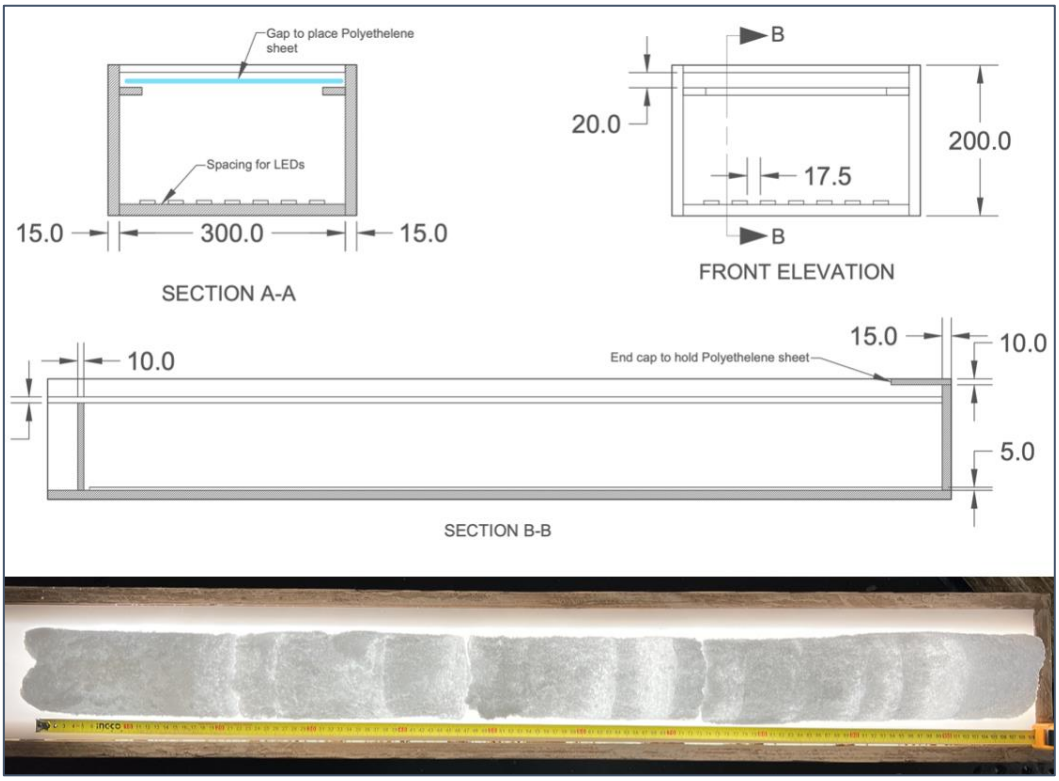

Figure 3-4: Lightbox design and function

To then cut samples for tests, and bandsaw was used. This was a motor operated wheel saw with a sliding table. This was used to cut samples to required heights obtained using a tape measure. As the bandsaw was used to cut samples to heights to a minimum of 10mm, a microtome was used to cut samples to micron thicknesses. The microtome used was a Bright retractive sledge microtome, observed in Figure 3-5, with a stainless steel blade. This was used to prepare samples for thin section analysis discussed later in this report.

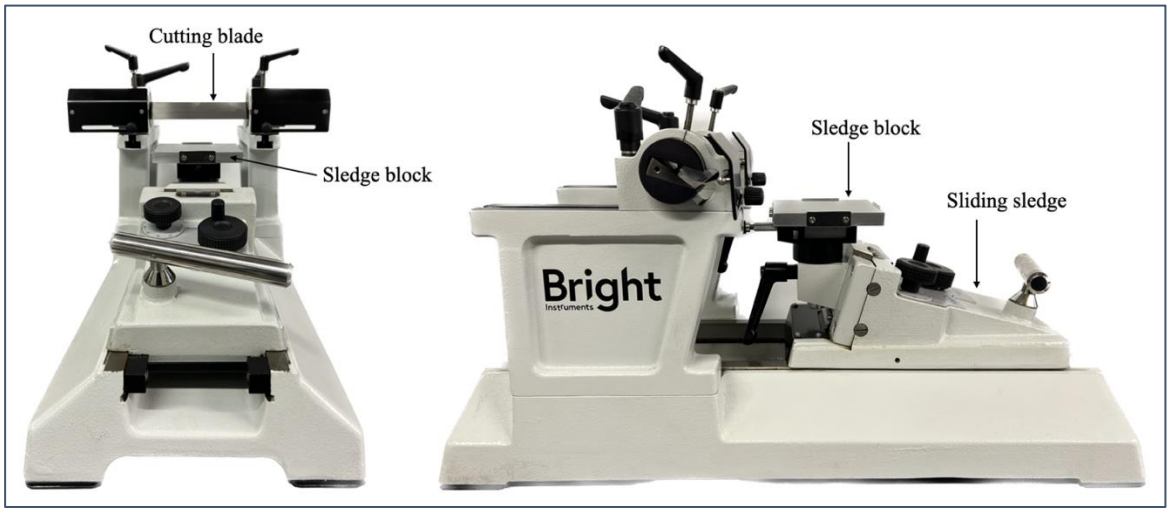

Figure 3-5: Retracting sledge microtome used

3.4.2 Physical property measurement equipment

The physical properties to be measured were density, elastic modulus, and Poisson's ratio. To measure density, an electronic scale and vernier calliper were used as shown in Figure 3-7. These instruments both output reading to two or more decimal places, increasing the accuracy of results and minimising uncertainty. The electronic scale was used to obtain mass readings to 3 decimal places and the vernier callipers was used to obtain height and diameter readings to 2 decimal places.

Elastic modulus and Poisson's ratio were then measured using an ultrasound machine. The ultrasound measurement device available for the tests was the Proceq Pundit PL-200 with 250kHz shear wave transducers shown in Figure 3-6. Like the machine used in this regard, other authors reported using similar ultrasonic measurement setups like the Proceq Pundit used by Brotons *et al.* (2016) with both Primary and Shear wave transducers, a GCTS ULT-100 Ultrasonic velocity test system used by Yasui *et al.* (2017), and Proceq Pundit used by Pappalardo & Mineo (2022) with two 250kHz S-wave transducers. The machine functioned by emitting Pressure (P) waves and measuring reflected Shear (S) waves. It then measured the velocity of sound through the material, together with an input density, to calculate the *E* and *v* properties.

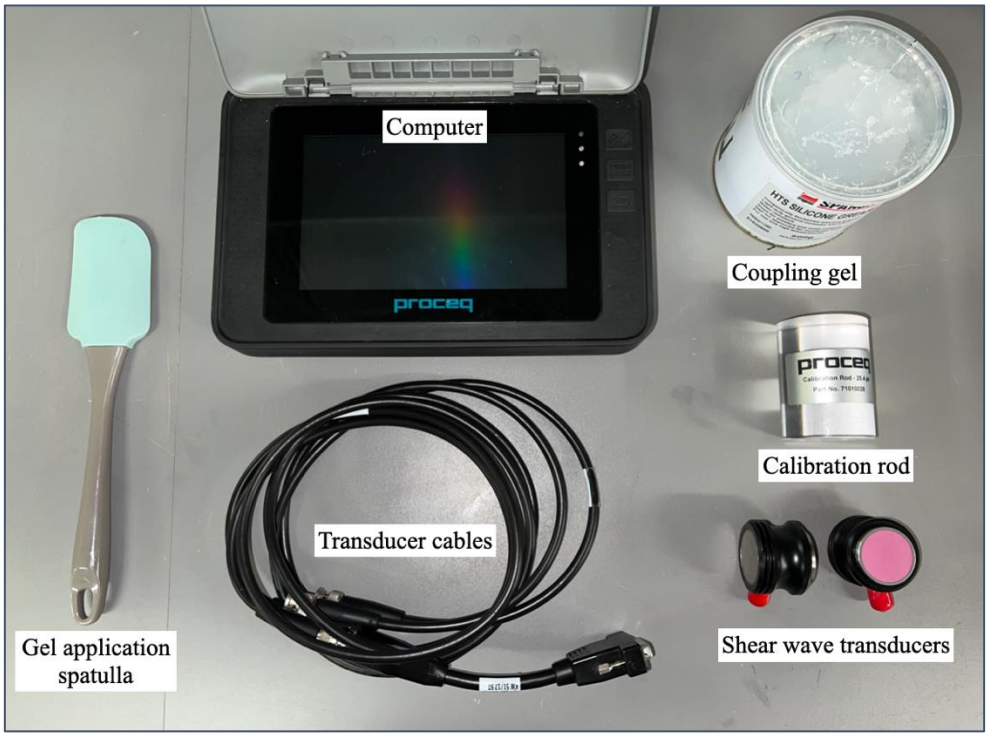

Figure 3-6: Ultrasound testing equipment

Figure 3-7: Density testing equipment

3.4.3 Strength property measurement equipment

The strength property measured was the uniaxial compressive strength which was obtained using unconfined uniaxial compression of samples. The equipment used for this was a PLT-2W compression machine from GCTS testing systems observed in Figure 3-8. The machine is a lightweight, portable, battery powered compression machine with load capacity of 100kN. The machine as shipped from the factory was fitted with point load test (PLT) platens, initially intended to apply an extremely localised loading for rock strength index measurements. The machine also originally had a horizontal opening of 100mm, vertical opening of 125mm and a displacement stroke of 50mm.

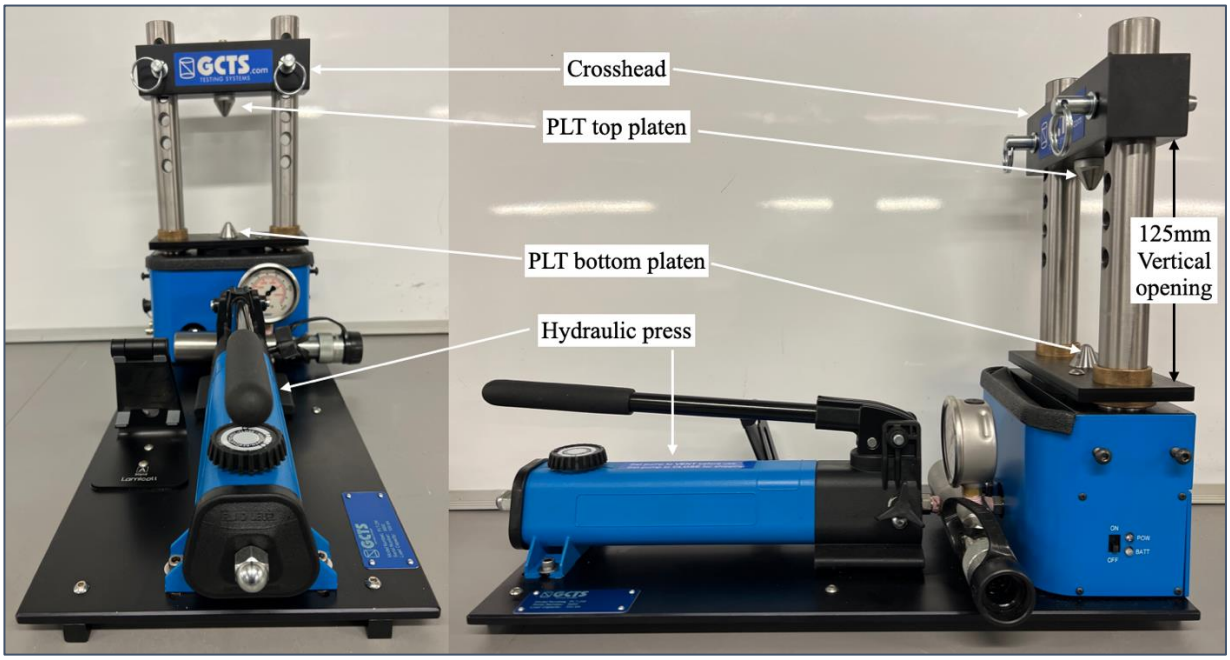

Figure 3-8: GCTS PLT 2W Compression machine used

To carry out UCS tests up to an acceptable standard, the height of samples tested were to be twice the value of the diameter of the same sample i.e., Height = 2*D*. Cores retrieved from Antarctica were cored using a 90mm drill corer, which retrieved cores of about 90mm in diameter. This therefore dictated a number of requirements for the UCS test setup. The requirements were:

- Height clearance of testing equipment > 180mm.
- Horizontal diameter clearance of approximately 95mm.
- Flat, parallel UCS compression platens to uniformly distribute the compressive load.

Due to the size limitations of the PLT-2W, modifications to the machine were considered and designed to be able to meet the testing requirements. The decision to modify the equipment was an efficient and economical choice which allowed for versatility in the modification design. Designs for the modifications were made using SolidWorks software.

3.4.4 Compression machine modifications

3.4.4.1 Platen design

To carry out the UCS test, the load from the machine was required to be transferred to the tests samples from a flat even surface on both the top and bottom in a uniaxial manner. In order to achieve this, a platen design was created to firstly, fit between the poles of the compression machine, secondly, seamlessly replace the existing PLT platen, and thirdly, be sturdy enough to carry loads significantly higher than the failure loads of the ice test samples.

The detailed designs drawings conceptualised and used for the UCS platens can be seen in the Appendix. The platens were made 95mm in diameter to fully encapsulate the 90mm diameter ice samples and comfortably fit into the compression machine with a horizontal clearance of 100mm. The platens were designed as stainless-steel elements to withstand the loading onto the ice samples and to protect the platens from moisture corrosion. The threaded holes on the UCS platens matched the screws originally used with the PLT platens enabling secure mounting without further modification. The design output can be observed in Figure 3-9.

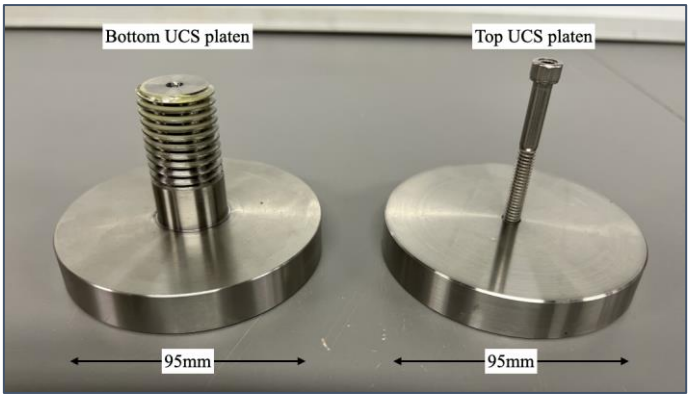

Figure 3-9: Uniaxial Compression platen design output

3.4.4.2 Increased vertical clearance

The major drawback from using the PLT-2W was the height limitation of 125mm vertical clearance. This would not suffice for samples with a 180mm vertical height. To accommodate this, a design of pole extensions was conducted. The poles to be designed were aimed to increase the maximum usable height of the machine to a value that would cater for a wide range of sample heights. Together with this aim, the extensions were to use that same crosshead as the original poles of the machine. In a structural aspect, the pole extensions would also need to be structurally sound to withstand the tensile forces exerted on the material used for the extensions during sample loading. The critical location, where failure of the pole extension would be expected was the meeting point between the top smaller section and larger bottom section. To minimise the stress concentration, a generous radius was specified at the change in diameter to allow a smooth transition of stress between the two sections.

The detailed SolidWorks design of the pole extensions can be found in the Appendix. The design was made with wider base to fit onto the current poles and be fastened by steel pins. The top section of the extension was however designed with a diameter equal to that of the original pole to allow use of the same crosshead with a firm fit. Two extensions were made following this design to fit on both machine poles. Both pole extensions were designed as stainless-steel parts due to the strength of steel and corrosion protection offered as observed in Figure 3-10. With this design, the maximum testing height would be significantly increased from 125mm to over 300mm.

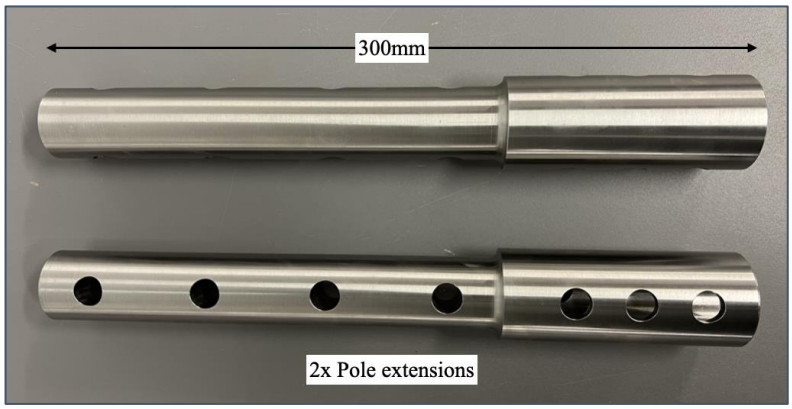

Figure 3-10: Pole extension design output

3.4.4.3 Final compression apparatus design

The output of the modification designs from the manufacturing workshop, together with steel pins used to hold the poles and crosshead in place during testing were shown in the machine assembly in Figure 3-11. The PLT platens were fully replaced with the UCS patterns, both at the bottom and at the crosshead. The pole extensions were also inserted onto the exiting poles and fastened by the additional pins. The modification of the machine did not impact the performance of the machine with regard to load and displacement sensors.

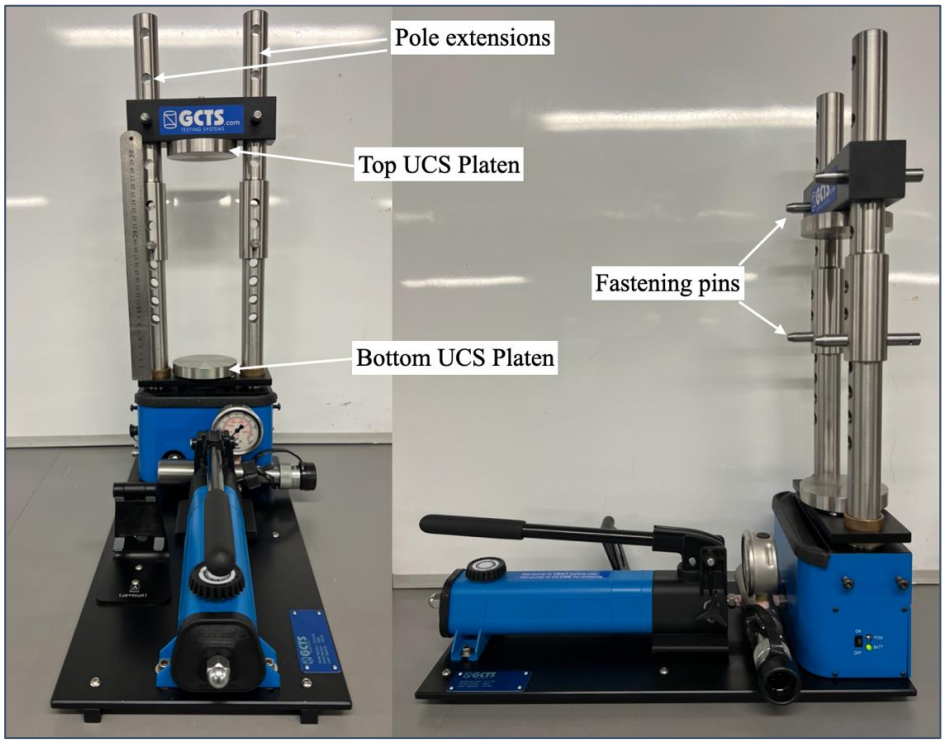

Figure 3-11: Modified PLT 2W compression machine

Part III: Test procedures

3.5 Fieldwork procedures

3.5.1 Ice coring procedures

3.5.1.1 Core retrieval

Core retrieval took place through a process of ice coring in the study area. Before any work was conducted on the ice shelf, permission needed to be granted by the ship's Captain. The decision to work was based on the weather conditions on the ice. When permission was given, all the cold weather gear was put on in preparation for transport onto the shelf. The corer was assembled on the ship, with only necessary equipment carried along to minimise weight. The PVC piping was put into the wooden core boxes and closed for transport onto the shelf. Both people and equipment were lifted off the ship and placed on the shelf by the large crane on the ship which was docked with ship bow against the cliff face.

A GPR subsurface investigation first took place on the shelf. This was used to identify discontinuities such as subsurface cracks and crevasses invisible to the eye due to snow cover. Ice coring then took place following the transects of the GPR where no discontinuities were found. This was done to assure safety of personnel carrying out the activity as the discontinuities were deemed as health hazards.

Core locations were chosen and distributed throughout the length and width of the study area to offer a thorough representation of the material. At each location, a site preparation preceded the coring. This involved the scrapping away of loose snow at the chosen location. The loose snow was characterised as the layer of fresh snow loose enough to be swept away by hand. This loose snow was swept by hand until firm ice was encountered, after which the remainder of the snow was removed using a shovel. This action was done similar to the removal of organic soil on top of engineering drill sites.

With the site prepared, the corer was held vertically upright and stable using the handles on the Mikita drill. Using the weight of the operator and rotation of drill when turned on, the drilling process commenced with the corer driven fully into the ice. The corer was driven 1m into the ground, allowing for retrieval of 1m cores at each of the locations. Obtaining deep cores at the site's distance to the shelf edge introduced concerns of increased cliff instability which would risk the lives of people working close to the shelf edge. This was aggravated by the brittle failure nature of ice, meaning in case failure were to occur, personnel would have little to no time to evacuate. On drill completion, the metal clamps at the bottom of the corer were automatically wedged out to hold the ice within the filament. The corer was then lifted out of the ice using the drill handles as captured in Figure 3-12a. The drill and metal cap on the corer were removed to create the gap through which the ice core was ejected.

During core removal, the GPS coordinate of the core hole was taken using a GPS device, and the coordinate written on the PVC pipe using a permanent marker. The bottom and top of the core were also marked on the pipe, symbolising the orientation of core retrieved. The bottom of the pipe was then closed using zip ties and front left open to receive the core. The core was then removed from the filament, oriented correctly, and put into the PVC pipe. The top was then sealed using another zip tie and put into the wooden insulated box for transport back into the ship freezer which was set at -10°C. A total of 39 cores were obtained and plotted into Figure 3-13.

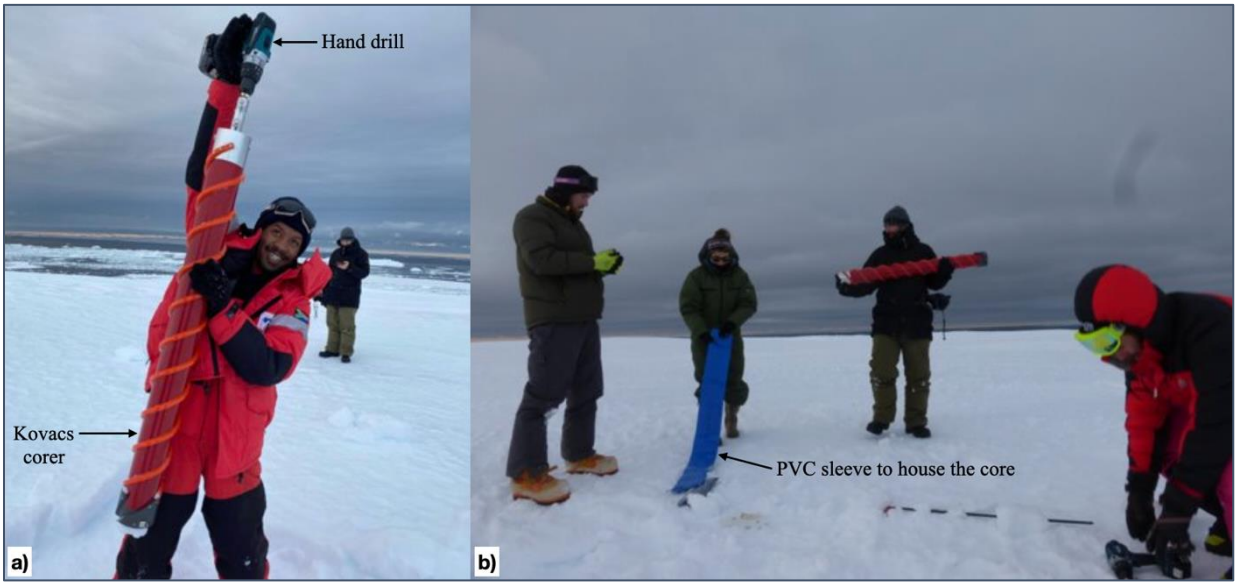

Figure 3-12: **a** Core retrieved from ice; **b** Core to be stored in flexible poly vinyl chloride piping

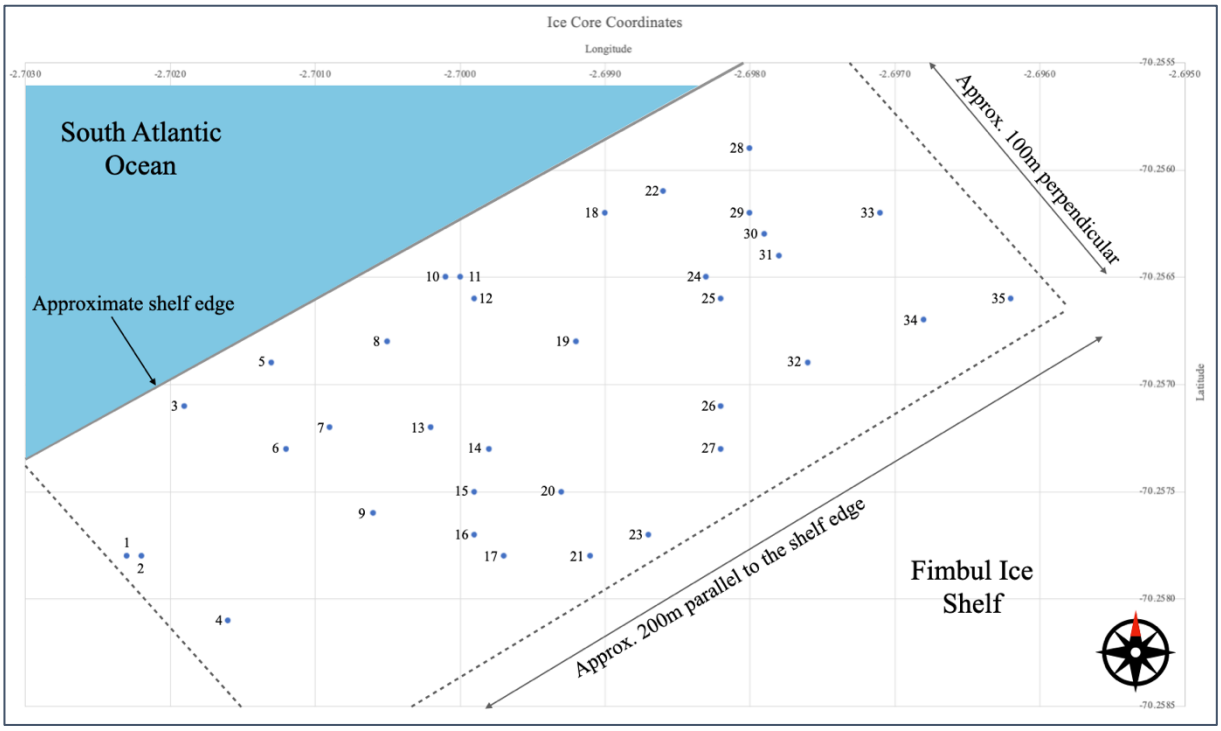

Figure 3-13: Map of the study area showing geographical locations where ice cores were retrieved

Cores on the SA Agulhas II were stored in the on-board freezer until the ship returned to the Cape Town port. At the port, the cores in the freezer were all packed into the insulated wooden boxes in preparation for disembarkation. There were 5 boxes, with about 8 cores per box. Each box was then carried by two people from the freezer and placed onto the crane loading platform where they were immediately tied using ratchet slings and lifted by the crane off the ship and loaded directly into a freezer truck with a freezer that had been precooled to -20ºC. This temperature was chosen to maintain the cold temperature inside core boxes and as safety factor in case the cores were exposed to any warmth during the vehicle transportation. To minimise core box movements in the truck, the core boxes are securely tied together using ratchet tie downs and placed horizontally side to side in the truck. The Styrofoam inside the boxes also supported the cores and protected them from heavy contacts.

The cores were then transported from the port to UCT and stored in the polar engineering lab at -10ºC. The core boxes were individually carried by two people from the truck to the cold lab. Each of the truck and cold lab doors were kept closed unless the cores were being moved. This was done to prevent excessive changes in temperature when the freezers were exposed to warm air. The -10ºC in the UCT polar lab, though colder than the temperature at which the cores were retrieved, was set following multiple literature sources who carried out ice testing in laboratories set at -10ºC.

3.5.1.2 Core information capture

On arrival to the UCT polar lab, preparation of the cores for testing was initiated. The first stage of this was an information capture where core information like coordinates, length, features, and damages was logged.

The process used to remove the cores from their casing involved a core lifted out of its insulated wooden box and placed on the flat lightbox top. The zip ties on the top end were cut using scissors, and the core tilted from the bottom end. One person lifted the bottom end of the core, while the other held the open top end through which the core was removed. The cores slid out of the PVC under their own weight and were guided onto the light box for observation.

A picture was then taken for each core laid on the light box. The pictures were taken with the aim to be used in core log sheets which are attached in the Appendix. In addition to the pictures, coordinates of each core were written and transferred in to an excel sheet. In the excel document, the core coordinates were filled in degrees, minutes, and seconds, as written on the PVC casings in the field, and converted to the decimal format. In the decimal format, the coordinates were sorted in an ascending order of Longitude and given core numbers for easier identification. This led to an increase in core number from West to East of the study area as seen in Figure 3-13.

The coordinates were also used to graphically represent the cores on a linear scale of Latitude versus Longitude. This showed anomalies in coordinates that appeared significant distances away from the approximate study area. Coordinates of this nature were removed from the data set with the assumption of human error or device malfunction when writing down the core coordinate in the field. The cores at such coordinates were set aside to be used for sample experiments, as no location would be associated to the obtained results.

3.5.1.3 Initial property estimates

The two primary methods used to obtain initial properties of the ice material were the rock quality designation (RQD) and rock mass rating (RMR) explained in Section 2.10.4. Among the most used methods of rock characterisation, these two methods were chosen due to their applicability to the types of data obtained during core retrieval. The inability to obtain site measurements on specific cracks on the shelf disqualified the use of rock qualification systems like the Q-system and GSI for the ice.

Each core was first characterised using the RQD which is the quality of the core obtained. In rock characterisation, natural faults and cracks in the rock cores are looked at as the discontinuities affecting the run of cores, with drilling breaks identified amongst the cracks and ignored in the calculations. In the case of the ice cores, two features were looked at as the discontinuity factors on cores obtained. Firstly, changes in grain sizes. This was influenced by the changes in physical properties exhibited between the different sizes. More on this can be found in Section 3.6.3 later in this Chapter. Secondly, changes in ice type from granular to solid

ice. This was primarily impacted by the existence of ice lenses along the lengths of cores, which were layers of near-pure ice amongst the granular ice on the shelf. Like the cracks in rocks, the two were taken as the discontinuities due to the change in material properties from one material or grainsize to another, and their influence as planes of weakness in the material as a whole.

To embark on the RQD determination, images of each of the core, like that in Figure 3-14, were taken and an exact scale placed next to the image in line with the tape measure used in the laboratory. This was done to ensure uniformity in image capture process. Together with the images taken, the various grain size stratigraphy and positions of ice lenses were viewed and logged into the log sheets for easier identification and analysis. Using positions from the two factors, RQD was determined by identifying consistent core lengths greater than 10cm. This means that only lengths unaffected by both the ice lenses and grainsize changes were considered. In each core, the total length of undisturbed >10cm core lengths was calculated and divided by the total length of the core to obtain the RQD percentage of the core.

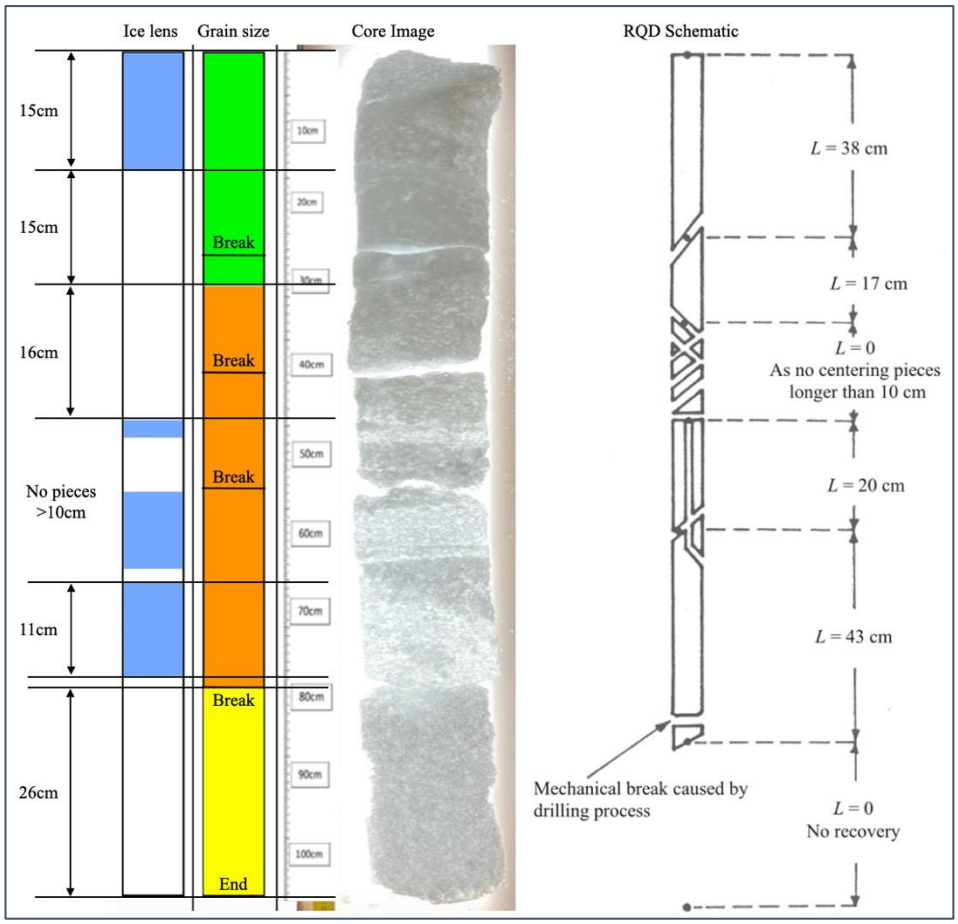

Figure 3-14: Rock Quality Designation determination method

The uncertainty of each RQD value was based off the equipment used to carry out the measurements. The tape measure used for the RQD measurements had a random error of limitation, giving an uncertainty of 0.5mm for each measurement. As the summation of >10cm

section lengths was calculated, value of uncertainty was summed for each section measured. For example, the core shown in Figure 3-14 above showed 5 sections, leading to an uncertainty calculation of 2.5mm. For the RQD, the percentage uncertainties of parameters in Equation 2-9 were calculated and summed to give the total uncertainty of each measurement. Systematic errors were however mitigated by using the same tape measure to measure all core sections.

3.6 Morphology test procedures

3.6.1 Thin section preparation

Thin sections were described as thickness of ice where the crystal structure arrangement in the ice samples can be observed. Sinha & Shokr (2015) provided a comprehensive list of methods used to view thin sections. The methods listed include using polarising microscopes, handheld polariscopes, and the cross polarising after double microtoming a sample. Among these, the Double Microtoming Technique (DMT) was chosen for use due to a number of factors. Firstly, the technique did not require extensive training or use of trained professionals as the microscope techniques would. Secondly, the equipment used for the technique was tried and tested to be more resilient to the cold temperatures as opposed to microscopes and polariscopes. The DMT was therefore performed in the UCT polar engineering laboratory. Multiple authors such as Petrovic (2003), Shazly *et al.* (2009), Bassis & Walker (2012), and Yasui *et al.* (2017) carried out their experiments on ice samples in cold laboratories at -10°C, which was a starting basis for the tests carried out.

The DMT method described by Sinha & Shokr (2015) involved the use of microtome cut surfaces as the bases of ice sample slices used for analysis. Firstly, a thin slice of ice of about 10mm was cut using a bandsaw. The cut end of the slice where the bandsaw passed was stuck on a glass slide using the flash freezing action of water in the cold laboratory. Using water at room temperature, drops of water were placed onto a glass slide to touch the side of the ice sample. A dropper was used for this. Due to the temperature difference between the water and surfaces it was touching, freezing was immediately supposed to occur to stick the ice onto the glass slide. However, the action was delayed with the laboratory at -10°C. This prompted setting the new laboratory temperature at -17.5°C (±2.5°C due to defrost cycles) which enabled the flash freezing process to occur. The top side of the slice was trimmed to an even level using a microtome to obtain a perfectly flat surface parallel to the glass slide below. Glass slides were used due to their transparent nature, allowing light to pass through undisturbed and directly to the ice samples.

To the new microtome cut face of ice, another glass slide was placed and stuck using water flash freezing. An ice sandwich was then formed using the two glass slides at the ends and the ice sample in the middle. The sandwich was once again pushed through a bandsaw to cut it into two separate samples. The sample with the microtome cut face on the glass slide was taken as the primary sample and placed into the microtome again for further trimming. This therefore ensured that both sides of the sample were cut perfectly flat using the microtome.

The cutting process was a repetitive shaving process where microns of ice were shaved off till the required thickness was obtained. Starting with a sample of about 2mm, 40µm cuts were used. This value drops to 20µm at about 0.5mm thickness, 10µm and 5µm at smaller thicknesses of the ice sample. When the sample was within the 100µm to 30µm thickness range, the ice shaving was concluded and sample placed under cross polarised light (Sinha & Shokr, 2015). The DMT process has been summarised into Figure 3-15 below.

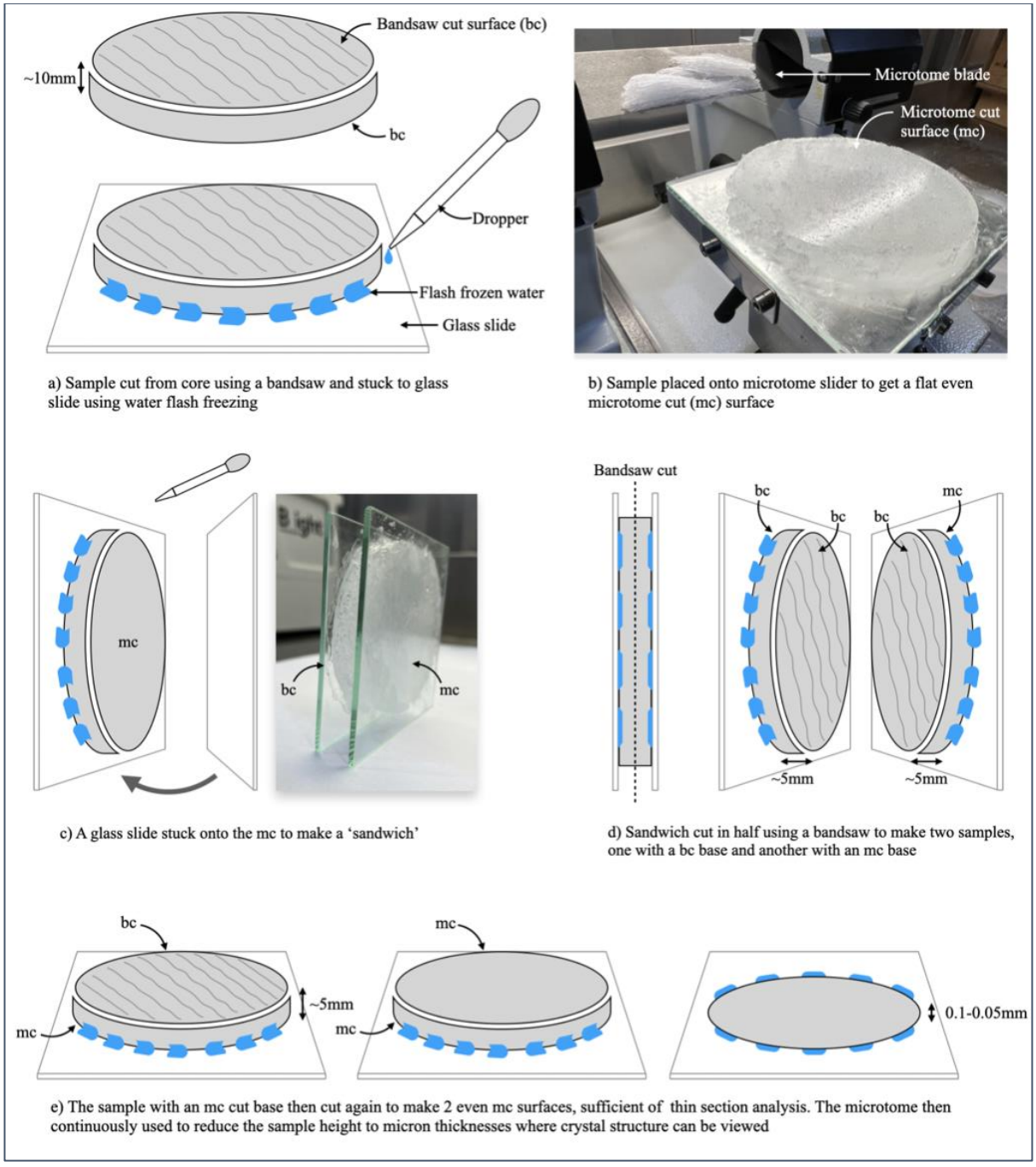

Figure 3-15: Double Mictroming Technique

3.6.2 Crystal and granular structure reading

There were two types of ice found in the cores retrieved from the shelf edge. Majority of the ice was granular in nature, originating from refrozen snow particles. The other type was the crystalline form which were ice lenses within the granular matrixes, which were formed through re-freezing of melt water inside granular ice.

The DMT method was effectively carried out on the crystalline ice lenses showing clear crystal structures under cross polarised light as observed in Figure 3-16. Similarly, the DMT was also attempted for the granular ice samples but proved to be detrimental to the samples. Due to the granular nature of the samples, pieces of the samples began to chip away during the DMT as the thickness of the samples reduced. This therefore inhibited the use of thin section analysis on granular samples. To remedy this, a grainsize selection approach was used as described in the next Section.

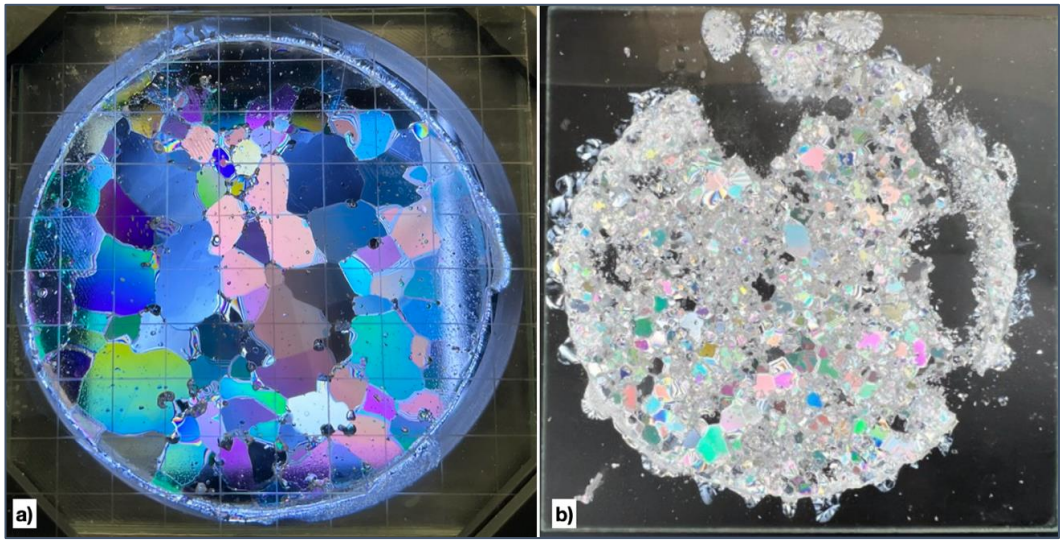

Figure 3-16: **a** Crystalline sample; **b** Granular sample

3.6.3 Grainsize selection

In addition to the difference between the granular ice and ice lenses, there was also a visual difference observed between the various granular core sections. From a visual inspection, some granular particles were observed to be larger than others. The sections with large granular particles were seen to permit more light through them, as opposed to the finer granular sections which appeared darker over a light box. This was therefore adopted as the method of determining the general size range of the granular sections. This method of determining the general size range was also adopted by MacDonell *et al.* (2021) in Figure 3-17 to characterise their firn cores from Antarctic firn aquifer. To quantify the amount of each of the grainsizes in the cores, the percentage length of each of the grainsizes was calculated for each core. This was done by identifying all the grainsizes in a core, measuring the heights of each grainsize section on the

core, then summing the lengths for each grainsize to obtain its proportion to the total core length. The equation used to calculate this percentage in given below.

$$Grainsize\ \% = \frac{\Sigma\ Grainsize\ lengths\ in\ core\ (mm)}{Total\ core\ length\ (mm)} \times 100 \qquad \text{Equation 3-1}$$

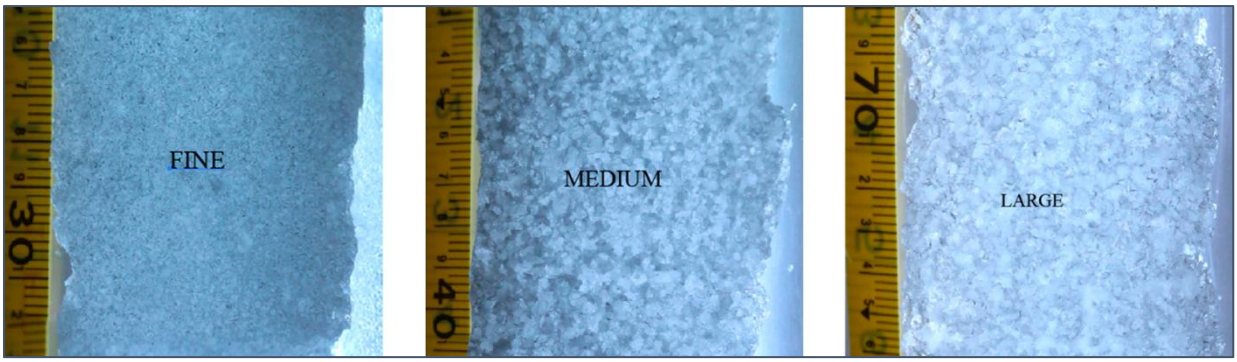

Figure 3-17: Grainsize determination method by MacDonell *et al.* (2021)

3.7 Physical property test procedures

3.7.1 Density tests

Following the information learned from authors in Chapter 2.2.1, density readings were considered highly critical to this study. This was not only due to the number of properties related to density, but also the classification of authors such as Wang, E. *et al.* (2021) mentioning density as the most important characterisation parameter for both ice and snow. This importance of density necessitated the need to adopt a well-documented and backed method to obtain acceptable values.

From Table 2-1, the hydrostatic method following Archimedes principle was investigated as the most accurate method to determine density. However, the method was flawed in its application to samples such as the Antarctic granular ice being dealt with. Firstly, the preparation of samples for the hydrostatic method is considerably difficult and time consuming. Secondly, with samples being majorly granular, submersion of the samples into a non-freeze liquid would allow the liquid to seep into the air-filled pores and overestimate density readings (Pustogvar & Kulyakhtin, 2016). Due to these drawbacks of the hydrostatic method, the mass/volume method was then chosen to be used. It was pointed out as the second most accurate of the methods tested and most used by authors such as Rist *et al.* (2002), Wang, Q. *et al.* (2018), and Han *et al.* (2015). Use of this reputable method also aided in the mitigation of systematic errors to the study.

Among the cores obtained from the Fimbul ice shelf, specific density measurement cores were selected and solely partitioned to be used for density measurements. In addition to these cores, the samples prepared for compressive strength tests were also used for density measurements, a method also used by Rist *et al.* (2002). To accurately determine densities of

singly grained core samples, homogenous sections were used for these readings. For this, samples obtained from the density cores were cut using a bandsaw to heights ranging from 50mm - 120mm, depending on the uniformity of the core (Han *et al.*, 2015). In addition to the homogenous samples, density tests on non-homogenous or mixed samples for compression tests were also carried out. These mixed samples contained different grainsizes and ice lenses.

The diameters and heights of the samples were measured using a vernier callipers to obtain millimetre (mm) readings to the nearest hundredth as used by Wang, Q. *et al.* (2018). The diameter and height readings got using a vernier callipers were each carried out 3 times for a single sample. The average of the 3 reading was there after calculated and used for further calculations. This method was recommended by Hutchings *et al.* (2015) as a way of reducing the random errors incurred during the measurements. Using the dimensions measured, the volumes of the samples were calculated using Equation 3-3. The masses of the same ice samples were measured using a mass balance and then divided by the volume to give the densities of the samples as seen in Equation 3-2. The mass balance and vernier callipers used had a random error of 0.001g and 0.01mm respectively. In addition to the density, porosity of each of the samples was calculated using Equation 3-4 below as function of the densities obtained.

$$\rho_i = \frac{m}{v} \qquad \text{Equation 3-2}$$

$$v = \frac{\pi D^2}{4} \times H \qquad \text{Equation 3-3}$$

$$Porosity = \left(1 - \frac{\rho_i}{\rho_m}\right) \times 100 \qquad \text{Equation 3-4}$$

where ρ_i = density,

ρ_m = material density,

m = mass,

v = volume,

D = average of diameter readings, and

H = average of height readings.

3.7.2 Elastic Modulus & Poisson's ratio tests

The two documented types of tests carried out to determine material moduli include the static and dynamic methods where the static methods involve direct measurement of deformations on tests samples while the dynamic methods carried out by measuring the speed of sound through a medium (Brotons *et al.*, 2016). In addition to these descriptions, the static tests were also classified as the destructive tests, while the dynamic tests were described as non-destructive.

With the static tests ultimately leading to the destruction of samples, the test method would require higher amounts of time and cost in the acquisition and preparation of samples (Pappalardo & Mineo, 2022).

Due to the mentioned limitations to the static method, the dynamic testing method was adopted. Dynamic testing proved more logical due to its none destructive nature and limited samples obtained, its previous applications for ice in literature, and the availability of a highly capable ultrasound setup used in Skatulla *et al.* (2022). The ultrasound setup was also tested to work comfortably in the -17.5±2.5°C temperature at which the lab results were taken.

Each of the samples used for the tests mentioned were cylindrical in nature with diameters of approximately 90mm. Both top and bottom edges of the samples were cut perpendicular to the height of the samples using a bandsaw. The sample ends were set up to be cut as straight as possible using the sliding tray of the bandsaw, cutting the samples in one straight plane along the diameter. To each of the cut areas of the samples, a highly viscous gel was applied to function as a coupling for the ultrasound transducers. The viscous gel applied onto the ice for the readings was HTS silicone grease which is a light duty general purpose lubricant approved for use in low temperatures. This method was carried out by Brotons *et al.* (2016) and Pappalardo & Mineo (2022) as well. A thin grease layer of about 0.5mm was applied to the diameter ends of test samples to improve the contact patch of the ultrasound transducers on the ice. In the case where granular samples with uneven ends were to be tested, a thicker film of grease was applied to fill the air voids between ice grains and to directly transmit the ultrasonic waves into the ice.

To then prepare the machine to take readings, the computer was turned on and a calibration done. This was carried out before each testing session to ensure correctly calibrated readings throughout the day. To achieve this, the transducers were connected to the computer and used to take a measurement of the calibration rod in Figure 3-6. Once correctly calibrated and showing the 25.4μm on the rod, the activity was concluded, and ice measurement commenced.

A transducer was placed on both diameter sides of the sample to be tested. The transducers were placed parallel to one another in order not to distort the wave readings viewed on the computer screen. When the transducers were in place and held in a firm stable manner, the test was begun by pressing ‘Play’ on the screen to output the waves observed in Figure 3-18. Once the waves on the screen were stable and constant, the ‘Stop’ on the screen was pressed to freeze the wave for measurement.

The output from the test scenarios were signal curves showing both the P and S waves. Time taken for each of the waves to arrive provided an oscillating signal curve seen on the screen of measuring device. The time taken for the first wave to begin was taken as the time taken by the P wave and the first significant drop in the wave amplitude to a trough was taken as the time taken by the S wave as seen in Figure 3-18. Using the times measured and the distances between transducers or height of the sample, the velocity of sound through the sample was calculated by dividing the distance by the time taken.

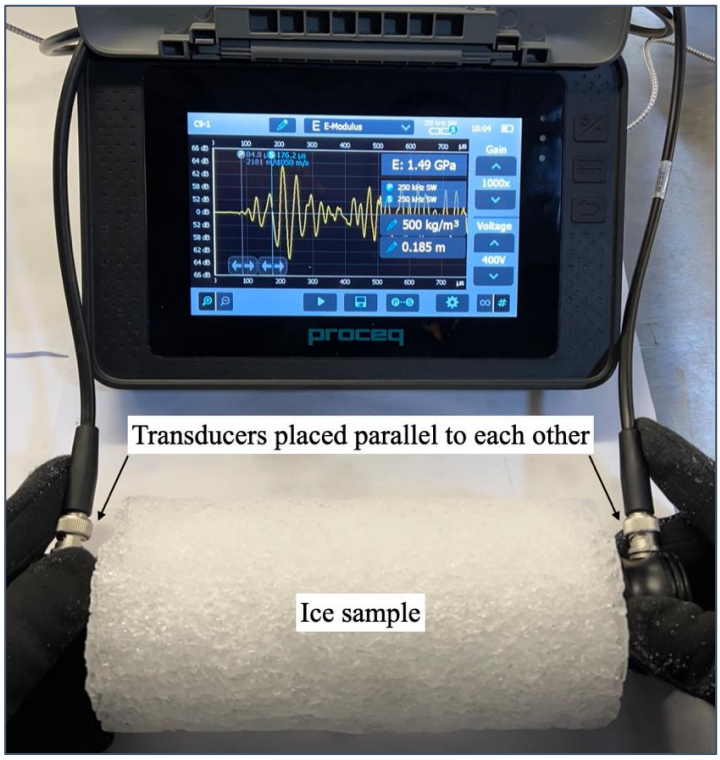

Figure 3-18: Ultrasound test method

Wyllie & Mah (2004) describe seismic methods to determine Young's modulus and Poisson's ratio using energy sources like hammers or small explosions and receiving transducers to measure the relative arrive times of waves caused by the impacts in rock. With the same formula, the transducers placed at known distances from the energy sources henceforth calculate the velocities of the P and S waves from the arrival times measured. Approximate P wave velocities can be determined using Figure 3-19. The velocities of the waves are related to the elastic properties of rock through the following equations:

$$V_p = \left(\frac{E + {}^{4G}/_{3}}{\gamma}\right)^{0.5} \qquad \text{Equation 3-5}$$

$$V_s = \left(\frac{G}{\gamma}\right)^{0.5} \qquad \text{Equation 3-6}$$

where V_p = pressure wave velocity,

V_s = shear wave velocity,

E = elastic modulus,

G = shear modulus, and

γ = unit weight of the rock (Wyllie & Mah, 2004).

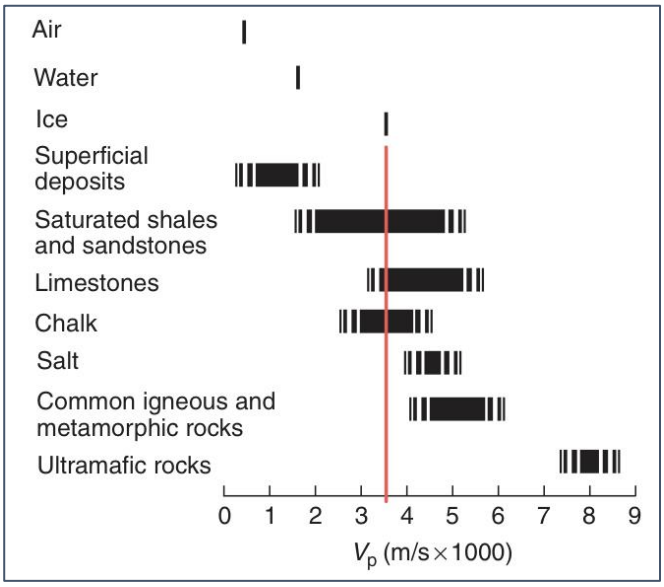

Figure 3-19: Approximate Primary velocity (Vp) values for various materials (Wyllie & Mah, 2004)

The densities of the ice samples were obtained before the ultrasound testing using Equation 3-2 and Equation 3-3 because of their role as an input into the calculations for elastic modulus. Poisson's ratio on the other hand did not require densities to be calculated based on the equations used. The density, length measurement and the internal machine calibration errors were therefore the only sources uncertainty noted during the experiments. With reference to Equation 3-5 and Equation 3-6, the shear modulus, elastic modulus and Poisson's ratio were determined using the following equations:

$$V_i = \frac{H}{t_i} \qquad \text{Equation 3-7}$$

$$M = \rho \times {V_p}^2 \qquad \text{Equation 3-8}$$

$$G = \rho \times {V_s}^2 \qquad \text{Equation 3-9}$$

$$\nu = \frac{M - 2G}{2M - 2G} = \frac{{V_p}^2 - 2{V_s}^2}{2\left({V_p}^2 - {V_s}^2\right)} \qquad \text{Equation 3-10}$$

$$E = 2G(1 + \nu) \qquad \text{Equation 3-11}$$

where V_i = P and S wave velocities,

H = height of sample,

t_i = ultrasound time measured,

M = pressure wave modulus,

G = shear modulus,

ρ = density of the sample and

ν = Poisson's ratio.

3.8 Strength test procedures

Together with the physical properties of the Fimbul shelf ice obtained, the strength properties were also a major requirement to achieve the objectives of this study. The strength parameters investigated were therefore UCS, shear strength, and tensile strength.

3.8.1 UCS test procedure

Uniaxial compressive strength tests on ice are currently carried out without the use of a documented standard method. To therefore carry out the tests to an acceptable and repeatable standard, a geotechnical engineering approach to UCS was adopted (Wang, E. *et al.*, 2021). Cores that were retrieved from Antarctica were about 1000mm in total length. Through the initial visual assessment of the cores, sections of a sufficient length of about 180mm were looked for to be used in UCS tests. However, during transportation and storage of cores from the Antarctic to UCT, a number of the cores experienced breakages along their lengths. Due to this, selection of sample lengths for tests was entirely dependent on the position of breakages within the core length.

To produce representative strength values of the top shelf ice layer, both homogenous and mixed ice samples were chosen to be tested. The homogenous samples were entirely of the same grainsize or structure, while the mixed samples contained different grainsizes and structures within. This also played a role in maximising the usage of the limited number of ice cores obtained.

During sample preparation, core sections of height greater than 180mm were selected. These sections were then measured using a tape measure and cut using a bandsaw to the heights of about 180mm. The diameter and specific height dimensions of all the samples cut were then measured using vernier callipers. Diameters and heights were each measured 3 times across the sample to obtain averages of the sample size to reduce the error and be used for further analysis.

The compression machine used worked hand-in-hand with an application installed on a mobile device. The application was used to connect with the machine through a Bluetooth link and acted as a display for the relevant test information from the machine. The app used for the compression tests was called Point Load Test developed by GCTS. The app interface enabled the selection of preferred settings, automatic and manual calibrations, setting up projects, and viewing results from past projects saved on the app. The settings used for the app have been summarised in Table 3-1. The calibrations used of the machine, as seen in the app are displayed in Table 3-2.

Table 3-1: PLT mobile application settings used

App Setting	Selection	Reason
Unit selection	Off	'Off' used SI units while 'On' used USCS units
Automatic mode	Off	Variable samples
Variable specimen	On	Variable sample dimensions
Read load	1.00kN	To prevent load reading during test preparation

Table 3-2: PLT sensor calibration results

Calibration information	Result
Calibration date	16/03/2022
Linear value	$19.633x - 1.226 = load\ value$
R^2	1.000
Maximum error (kN)	0.115
Maximum % error (%)	0.12
3rd degree polynomial	$-0.002x^3 - 0.019x^2 + 19.784x - 1.388 = load\ value$
R^2	1.000
Maximum error (kN)	0.058
Maximum % error (%)	0.06

In order to maintain an organised thread of data storage on the app, a new project was begun for each core tested. The number of samples tested per core therefore represented the number of samples obtained from the respective core. To carry out the compression test, the app required input data about the samples to be tested. This included the diameter, height, and orientation of the sample. The diameter and height values obtained prior to the test were put into the app with the section of a vertical uniaxial compression orientation on a cylinder, as opposed to a horizontal compression on a cylinder or irregular shape. After completing the app setup, the testing was ready to commence.

Placing a sample between the two platens, as observed in Figure 3-20, the bottom platen was raised using the pump to allow the sample to contact the top platen. Once contact was confirmed by an increase in load on the app screen, the initial height (h_i) of the bottom platen was measured using a vernier calliper and recorded. Further pumping then commenced to begin the compression test with a graph of load vs time beginning to form on the app screen.

The pumping process was aimed to be as slow as possible to stay within the strain rate regime for ductile failure. This was to simulate the slow loading process of snow and ice on the ice shelf through snow accumulation. The aim was to have a single pump stroke per minute with one rebound where the handle was lifted from loaded to begin a new stoke. On the rebound, reapplication of the load was made as smooth as possible to prevent a spike in the load on the ice due to stress hardening. The pumping was noted to be a source of human error in the experiments.

To mitigate this, the timing of the revolutions was crucial. The other sources of error were the machine internal calibrations and equipment used to measure length and time.

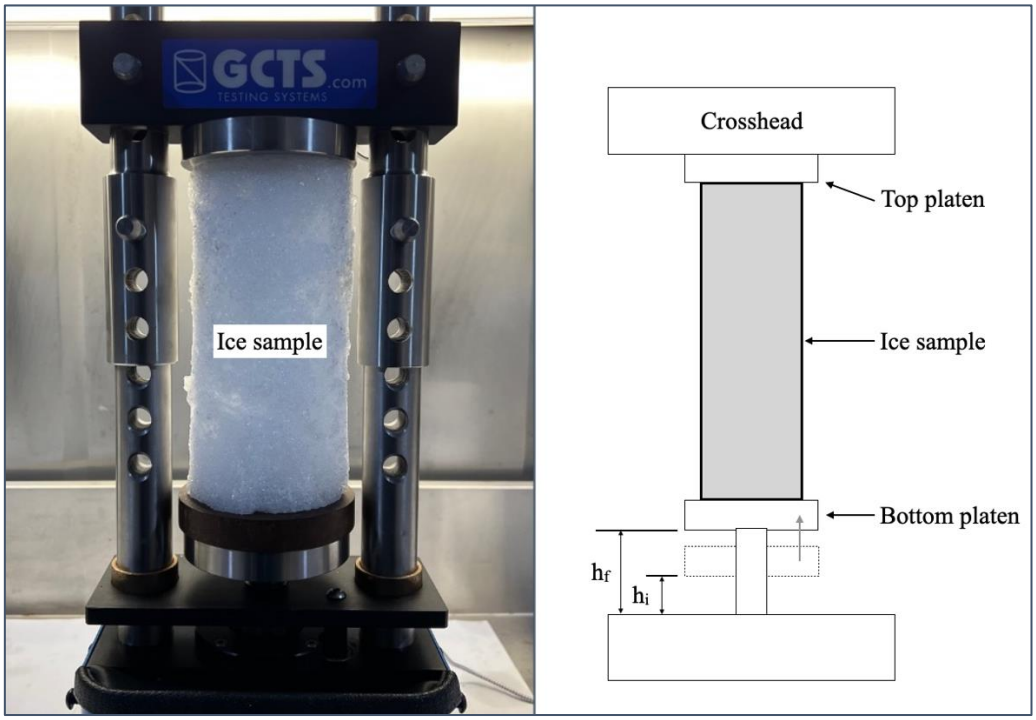

Figure 3-20: Compression test setup

The pumping processes was continued at the same rate until there was no more load increase displayed on the graph. This was seen after the peak load was clearly recorded by the app and there was no increase in stress during a further application of the load. At a time of 400s or 500s, based on material behaviour, the tests were stopped and a final reading of displacement of the bottom platen was measured and recorded (h_f). The initial and final readings of the displacements were used to determine the strain during the test. The strain was then coupled with the time spent during a test to determine the average strain rate during the test following the Equations below. The failure load was also recorded on the app as the peak load. This was then used to determine the failure stress and hence the UCS of the sample.

$$\varepsilon = \frac{h_f - h_i}{L} \qquad \text{Equation 3-12}$$

$$Stain\ rate = \frac{\varepsilon}{\Delta t} \qquad \text{Equation 3-13}$$

where ε = strain,

h_f = final displacement reading,

h_i = initial displacement reading,

L = sample height, and

Δt = time taken

3.8.2 Shear strength procedure

Shear strength has been mentioned as the governing parameter for failure in not only geotechnical materials but also ice as well. Authors like Kulyakhtin & Høyland (2014), Podolskiy *et al.* (2015), and Serré (2011) use the Mohr Coulomb failure criterion to model and describe failure characteristics of ice masses. The Mohr Coulomb criterion is a shear strength failure mechanism with a formation shown in Equation 2-3. The input parameters for the equation are cohesion, angle of friction, and normal stress. To obtain the shear strength parameters for ice, the normal stress was taken as the UCS tested in Chapter 3.8.1 above, while the cohesion and angle of friction were determined using the RMR rock classification method below.

3.8.2.1 Rock Mass Rating

The RMR method was adopted due to the number of constraints experienced in data collection. These included the type of materials collected, the method of material collection, and the machinery available to analyse the materials collected. The method was developed in the South African CSIR by Bieniawski (1979). Different versions of the method have been produced (Singh & Goel, 1999) and the versions used were the original 1979 version and the RMR 1989.

This particular rock classification system was chosen due to the similarities between ice and rock that were found and detailed in Section 2.8 with authors like Schulson (2001) showing similarities between ice characteristics and those of granite. In addition to the similarities, the author also related the rate of crack nucleation in ice to a cohesion parameter, which was one of the RMR outputs. The RMR ultimately output shear strength properties, cohesion and angle of friction, which were required for slope stability modelling of the ice. Third was the limited availability of data from the ice shelf leaving RMR as the best fitting option.

The RMR considers 6 parameters which include UCS, RQD, discontinuity spacing, discontinuity conditions, ground water conditions, and discontinuity orientations (Kundu *et al.*, 2020). However, the first 5 parameters can be referred to as the basic RMR (Singh & Goel, 1999). Due to the low resource intensity and adaptability of the method, the RMR was incorporated into the analysis of the ice core samples obtained. The UCS of the samples was obtained using the compressive strength tests explained in Chapter 3.8.1. The values of strength obtained were then compared to the UCS table for the RMR method in Table 3-3. The RQD was also calculated as described in Chapter 3.5.1.3, giving results that were placed in the RMR table for RQD seen in Table 3-4. The discontinuity spacing was then obtained using a visual assessment of the ice cores. Discontinuities in the cores were chosen as the changes in grainsize and existence of ice lenses. Whenever an ice lens or a change in grainsize was encountered on a core, the distance between it and the next discontinuity was read and recorded. To select a value for the RMR parameter,

the smallest discontinuity value of each core was obtained, and an average determined for the entire data set. The average value was then placed within the ranges shown in Table 3-5 to obtain the RMR parameter.

Table 3-3: UCS of intact rock (Bieniawski, 1979)

Qualitative description	Compressive strength (MPa)	Rating
Exceptionally strong	>250	15
Very strong	100 - 250	12
Strong	50 - 100	7
Average	25 - 50	4
Weak	10 - 25	2
Very weak	2 - 10	1
Extremely weak	1 - 2	0

Table 3-4: RQD ratings (Bieniawski, 1979)

Qualitative description	RQD (%)	Rating
Excellent	90 - 100	20
Good	75 - 90	17
Fair	50 - 75	13
Poor	25 - 50	8
Very poor	<25	3

Table 3-5: Discontinuity spacing (Bieniawski, 1979)

Description	Spacing (mm)	Rating
Very wide	>2	20
Wide	0.6 - 2	15
Moderate	0.2 - 0.6	10
Close	0.06 - 0.2	8
Very close	<0.06	5

Unlike the UCS, RQD, and discontinuity spacing parameters, the discontinuity condition and ground water parameters were determined subjectively through assessment of the cores obtained and site characteristics. The discontinuity condition was assessed by observing the interface between firstly, changing grainsizes and secondly, granular ice and ice lenses. When compared to the descriptions mentioned in Table 3-6, the description that best described the interfaces was slickensided, due to the smooth and relatively slippery interface between granular ice and solid ice lenses. The ground water conditions were then assessed using both site conditions and cores obtained. Being an icy site, presence of water on the ice shelf was relatively rare as water in those temperatures froze at fast rates. The cores retrieved also showed no signs

of wetness, thus leading to the conclusion of dry groundwater conditions on the shelf. The completely dry rating was then chosen in Table 3-7.

Table 3-6: Condition of discontinuities (Bieniawski, 1979)

Description	Rating
Very rough and unweathered, wall rock tight and discontinuous, no separation	30
Rough and slightly weathered, wall rock surface separation <1mm	25
Slightly rough and moderately to highly weathered, wall rock separation <1mm	20
Slickensided wall surface or 1 – 5mm thick gouge or 1 – 5mm wide continuous discontinuity	10
5mm thick soft gouge, 5mm wide continuous discontinuity	0

Table 3-7: Ground water condition (Bieniawski, 1979)

Joint Water Pressure	General description	Rating
0	Completely dry	15
0 – 0.1	Damp	10
0.1 – 0.2	Wet	7
0.2 – 0.5	Dripping	4
>0.5	Flowing	0

The parameters obtained each gave an RMR value which were all added up to give the basic RMR rating for the material. The sixth parameter was the discontinuity orientation which was based on the strike and dip measurements of discontinuities. Due to the horizontal layering of the shelf ice caused by repetitive process of snow fall, consolidation, and further bonding due to overburden pressure from new snow fall, the arrangement of discontinuities was seen on be nearly horizontal throughout the site on the shelf edge. This was seen through radargrams taken on the site and the horizontal orientation of ice lenses and grainsize changes in the ice cores. The discontinuity orientation is a negative rating to the basic RMR, with a value obtained being subtracted from the basic RMR to give the final RMR value. The flat and horizontal nature of the discontinuities seen informed the decision to assign a zero rating to the discontinuity orientation rating, making the basic RMR equal to the final RMR.

The final RMR was finally placed into an RMR rock class as seen in Table 3-8 to obtain the estimate rock property values of the Fimbul granular ice layer. It is mentioned that the RMR values carry validity for use in slopes and predesign scenarios (Aksoy, 2008), making them sufficient for use in obtaining the estimate cohesion and friction angle for the ice. These parameters played a key role in the determination of the shear strength of a material and have therefore been used to determine the shear strength of the ice in the coming Section.

Table 3-8: RMR engineering properties based off Bieniawski (1979)

RMR Rock Class	Classification	Cohesion (MPa)	Angle of friction (º)
100 – 81 (I)	Very good	>0.4	>45
80 – 61 (II)	Good	0.3 – 0.4	35 - 45
60 – 41 (III)	Fair	0.2 – 0.3	25 - 35
40 – 21 (IV)	Poor	0.1 – 0.2	15 - 25
<20 (V)	Very poor	<0.1	15

In addition to the shear strength, the value used for cohesion was also used as the Tensile strength of the materials. This was chosen following the method by Podolskiy *et al.* (2015) who stated the tensile strength of ice being equal to the cohesion or freeze bond strength in the material. This was further supported by authors like Kulyakhtin & Høyland (2014) and Serré (2011).

3.8.2.2 Shear strength determination

Determination of the ice shear strength was the intended aim of the UCS tests carried out. The uniaxial strength tests were carried out on the ice samples and the results statistically analysed to obtain an average value with a standard deviation. Following that, the RMR method was carried out to obtain an RMR class which, according to Singh & Goel (1999), gives a range of cohesion and angle of friction values to be used. Having obtained the UCS to give the value of σ', and RMR to give the values of c and ϕ, all the parameters used to determine shear strength were obtained using the shear strength equation below.

$$\tau = c + \sigma' tan\phi \qquad \text{Equation 3-14}$$

where τ = shear stress,

c = cohesion,

σ' = effective normal stress, and

ϕ = angle of friction.

In addition to the RMR method, Singh & Goel (1999) advise the inclusion of the numerical modelling to further analyse a material due to the preliminary nature of the RMR values obtained. With this and as part of the research objectives, slope stability modelling was carried out in the next Section.

Part IV: Cliff stability modelling

This Part describes the methods used to carry out a cliff stability assessment based off the material parameters obtained using methods in the earlier Sections. A combination of information obtained through the literature review, material characterisation, physical, and strength parameters informed the development of the processes described. Due to the differences in glacial and geotechnical nomenclature, the terms slope stability and cliff stability were used interchangeably in this Section as the cliff was analysed as a vertical slope.

3.9 Model build

3.9.1 Software used

The first step in modelling the cliff was building a model cliff in the slope stability software relatively accurate to the appearance and dimensions of the real cliff. Following the assessment carried out for Table 2-3, Rocscience's RS2 was selected for the slope stability analysis for a number of reasons. Firstly, it incorporated a Finite Element Method (FEM) which was required to model the complex behavioural characteristics of ice. Secondly, it had a relatively low learning curve as opposed to other software types with the command driven modelling. Finally, it had a specific focus on slope stability modelling and a low resource intensity when compared to other software. This was further influenced by the minimal amount of information available about the Antarctic ice obtained.

Rocscience software packages were commonly used due to their, ease of use, connectivity, and versatility, with data transferable from one package to another. Examples of this are Alemdag *et al.* (2014) using Rocscience's RocPlane to analyse planar failure and Jiang *et al.* (2013) using SWedge for wedge failure analysis. An example of RS2's numerical modelling usage was in Alemdag *et al.* (2014) where the slope analysis was carried out using RS2's Strength Reduction Factor (SRF) modelling of a slope before and after excavation.

3.9.2 Project settings

Before any geometry building, the project settings of the analysis were set as shown in Figure 3-21. This mainly involved information on the type of model that was going to be built and the way the software would carry out the analysis. Firstly, the plain strain analysis was selected for the model as opposed to an axisymmetric type of analysis. The plain strain analysis assumed an infinite length of material normal to the 2D model drawn on the interface which is representative of the ice shelf. Secondly, viscous properties were enabled in the analysis due to the fact that ice is commonly referred to as a viscoelastic material, defined by Sinha (1989), Han *et al.* (2015), and Wang, E. *et al.* (2021). Thirdly, both thermal and dynamic properties were not considered in this research due to the limited scope and data available for those kinds of analysis, and then a static ground water method was chosen as opposed to a steady state or transient Finite Element

Analysis (FEA). This was chosen due to the unavailability of data about seepage of water into the ice shelf, or its possible influence on slope failure. Finally, the shear reduction factor (SRF) method was selected for this analysis, with an automatic step size and tolerance of 0.01. This would be used to provide a factor of safety (FS) for the cliff following Equation 3-15 below. Following this, SRF and FS were used interchangeably in the study.

$$SRF = FS = \frac{Material\ c}{Reduced\ c} = \frac{Material\ \phi}{Reduced\ \phi} \qquad \text{Equation 3-15}$$

where c = cohesion,

ϕ = angle of friction,

SRF = shear reduction factor, and

FS = factor of safety.

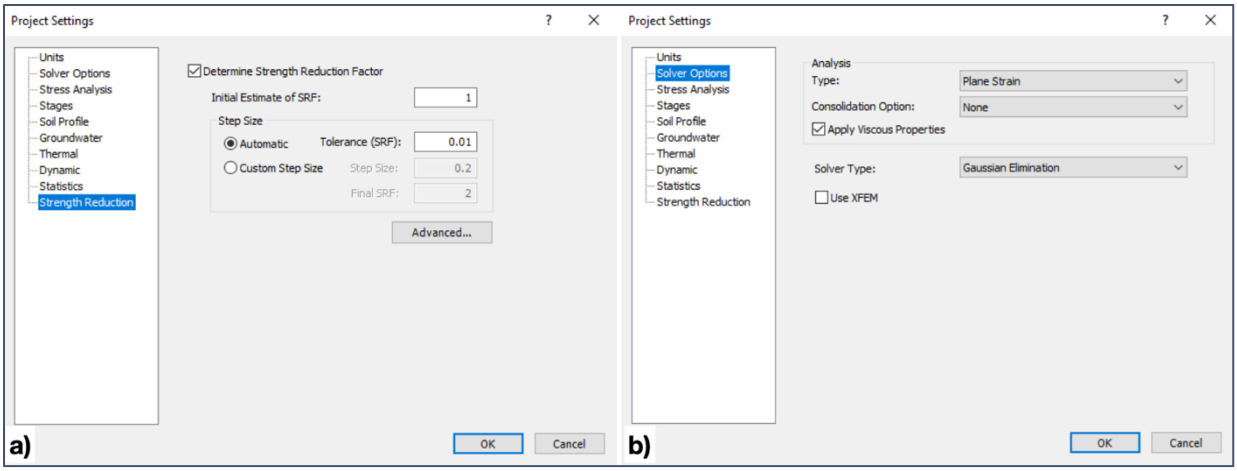

Figure 3-21: **a** SRF settings; **b** Solver options

3.9.3 Model boundaries

Having set out the project settings, the boundaries of the cliff were then drawn. The ice shelf was drawn to a total height of 100m following information on the Fimbul shelf by Nøst (2004) and as observed in Figure 3-22. The 100m cliff was modelled as a 90º vertical cliff, with the ice mass extended to 200m in-land to encompass the study area. 2 material boundaries were then drawn within the cliff model to simulate 3 distinct material types. The top layer (0m - 20m) was comprised of the granular layer of ice. This was informed by deep coring in Antarctica carried out MacDonell *et al.* (2021) where granular ice with ice lenses, similar to the ice obtained in the study area, was observed at depths of 18m below the surface. The middle layer (20m - 50m) was labelled the upper firn layer to provide a smoother transition of properties to the third layer, and the bottom layer (50m - 100m) was labelled as lower firn ice. These layers were all placed into

a rectangular model of the cliff, which is a common ice cliff model shape used by other authors like Bassis & Walker (2012), Bassis *et al.* (2021), and Crawford *et al.* (2021).

To define the model position in space, roller connections were placed at the bottom and end of the model away from the free standing cliff. The bottom of the model was given a roller permitting movement in the *x*-axis, while fixing movement in the *y*-axis. The horizontal movement was released to enable deformation of the cliff in case failure required horizontal transition of the entire ice mass. On the other hand, the *y*-axis was fixed to simulate hydrostatic equilibrium keeping the shelf afloat. This was noticeably different to the floating ice shelf in reality, but due to the limited information about the vertical support offered to the shelf by ice further inland, the vertical hydrostatic equilibrium was assumed.

On the far end away from the cliff edge, the rollers used permitted movement in the *y*-axis and fixed movement in the *x*-axis. The *y*-axis was released to work in conjunction with the *x*-axis freedom of movement at the bottom of the model, permitting vertical deformation of the model. The *x*-axis fixity was used to represent the connection between the study area being modelled and the rest of the Fimbul ice shelf further inland which restricted movement in that direction.

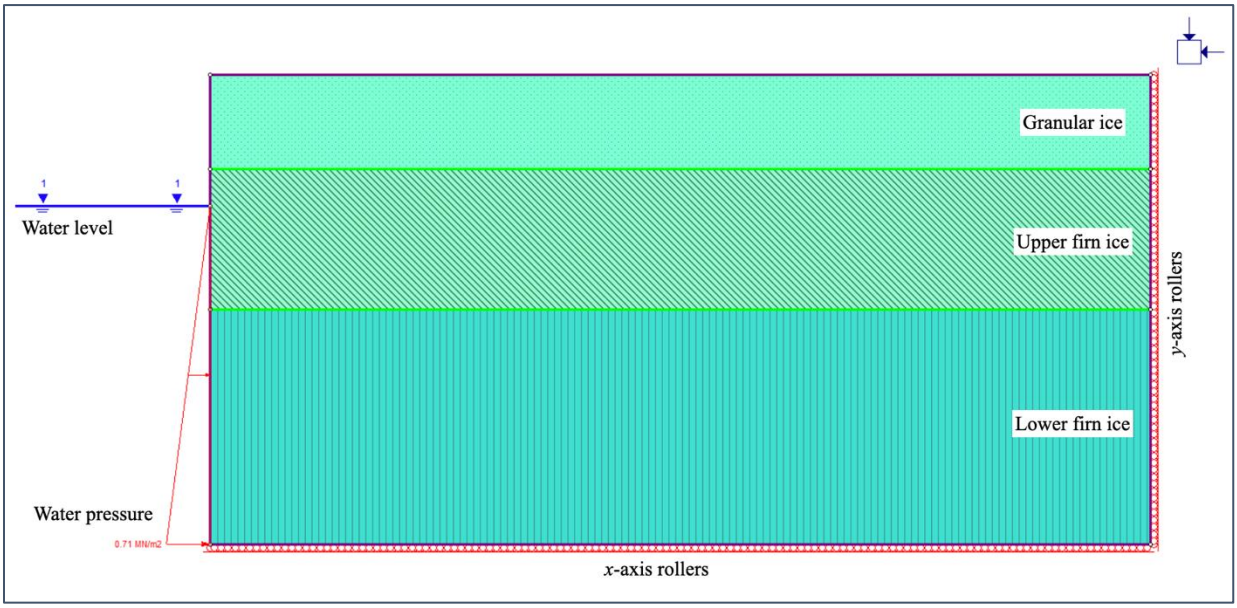

Figure 3-22: 2-dimensional Base shelf model

According to the height readings from SA Agulhas II, the cliff stood at a height approximately 28m above the water level. To model this, a piezometric line was placed 28m below the top of the model which extended away from the cliff. To model the water pressure on the cliff, a linearly distributed load (LDL) was placed with an origin of 0kPa at the surface of the water to 710kPa or 0.71MPa at the bottom of the shelf, 72m below the water level. Having built the model, the material properties were then input based on test results and information from various literature sources. This is expanded on in the next Section.

3.10 Input parameters

The three ice material types used; granular ice, upper firn ice, and lower firn ice, each required material parameter inputs to define the properties and behaviours of the materials. The key parameters inputs for the model were unit weights, porosity, elastic moduli, Poisson's ratio, cohesion, and friction angles. These were mainly dictated by the material type and the Mohr Coulomb failure criterion selected for the ice cliff due to backing from a number of published authors like Ji *et al.* (2017), Podolskiy *et al.* (2015), and Reiweger *et al.* (2015).

Granular ice material properties in the top layer were obtained from laboratory testing on the ice samples from the shelf. The unit weight and porosity were calculated from density results, elastic modulus and Poisson's ratio from ultrasound tests, then cohesion and friction angle from RMR, and tensile strength equal to the cohesion values obtained. The drainage properties were then set to drained to simulate dry cliff conditions. This setting was also used in the upper and lower firn ice inputs.

The upper firn ice density and elastic properties were obtained from Rist *et al.* (2002) property curve while the rest of the properties were interpolated between values from the upper and lower ice materials. The lower firn layer properties were purely obtained from literature sources. The density used was obtained from White & McCallum (2018) and Bassis & Walker (2012). The *E* modulus was an average of results by Yasui *et al.* (2017) and Petrovic (2003). The Poisson's ratio used was obtained by both Petrovic (2003) and Sinha (1989), while the cohesion value was obtained from Bassis & Walker (2012). The angle of friction was averaged from ranges used by Schulson (2001) and Serré (2011) and finally tensile strength got from Podolskiy *et al.* (2015).

3.11 Model analysis

To begin analysis of the shelf edge model, a FE mesh needed to be generated. The RS2 software could be used to automatically generate a number of mesh types which include uniform, graded, and radial meshes. For the ice cliff modelled, the graded mesh option was chosen due to the higher concentration of mesh elements at areas of higher concern like the cliff edge and material boundaries. Before a mesh setting was chosen, a sensitivity analysis was carried out to determine the most accurate settings to achieve consistently accurate results. This was achieved by setting the Gradation Factor of the mesh to 0.2 and increasing the Default Number of Nodes on All External to increase the number of elements in the mesh. With each individual setting, the base model was analysed to output a SRF for the cliff. Convergence of SRF values was observed in models with 16500 elements or more, achieved with a 6-node triangle graded mesh, with a Gradation Factor of 0.2 and number of nodes on external set to 400 as observed in Figure 3-23 and Figure 3-24. This was therefore set as the minimum number of elements for all upcoming cliff models.

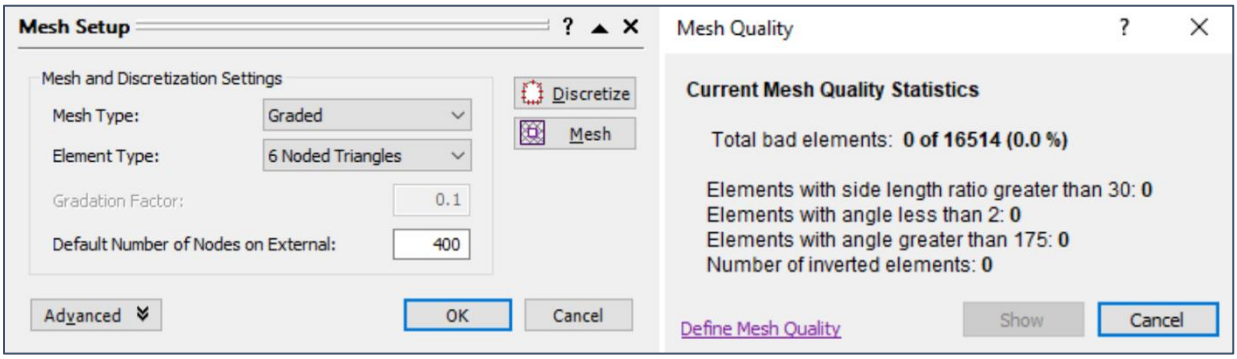

Figure 3-23: Base mesh setup and mesh quality

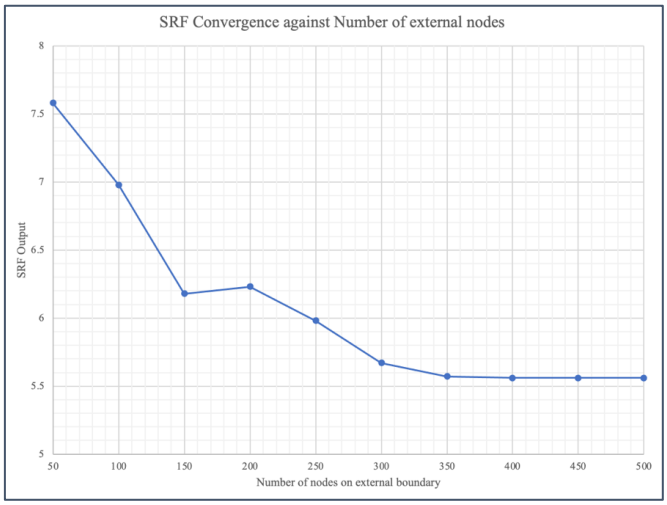

Figure 3-24: SRF convergence graph

Having set up the mesh, the slope stability analysis was then carried out, starting with the base cliff and parameters, then followed by a case study format by varying crevasse locations and depths along the ice surface. On the base shelf model, the model was computed using the Mohr Coulomb failure criterion and shear reduction factor (SRF). This was carried out to observe the type of failure experienced by the cliff, locations at which failure is initiated, and behaviour during failure, ultimately giving a SRF for the cliff which was interpreted as the factor of safety (FS).

Following the base scenario, two other scenario groups were analysed on the shelf. These were the variation of crevasse locations horizontally along the shelf keeping crack depth constant, and a vertical variation (VV) of crevasse depth at the critical horizontal location. The crevasses or cracks were introduced as excavations following the software capabilities. A constant crack width of 1m was assumed and used for all scenarios. The assumption was motivated by information about CAT Challenger tractors with continuous tracks, nearly tipping when the tracks ran into crevasses on the shelf. Together with the 1m width, a constant depth of 3m was used for all horizontal variation (HV) tests. This was motivated by an exploratory activity on the shelf where a 2m rod was lowered down into a crack and reported to be unable to reach the

bottom. The combination of the 1m width and 3m depth was therefore assumed to be a worst case scenario.

The HV was carried out at 1m increments from the shelf edge to 20m inland. These concentrated increments were selected within the range because the area closest to the cliff face were assumed to be the most susceptible to failure. Thereafter the increments were increased to 5m to 50m inland, and finally 10m increments to 90m inland due to a reduction in failure susceptibility. The VV models were finally carried out at the critical horizontal location with increments also set at 1m and increased till a depth of 20m below the surface. These methods have been illustrated in Figure 3-25 below.

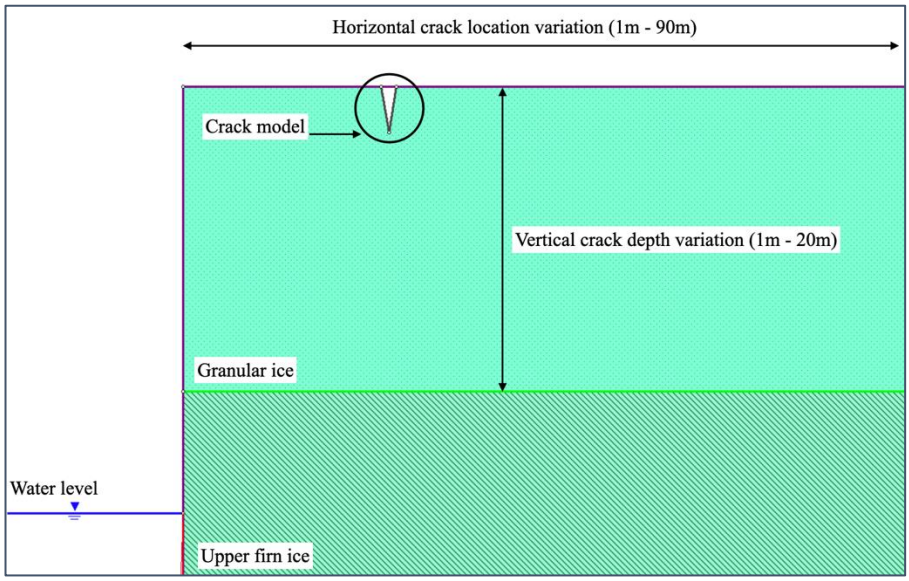

Figure 3-25: Crack scenario variations

3.12 Summary of chapter

From the field work carried out on the Fimbul ice shelf, 39 ice cores were retrieved to be used for material testing. On the cores obtained, characterisation was initially carried out to assess the quality and initial structure of the ice. During this, the grainsize types in the cores were characterised and ice lenses found. Following this, the RQD of each of the cores was calculated using the changes in grainsize and position of ice lenses as indicators of discontinuity.

The physical properties of the ice were then measured, starting with density. The mass/volume method was used for this measurement because it was found to be the second most accurate method of measuring density and most efficient in terms of sample preparation. The density was used to define the material unit weight and had applications in more properties. One of these properties was the elastic modulus of the material which was measured using non-destructive ultrasound methods. This was determined together with the material Poisson's ratio to define the material's deformation characteristics.

To obtain the material strength properties, the UCS test was carried out. This was done at a strain rate slow enough to allow the material to fail in a ductile manner to simulate slow creep failure expected on the ice shelf. The RMR method was then used to determine the shear strength of the material. It used RQD, UCS, and discontinuity spacing as the quantitative factors, and discontinuity condition and groundwater as the qualitative factors. With those, the RMR obtained was further used to select a range of cohesion and friction angle values, which when combined with the UCS of the material, gave the shear strength using the Mohr Coulomb failure criterion. The cohesion value obtained was also used as the tensile strength of the material because tensile failure is characterised to break the ice freeze bonds, which are interpreted as the material cohesion.

Using all the data obtained, a shelf cliff model was built. The model was drawn as a 90° vertical cliff with a total height of 100m and 28m above the water level. The material in the model was divided into 3 layers. The top layer was the granular ice layer with data from the tests carried out, bottom layer being the shelf firn ice with data obtained from deep shelf tests carried out in literature, and finally the middle layer which was labelled upper firn with data interpolated from the granular layer and lower firn layers. This interpolation was done due to the gradual increase in ice properties with increase in depth. The base model was run to obtain a base shear reduction factor, which was further interpreted as the cliff factor of safety. Following this, a case study was performed on the model by introducing a crack discontinuity on the model surface. Firstly, the crack distance from the shelf edge with a constant crack depth of 3m was varied. Second to this, the crack was then placed at the critical horizontal location and the crack depth varied vertically through the ice. This was aimed to provide a worst case scenario for crack location and crack depth on the shelf edge.

4 Results, Analysis and Discussions

In this Chapter, the results from the various methods adopted in this study were presented. For each of the results, an in-depth analysis was carried out and discussions made in each of the Sections. The Chapter begins with results and discussions from the core and site characterisation processes carried out. This is then followed by analysis of the physical and strength properties of the ice material. These properties were then summarised as software inputs in the cliff model inputs Section, which is then followed by base model and scenario model results and analysis. The Chapter is finally concluded by a summary where key aspects were presented.

4.1 Core and site characterisation

Cores obtained from the study area were the primary source of data for the research to take place. In this Section, the cores were first assessed to understand the ice structure in terms of grainsizes. This was detailed with regard to grainsize types, formations, densities, porosities, and their variation with depth. Ice lens then followed in the analysis process as they were presented in terms on ice lens concentrations and their implications to the study area. RQD percentages then followed and concluded this Section. All the data presented was discussed in terms of their cause, meanings to the scope of study, and application to further inputs.

4.1.1 Grainsizes

4.1.1.1 Grainsize types and formation

To begin the core characterisation, grainsizes of fine, medium, large were chosen following the method by MacDonell *et al.* (2021), all differentiated by the amount of light from a light box penetrating through the core section as seen in Figure 4-1 and Figure 4-2. Due to the limitations faced during preparation of granular thin sections in Figure 3-16, the lightbox method proved successful for use, despite its visual subjectivity.

Along the shallow depth of at which the cores were got, multiple combinations of the mentioned grainsizes were observed. On each core, the percentage of each grainsize observed was calculated using Equation 3-1. To aid this, colour grading on the log sheets was used. The medium grainsize was determined to be in most abundance on the shelf, occupying 62.4% of all the core length obtained. The fine grained followed with a percentage of 19.6% and the least present was the large grainsize with a total percentage of 17.9%. To further understand the different grainsizes, homogenous grainsize samples were also cut from cores and grainsize densities tested.

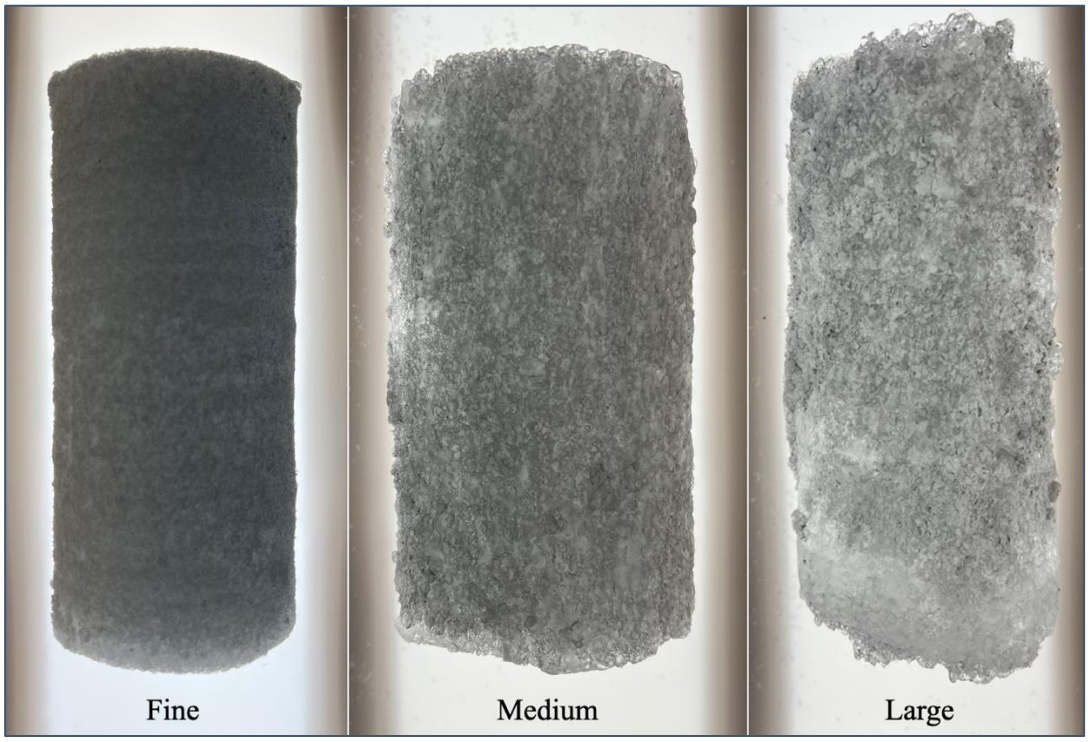

Figure 4-1: Grainsize measurement scale used

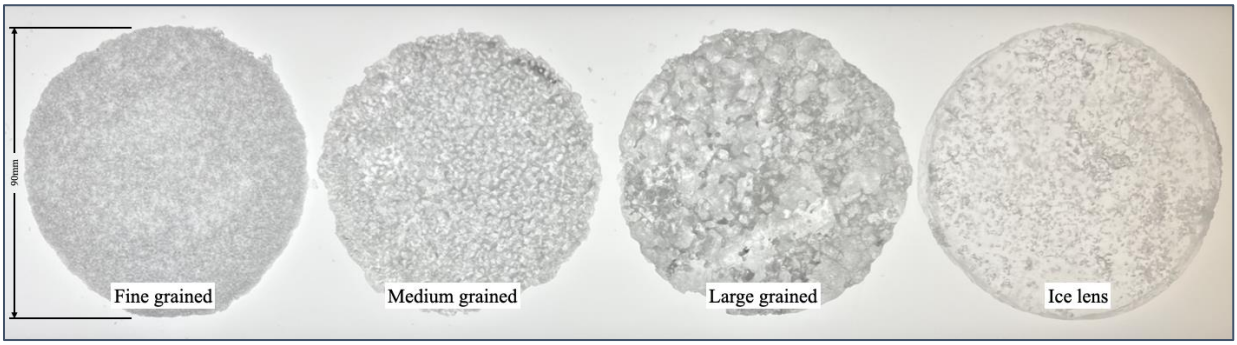

Figure 4-2: Grainsize variations and ice lens cross sections

The densities from fine, medium, and large grainsizes were found to be 473.2kg/m^3, 469.7kg/m^3, and 406.2kg/m^3 respectively. According to MacDonell *et al.* (2021), the increase in grainsize is attributed to increasing levels of metamorphism experienced on the ice shelf. Fine grained samples, closest to the makeup of snow, experienced the least amount of metamorphism, large-grained samples experienced the highest amount, and finally medium grained experienced a metamorphism level between the two extremities. Metamorphism in this case was understood to be influenced by both pressure and temperature on the ice shelf (Ligneau *et al.*, 2022). This process has been concisely described in Section 2.8, showing the similarities between ice and rock formations.

The formation process of the different grainsizes also showed a correlation to the quantity of each of the grains found on the shelf. The quantities were similar to the distribution viewed

by MacDonell *et al.* (2021) in the assessment of their 16 - 18m cores obtained. This could be attributed to the longer amount of time needed for metamorphism to take place from the medium to large-grained samples as opposed to the shorter time from fine to medium grained. The fine grains of ice melt and refreeze significantly faster when compared to the larger grains in the bigger sizes. However, as this is not fully understood, more research would need to be carried out to address this transition.

4.1.1.2 Grainsize, density and porosity

Density was first used to aid in the characterisation of the different grainsizes of ice in the study area. Each of the samples set aside for density tests were categorised into the mentioned grainsizes, with an addition of mixed samples which were a mixture of the grainsizes in samples used for compression testing. For each sample, the density was measured using the method in Chapter 3.7.1 and a porosity calculated using Equation 3-4. The values of density and porosity obtained can be viewed in Table 4-1 below.

Table 4-1: Grainsize density results

Grainsize	**Density (kg/m^3)**	**Porosity (%)**
Fine	473.2	48.6
Medium	469.7	49.0
Large	406.2	55.8
Ice lens	813.0	11.6
Mixed	564.1	38.7

An observation of the densities obtained revealed a trend between the densities and grainsizes. For each increase in grainsize, a drop in density was observed, which also led to an increase in porosity among the sizes. The trend was understood as an increase in particle compaction with a reduction in grainsizes. The finer sizes showed a higher level of compaction, with the fine particles filling potential air voids and reducing porosity. This compaction was also clearly viewed under a lightbox with fine samples having the least amount of light penetration among the sizes as seen in Figure 4-1. In contrast to this, the large-grained samples had the lowest density and highest porosity which was understood to be due to the least compaction of the particles among the grainsizes. When compared to fine grained samples, it was understood that due to the larger particle size, bonding between particles had the potential to leave air voids between the bonded particle matrices as illustrated in Figure 4-3. Finally, between the fine and large granular samples was the medium sized category with a density and porosity between the two extremities. This was understood to mainly be a more compacted bonded matrix than the large-grained category, but a less compacted matrix than the fine grained category.

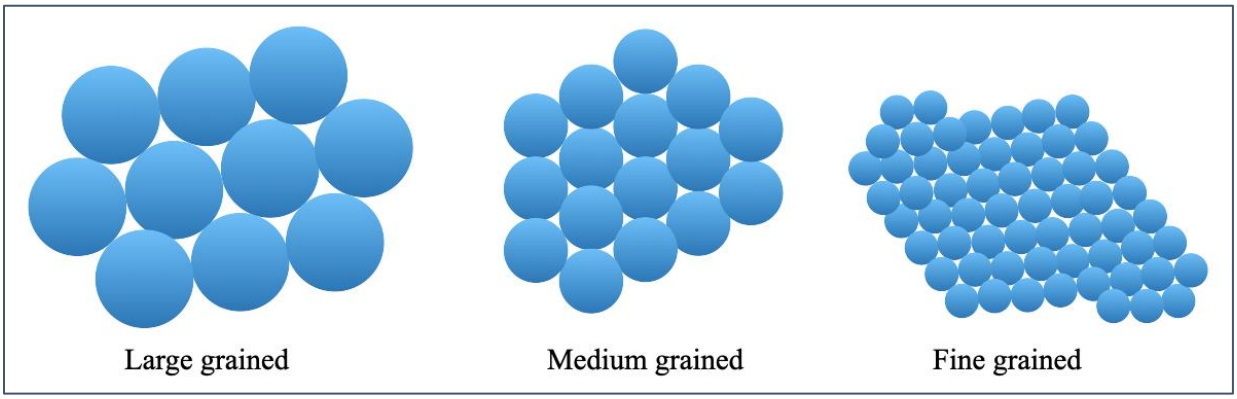

Figure 4-3: Ice particle density illustration

4.1.1.3 Grainsize variation with depth

The cores obtained did not exhibit any apparent organisation of grainsizes along the core depths, a phenomena also experienced by MacDonell *et al.* (2021). The large variation of arrangements was therefore assumed to be related to the variable weather events such as heavy rainfall, high wind speeds, or high temperature days that occurred on the ice shelf at different times. In addition to pressure and temperature, the existence of water from precipitation or melting also has an influence on the metamorphism on the ice shelf. This was therefore assumed to be a factor in the metamorphism of the grainsizes on the Fimbul ice shelf, and an influence on the large variation of grainsize positions with depth.

4.1.2 Ice lenses

4.1.2.1 Structure and concentrations

In addition to the grainsizes and their distributions on the shelf, ice lens percentages were also calculated due to their contribution to the overall structure of the ice material. The ice lens percentages of each core were calculated using the ratio of ice lens length in the core to the total core length. The lens percentages on all 1m cores ranged from 0% to 33.6% of entire core lengths. In addition to the clearly visible ice lenses, seen by the bright bands of light on the lightbox, different types or compositions of ice lenses were also obtained. When cross-sectionally cut, these were seen to be due to the concentration of granular ice and air bubbles trapped within the ice lenses.

Ice lenses were formed through crystallisation of water on the shelf. This crystallisation was mentioned to be due to the freezing of rainwater or recrystallisation of meltwater in the ice shelf. This process was mentioned to be both regular and irregular, with regular formation leading in the formation of clear ice lenses and irregular forming ice lenses with multiple discontinuities within them (MacDonell *et al.*, 2021). This process therefore explained the formation of the various ice lens types shown in Figure 4-4 that were observed in the cores.

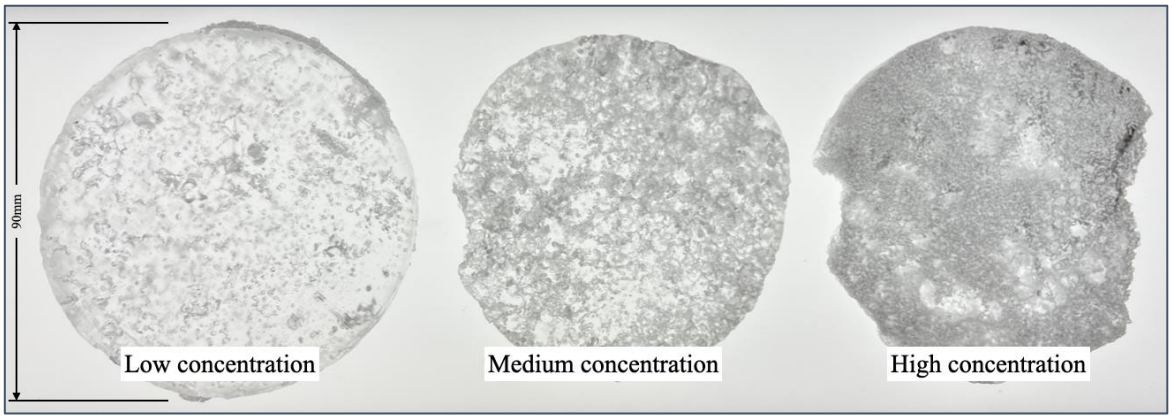

Figure 4-4: Varying air/granular concentrations in ice lenses

For ice lenses in individual cores, there was no clear correlation between ice lens depths and crystal sizes on cores. The ice lens crystals viewed using cross-polarised showed a wide variety of crystal sizes at different depths and positions on the ice shelf. This therefore showed no relationship between ice lens positions and depths. However, when cores of close proximity were placed side by side, a layer of ice lens could be viewed horizontally on the shelf. This led to the conclusion that the ice lenses were all individually formed in horizontal layers on the ice shelf, but under different circumstances, positions, and conditions leading to the large differences in crystal sizes and orientations as shown in Figure 4-5. Examples of these conditions were high melt water days, rainy days, or firn saturation in firn aquifers to mention but a few.

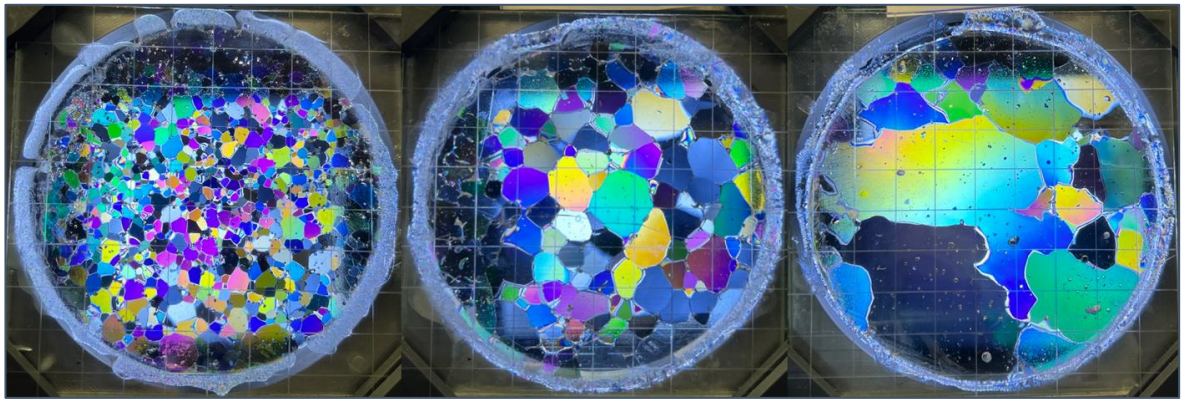

Figure 4-5: Varying crystal sizes within 1m layer

The ice lens density was then determined to be 813.0 kg/m^3. Despite being recrystallised water on the shelf, the value was different from the density of pure ice which was 920kg/m^3 used by authors like White & McCallum (2018) and Bassis & Walker (2012). This value was explained and understood to be due to the presence of air or granular ice that were trapped in the ice during the recrystallisation process (MacDonell *et al.*, 2021), evidenced by a value of porosity of 11.6% calculated and shown in Figure 4-6.

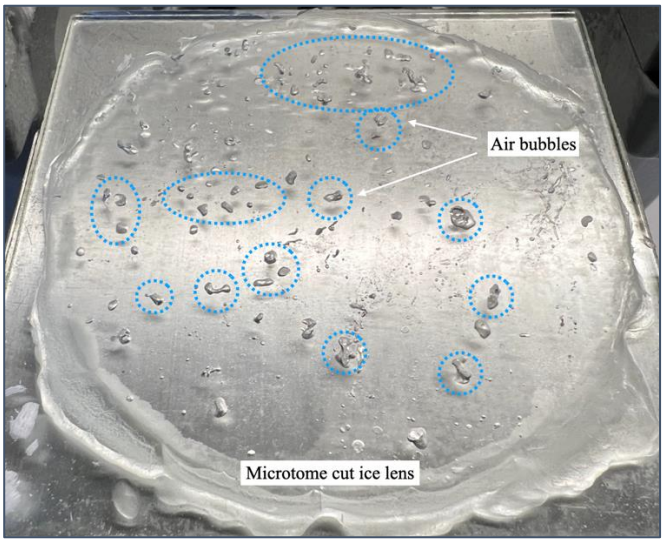

Figure 4-6: Air bubbles affecting ice lens density

4.1.2.2 Ice lens effects on study area

Using all the different ice lens types, the concentration of ice lenses across the entire shelf was visualised based on the individual core locations and their percentages of ice lens as plotted in Figure 4-7. This variation showed areas on the study site with higher concentrations of ice lenses.

The positions of ice lens concentrations showed critical meltwater areas on the shelf and the potential positions of firn aquifers capable of holding meltwater (Alley *et al.*, 2018). These further induced safety concerns on the ice shelf surface due to the fact that meltwater presence on ice shelves is a factor that causes hydrofracturing, leading to creation and deepening of crevasses and further increase of shelf edge instability. This therefore showed high risk areas on the shelf study area where the highest concentrations of ice lenses were illustrated. In addition to the ice lenses found in the cores obtained, a study of Müller Ice Shelf by MacDonell *et al.* (2021), with similar characteristics to those investigated in this study, found ice lenses as deep as 18m from the shelf surface. This therefore increases the concerns of safety on the ice shelf with possibilities of hydrofracturing and crevasses formation occurring at such depths.

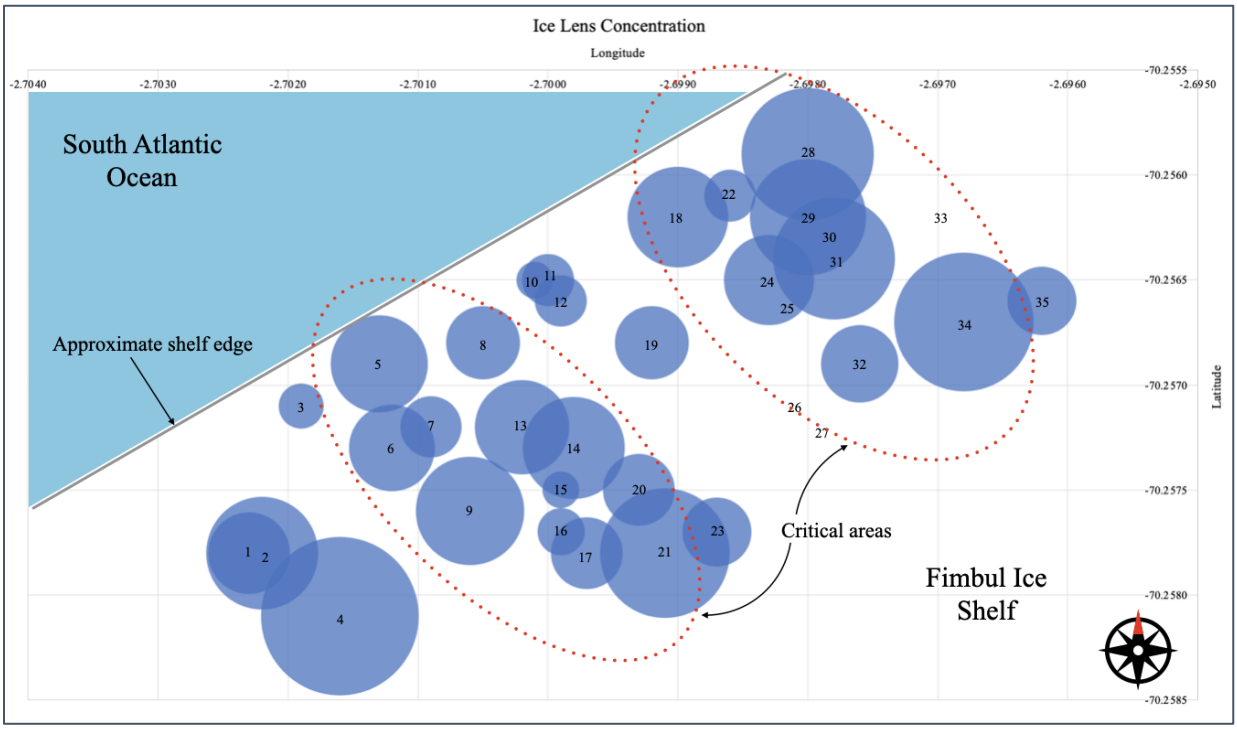

Figure 4-7: Ice lens concentrations showing critical melt areas

4.1.3 RQD

The values of RQD obtained from the cores ranged from 43% to 100% for all 35 cores used. However, one single value of RQD was required for use in the RMR classification to classify the material as a whole. To obtain this, a statistical approach was implemented to obtain an average RQD of 76% with a standard deviation of 14.5% using the graph in Figure 4-8. The random errors calculated for each RQD measurement were assumed to be incorporated into the standard deviation, leading to a material value of 76±14.5%. This value was therefore used in the determination of strength parameters in the RMR Section later in this Chapter.

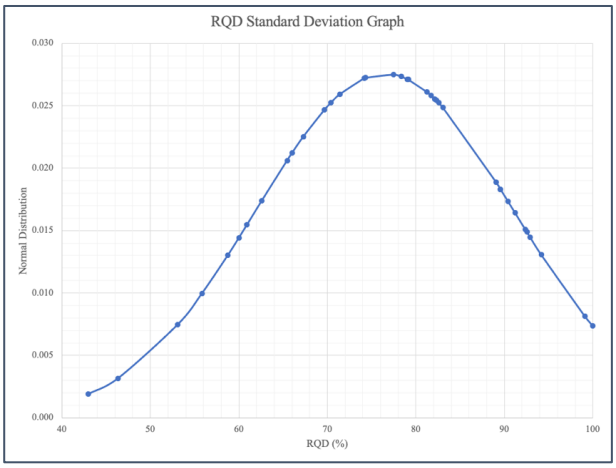

Figure 4-8: RQD standard deviation graph

The RQD of the cores on the shelf was taken as a direct quantitative assessment of the quality of the cores. In addition to the core quality, the values were also taken as a degree of jointing (Lucian & Wangwe, 2013) found on the ice shelf. Because the granular ice on the shelf was aimed to be modelled as a homogenous material, the RQD parameter played the role of quantitatively installing the influence of joints or discontinuities in the material being modelled. This was due to the fact that modelling ice with all the discontinuity components would be a cumbersome challenge with regard to not only time, but also data acquisition and computational power. These challenges were also highlighted by authors such as Crawford *et al.* (2021) and Bassis & Walker (2012).

The average value of 76% was assessed as a good degree of jointing in terms of the RMR classification (Bieniawski, 1979). This therefore meant that the existence of grainsize boundaries and ice lenses reduced the RMR rating from a value of 20 to 17, as seen in Table 3-4, therefore reducing the shear strength properties of the homogenous ice material to be used in the model.

4.2 Physical property results

This Section details the results obtained and analysis carried out for the physical properties required in the study. These were density, Young's/elastic modulus (E), and Poisson's ratio (v). The properties are discussed in the order of density, E, and finally v, while also detailing the result relationships to published sources and applications to further areas of the study.

4.2.1 Material density

Density of ice was classified as the most critical property to test as it was to be used to determine a variety of other parameters for the material. These included unit weight, elastic modulus, Poisson's ratio, and porosity.

A representative density of the granular material was determined. This value was to be used as a material input parameter to the granular material in the cliff model built in Section 3.9. To obtain the parameter, an average value of the densities was calculated. The average density calculated was 569.9 kg/m^3, with a standard deviation of 157.5kg/m^3, plotted in Figure 4-9, giving a unit weight of 5.59kN/m^3. The 569.9±157.5kg/m^3 value was assumed to encompass all individual random error uncertainty readings from the equipment used. The value of density was then used in further applications like the determination of elastic modulus and Poisson's ratio.

The granular ice density of 569.9kg/m^3 obtained was an encompassing value to represent the entire granular shelf material of the cliff model. The value obtained is within the bounds of values of granular ice obtained by other authors in literature. These include MacDonell *et al.* (2021) who had an average density of about 550kg/m^3 for their granular ice cores, Wang, E. *et al.* (2021) who obtained a 600 kg/m^3 density of well compacted snow, and Ligneau *et al.* (2022) who used a value of 500kg/m^3 to model the granular snow structure in avalanches. With the cores

obtained existing within 2m of the top of the study area, the density obtained lies in agreement with published sources. This was therefore used in the material model and sample specific determination of deformation properties in the next Section.

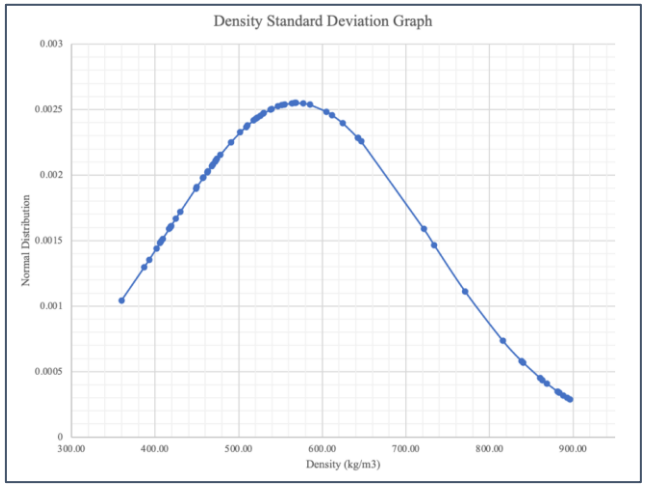

Figure 4-9: Density standard deviation graph

4.2.2 Elastic modulus and Poisson's ratio

The elastic modulus and Poisson's ratio were essential parameters to be used to model behaviour of granular ice on the ice shelf. To obtain the parameters, an acoustic method using pressure and shear wave velocities, as demonstrated in Figure 4-10, was used.

The pressure (V_p) and shear wave (V_s) velocities, required to calculate the E and v properties, were read off of the ultrasound measurement device. Values of V_p ranged between 3354m/s and 1852m/s while values of V_s ranged between 1640m/s and 712m/s. The pressure wave moduli (M) therefore ranged between values of 7.33GPa and 1.33GPa while shear wave moduli (G) ranged between 1.47GPa to 0.21GPa, with all moduli directly dependent on the densities of samples measured. These were therefore used to calculate the Poisson's ratios of each sample, giving ranges from 0.44 to 0.22 across the range of samples. The mean of all values was calculated to give a Poisson's ratio of 0.37 with a standard deviation of 0.06. After that, the elastic modulus of each sample was also calculated to give values ranging from 3.19GPa to 0.61GPa. For a representative material parameter, the mean was also calculated to give a value of 1.66GPa with a standard deviation of 0.87GPa, with the standard deviation graphs plotted in Figure 4-11 and Figure 4-12. The values of 1.66±0.87GPa and 0.37±0.06 were lastly assumed to encompass all random and systematic errors experienced by the individual E and v measurements.

Figure 4-10: Example V_p and V_s result readings

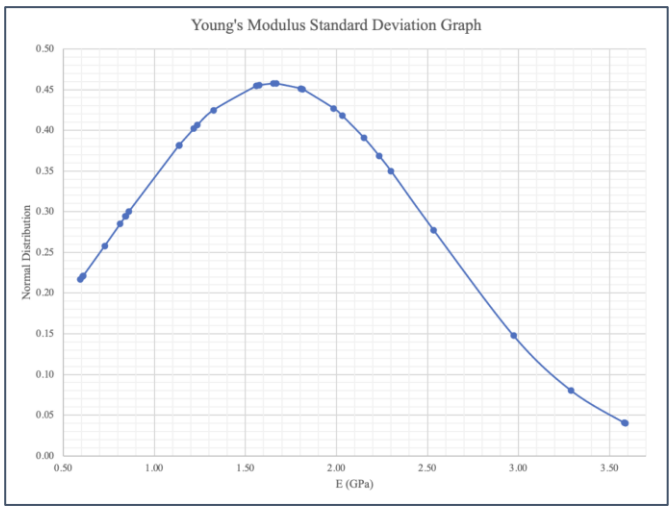

Figure 4-11: Elastic modulus standard deviation graph

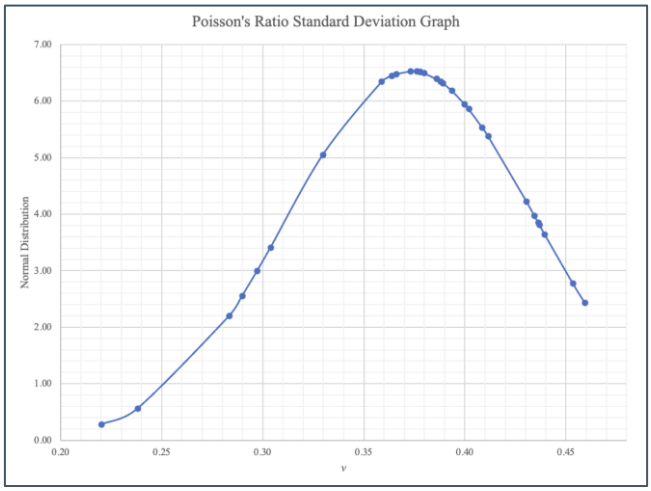

Figure 4-12: Poisson's ratio standard deviation graph

The elastic modulus and Poisson's ratio calculated for the material provided behavioural characteristics for the material. In terms of the *E*, the value of 1.66GPa showed a high amount of strain experienced by the material when loaded under a stress. The high strain, obtained by a high change in length in relation to the original length, was caused by the presence of air voids in the material tested. This can be explained by the change in height and volume of the material during stress application as material particles were compressed into the voids previously occupied by air. This is an action commonly observed in the densification of soil samples during a compaction test in geotechnical engineering where air voids are expelled from the sample to obtain the maximum dry density.

The *E* value was then compared to values obtained by other authors in published literature to gauge the material standing or similarities to others tested. Considering that there was a miniscule amount of authors who carried out tests on top level shelf ice, there was not much to compare the values obtained directly to. However, various authors carried out acoustic and statistical *E* analysis on different ice types showing a range of modulus readings. Rist *et al.* (2002), Yasui *et al.* (2017), and Petrovic (2003) each carried out tests on columnar crystalline ice to give *E* values of 8.2GPa, 8.7GPa and 9.7 - 11.2GPa respectively. On the other side of the spectrum, Serré (2011) obtained *E* values of 0.7 - 1.14MPa for rubble ice while Ligneau *et al.* (2022) used an *E* value of 1MPa for snow. Between these 2 extremities were Sinha (1989) and Cole (2001) who obtained *E* values of 7.5GPa and 5.5 - 7.5GPa for granular ice. Considering the 1.66GPa average *E* value obtained was for ice samples at the top of the ice shelf within 2m depths, it was concluded that the shallow depth of the material made it less stiff than the older and more fully crystallised ice at deeper depths, but a lot stiffer than snow at the surface of the shelf due to the higher amount of bonding time within the 2m depth of granular ice.

Poisson ratio values are viewed to primarily lie between 0.0 and 0.5, with materials like rubber having a value of close to 0.5 and stiffer materials like diamond around 0.18. The value of 0.37±0.06 therefore showed a higher amount of width change to a change in length of ice when loaded. This behaviour was evidenced by the ice bulging outwards and spalling viewed during uniaxial compression tests, similar to that experienced by Schulson (2001). Authors obtaining physical values of ice show an array of results for their particular ice types. Sinha (1989) and Petrovic (2003), each testing crystalline ice samples, obtained *v* values of 0.31 and 0.29 - 0.32 respectively. Considering the lower air voids in the samples used by the authors mentioned, a value of 0.37 for the top granular ice on the Fimbul ice shelf was concluded to be satisfactory, also because of the similarity in behaviour the material has when compared to those in other published sources.

4.3 Strength properties

The strength properties discussed in this Section were the UCS, shear strength, and tensile strength. The results obtained from the RMR used to determine shear strength were also detailed. This Section also provided in-depth interpretations and analysis to the values obtained and

showed their comparison with reference to what has already been achieved in published literature.

4.3.1 Uniaxial compressive strengths

The UCS tests of ice do not currently follow a documented standard, making determination of the UCS rather specific per study. Geotechnical engineering methods of uniaxial compression were therefore used to determine the UCS of the ice samples obtained. Since UCS tests were to be done on samples with a height twice the diameter, tests were mainly carried out on mixed samples. This was chosen due to the unavailability of homogenous samples with the required height and the density of the mixed samples. The mixed samples, comprising of different grainsizes and ice lenses, had an average density of 564.1kg/m^3, similar to the average density of all material of 569.92±157.46kg/m^3. This further justified the use of the mixed samples as true representations of the shelf ice.

Using the PLT-2W compression machine, failure loads of different ice samples were obtained. The machine, coupled with a mobile phone app, displayed test information as shown in Figure 4-13. Due to modifications of the test machine height, only failure load and time taken values were used, with the changes in height measured directly from the testing machine using vernier callipers. The failure loads ranged from 2.2kN to a value of 8.28kN across the spectrum of samples tested. Each of the ice materials failed in a ductile manner, with minute changes to original height of the sample. Spalling was also observed on a number of samples as small pieces of granular ice were detached from the sample during the loading processes.

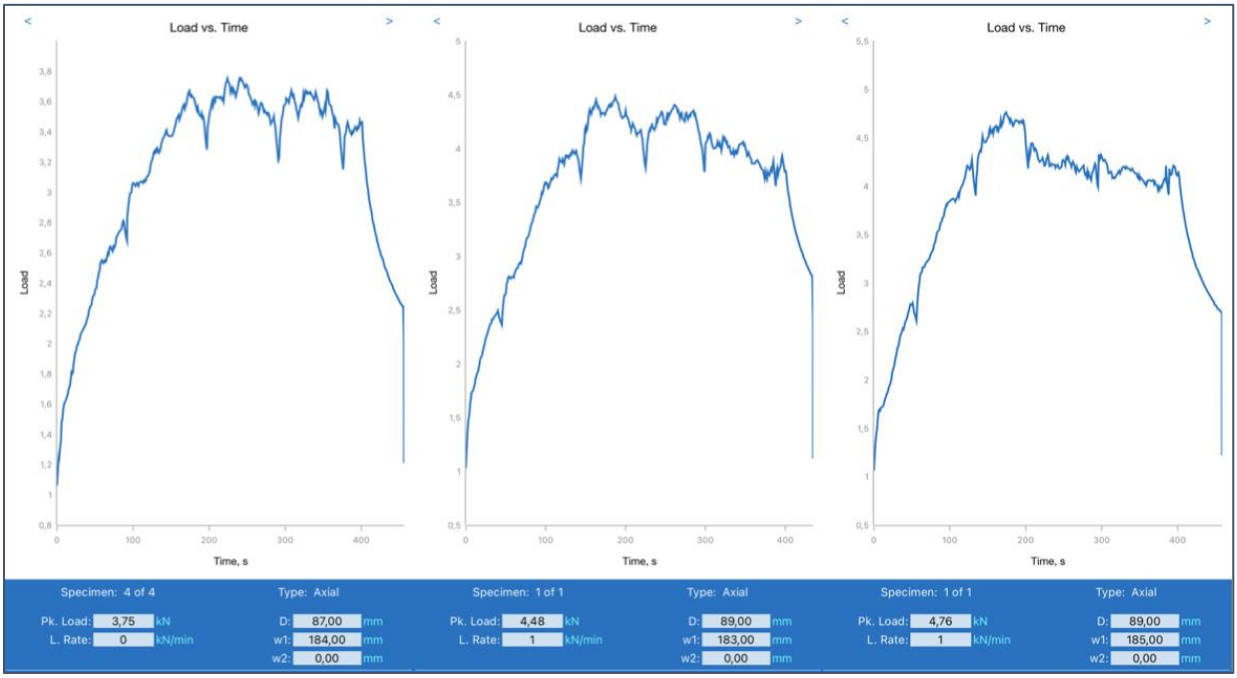

Figure 4-13: Example Load vs Time UCS test graphs

To then determine the UCS of each sample, the failure loads were divided by cross-sectional area to give stress values which ranged from 0.37MPa to 1.33MPa respectively. To obtain a representative value of the material, the values were statistically analysed using standard deviation and normal distributions. The mean obtained was 0.9MPa with a standard deviation of 0.27MPa as plotted in Figure 4-14. The 0.9±0.27MPa value was lastly assumed to encompass all random and systematic errors experienced by the individual UCS measurements.

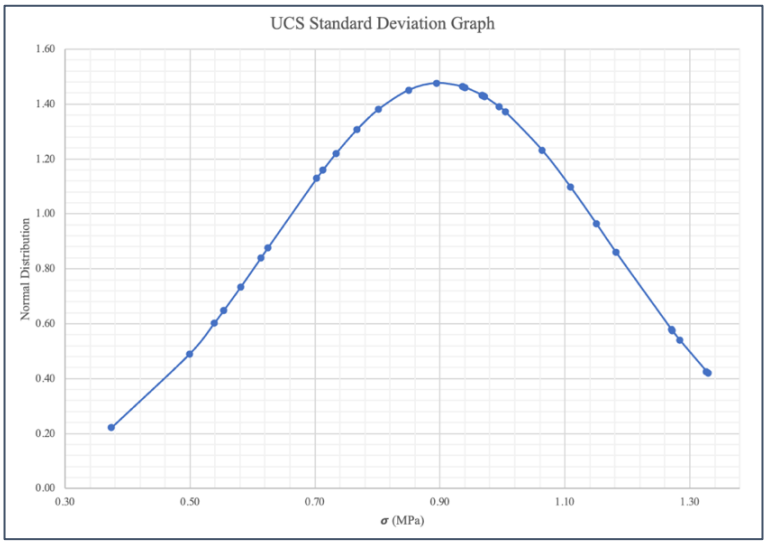

Figure 4-14: Standard deviation of UCS values

Axial compression was achieved using a pressure pump on the compression machine used. Reapplication of a load after one full movement of the lever arm induced high forces in the samples which was attributed to strain hardening. This led to the extreme dips and peaks on the load time graphs. Despite this, reapplication was carried out as smoothly as possible to reduce these effects and measure an accurate failure load.

Together with the strength, direct measurement of displacement and time was used to determine the strain experienced by the samples. Each sample had an initial height value, final height value, and time taken measurement taken. These were used to calculate the strain rate for each of the tests using Equation 3-12 and Equation 3-13. The strain rate measurements ranged between a maximum of $10^{-3.8}s^{-1}$ and a minimum of $10^{-4.7}s^{-1}$. The mean strain rate for all the tests was therefore $10^{-4.3}s^{-1}$ which lay in the ductile failure zone. According to Yasui *et al.* (2017) and Shazly *et al.* (2009), this strain rate lay in the ductile strain rate zone that was mentioned to be less than $10^{-3}s^{-1}$. This type of failure was used to simulate a slow creep failure, which was to be essential to simulate the slow gradual failure of the granular ice in the ice shelf model.

Failure of the samples tested was viewed to occur in a ductile manner with visible axial deformation and negligible lateral deformation, evidenced by the spalling of grains from samples tested. During testing, microcracks were also heard in the sample, which was attributed to the failure of frozen bonds between granular particles. Despite the failure of such bonds, the

structural integrity of the samples was maintained which was attributed to sintering. Sintering was defined as the formation of ice bonds due to melting and refreezing (White & McCallum, 2018). This kind of failure was also attributed to the high porosity calculated in the granular ice samples as seen in Table 4-1. The voids in the ice that were previously filled with air allowed for movement of grains within the material lattice, explaining the higher axial and negligible lateral deformations observed.

The average UCS calculated was then compared to the ranges of ices strengths in published literature. Rist *et al.* (2002) and Petrovic (2003) obtained UCS values of crystalline ice as 4 - 30MPa and 5 - 25MPa respectively. Han *et al.* (2015) then obtained 3.9 - 5.1MPa for sea ice, Wang, Q. *et al.* (2018) got 2.2 - 2.9MPa for Arctic ice, and Wang, E. *et al.* (2021) got 1.2 - 1.7MPa for lab snow ice. The value range for ice obtained was 0.63 - 1.17MPa, which was similar in strength to the laboratory made snow ice in Wang, E. *et al.* (2021) but weaker than crystalline ice. This observation was justified due to the weaker bonds between individual granular ice particles when compared to the well bonded crystal lattice in crystalline ice.

The UCS in this study carried significance because it was to be used for the determination of the shear strength properties through RMR and the shear strength through the Mohr Coulomb shear strength equation in Equation 3-14. The values obtained were then carried forward for use in the determination of shear strength as described in the next section.

4.3.2 Rock mass rating

The rock mass rating was used in the determination of the ice strength properties due to ice's relationship to rock and the data available from field work during core retrieval. The parameters used for the RMR were UCS, RQD, discontinuity spacing, discontinuity conditions, groundwater, and discontinuity orientation. Each of the parameters mentioned provided an RMR value which was in turn used to get the properties for shear strength.

Beginning with UCS, the value obtained during the compression tests was 0.9±0.27MPa. The method tables by Bieniawski (1979) stated that materials with strength of 0.6MPa and below should be assessed as soil. As the value obtained existed closest to extremely weak rock with strengths between 1-2MPa, a rating of 0 was taken for the parameter. The rating can be found in Table 3-3. The RQD was then statistically determined to give a value of 76+14.5% for the material. Using the range of values in Table 3-4, a rating of 17 was given for the material. For the discontinuity spacing, a statistical analysis was also carried out for the discontinuities values obtained from each core. The smallest discontinuities were measured and recorded for each core to get an average value of 97mm for the entire granular material. This value lay within the range of 0.06 - 0.2m in Table 3-4 and gave an RMR rating of 8.

The remaining 3 parameters were assessed using core and site conditions. The discontinuity condition for the ice cores was selected as slickensided, giving an RMR rating of 10 from Table 3-6. The rating was chosen due to the smooth, rounded, and slippery nature of ice, and the presence of ice lenses within the granular ice cores that ranged in the 1-5mm range

mentioned. For ground water, the cores were rated as dry and given a rating of 15 as per Table 3-7. This was selected due to the absence of water on the ice shelf during the core drilling. The parameters mentioned therefore gave a summed up RMR_{basic} value of 50.

Finally, the discontinuity orientation value needed to complete the RMR rating was based on the dip measurements of discontinuity values on the shelf. Due to the vertical stacking of snow layers throughout the shelf, all layers of ice material and discontinuities were assumed to lie horizontally with a dip angle of 0º. This therefore gave a 'Very favourable' rating with a value of -0, which when summed to the RMR_{basic} rating to give a final RMR value of 50. This was tabulated into Table 4-2. When the upper limit and lower limits of each of the quantitative values were also assessed, the upper limit values summed up to an RMR of 50, while the lower limits summed up to a value of 47.

The RMR value of both 50 and 47 were then classified into Table 3-8. At the value of 50, the material fell into rock class III with a 'fair' classification. This then in turn led to the choice of cohesion and friction values of 0.20 - 0.30MPa and 25 - 35º respectively. The averages of each were calculated to 0.25MPa and 30º respectively.

Table 4-2: Rock Mass Rating parameters

Parameter	**Value**	**RMR rating**
UCS (MPa)	0.9±0.27	0
RQD (%)	76±14.5	17
Discontinuity spacing (mm)	97	8
Discontinuity condition	Slickensided	10
Groundwater	Dry	15
Discontinuity orientation (º)	0º	-0
Sum		**50**

In terms of cohesion, there were no cohesion parameters found for granular ice similar to that on the ice shelf. However, various authors obtained and used the cohesion for their specific ice models. These include Reiweger *et al.* (2015) who obtained a cohesion of 0.17kPa for weak snowpack, Podolskiy *et al.* (2015) who found 2.5kPa for avalanche snow, and Bassis & Walker (2012) who used a cohesion of 1MPa for glacier ice. Considering that the granular ice tested experienced higher metamorphism than snowpack, but less than glacier ice, it was assumed that the cohesion would lie between the 2.5kPa of snowpack and 1MPa of glacier ice. Despite the wide range, use of the value of 0.25MPa from RMR was justified, also due to the unavailability of more shear strength property data for similar granular ice.

In terms of the angle of friction, there was also a variety of values used for crystalline ice, but minimal for granular ice. Reiweger *et al.* (2015) mentioned a range of 12° - 28° for weak snow pack, Serré (2011) mentioned 30° - 45° for rubble ice, and Schulson (2001) mentioned 30° - 45° for crystalline ice. Like in cohesion above, the value of 30° got for the granular ice placed

it higher than the snowpack and at the lower end of the crystalline ice range. This position of shear strength parameters from the RMR was therefore justified, not only by the cohesion and angle of friction, but also the density values of the range of ice material variants.

4.3.3 Shear and Tensile strengths

The granular ice tested was taken as a Mohr Coulomb material with a failure based on shear strength properties. The choice for use of this criterion is backed as multiple literature sources for ice materials modelled. The RMR method output cohesion and friction angle values as 0.25MPa and 30º. These values, together with the UCS value of 0.9MPa, were used to determine the shear strength of the material. This was calculated using Equation 3-14. The shear strength of the granular ice was then calculated as 0.77MPa.

When compared to published literature, Masterson (2009), Rist *et al.* (2002), and Petrovic (2003) each had calculated shear strength values for crystalline ice at 0.86MPa, 1MPa and 1.5MPa respectively using an equation by Ligneau *et al.* (2022). As the shear strength obtained was less than those of crystalline ice, the result was considered acceptable. This is due to the understanding that the granular freeze bonds between particles were weaker than the fully bonded lattice in solid ice samples.

Following the method by Podolskiy *et al.* (2015), tensile strength of the ice was taken to be equal to the cohesion in the material. As the cohesion value from the RMR was 0.25MPa, the tensile strength of the material was also taken to be 0.25MPa. This value and associated parameters were then used as input parameters to obtain the ice shelf modelling results mentioned below.

4.4 Cliff model inputs

Results obtained from the FEM process were described in this Section. It begins by consolidating the physical and strength property results from earlier laboratory tests and literature sources which were used as input parameters for the model. The results from the base model scenario were then described, followed by the scenario case studies which involved the horizontal crack variation and vertical crack variation on the ice shelf. The results obtained from all the numerical modelling of the shelf study area were analysed and interpretations of the values discussed within the scope of this research.

As the software ran the SRF analysis, the model concluded failure when a model experienced destabilisation, which occurred when model mesh experienced excessively high deformations. Such high deformations are interpreted as acceleration and movement of the cliff material which symbolised failure. The SRF at the point of instability was therefore termed as the “failure SRF”. Using the tolerance of 0.01, the SRF which was 0.01 less than failure SRF

was then considered as the critical value and further termed as the “critical SRF” throughout the report.

Following the laboratory tests and literature sources explained in Section 3.10, the Table 4-3 below summarised the input parameters used for the FEM models throughout this section.

Table 4-3: Model material property inputs

Properties	**Granular ice**	**Upper firn ice**	**Lower firn ice**
Unit weight, γ (kg/m^3)	5.58	6.97	9.00
Porosity (%)	37	23	4
Young’s modulus, E (GPa)	1.66	6.00	9.00
Poisson’s ratio, ν	0.37	0.335	0.30
UCS (MPa)	0.9	8.5	16
Cohesion, c (MPa)	0.25	0.625	1.0
Angle of friction, ϕ (º)	30	33.5	37
Shear strength, τ (MPa)	0.77	6.22	13.1
Tensile strength, T (MPa)	0.25	0.625	1.0

4.5 Base model analysis

The base model was the initial model built comprising of the shelf study area, input parameters, and boundary conditions without any surface discontinuities. This model was the initial test to determine the functioning of the model in an ideal scenario. Determination of the stability was achieved by running the model using the software’s finite element method (FEM) analysis.

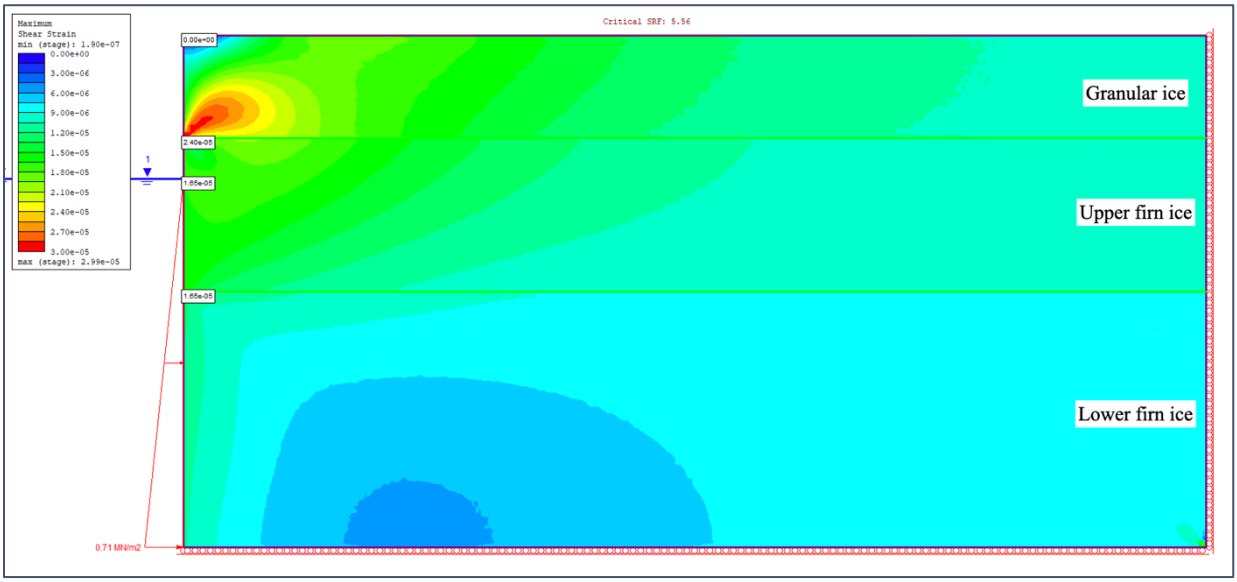

Figure 4-15: Shear strain contour model at Critical SRF

The software outputs of the base cliff scenario gave a critical SRF of 5.56. The base cliff model was observed to remain stable with no deformations within the lower SRF values, up until the critical SRF at 5.56. To understand the mechanism in the critical model, various contour figures output during the analysis were investigated. In terms of stresses, the top of the model was observed to exist in tension, with the value increasing with depth till the bottom of the cliff. The highest tensile stress experienced was 10kPa, denoted by -0.01MPa on the model, which increased to a 910kPa compression at the bottom of the model. The stress trajectories can also be seen in Figure 4-16 showing the resultant direction of the principle stresses inside the ice shelf model. The critical SRF model was observed to have a dominantly vertical principle stress orientation. The vertical stress trajectories showed resultant stress values dominated by σ_1 and compression in the *y*-axis. The maximum strain was then located at the material boundary between the granular ice and upper firn layers, with a magnitude of $2.40e^{-5}$ as seen in Figure 4-15.

The current ice shelf is a freestanding cliff with no failure recorded, showing a factor of safety greater than 1.0. With the critical FS from the analysis being 5.56, the base cliff edge can be considered safe with the 'failure resisting forces' greater than the 'failure driving forces' by a magnitude of 5.56. According to Equation 3-15, the strength parameters; cohesion and friction angle, of the ice at the critical SRF of 5.56 were calculated to be 45kPa and 5.40° respectively.

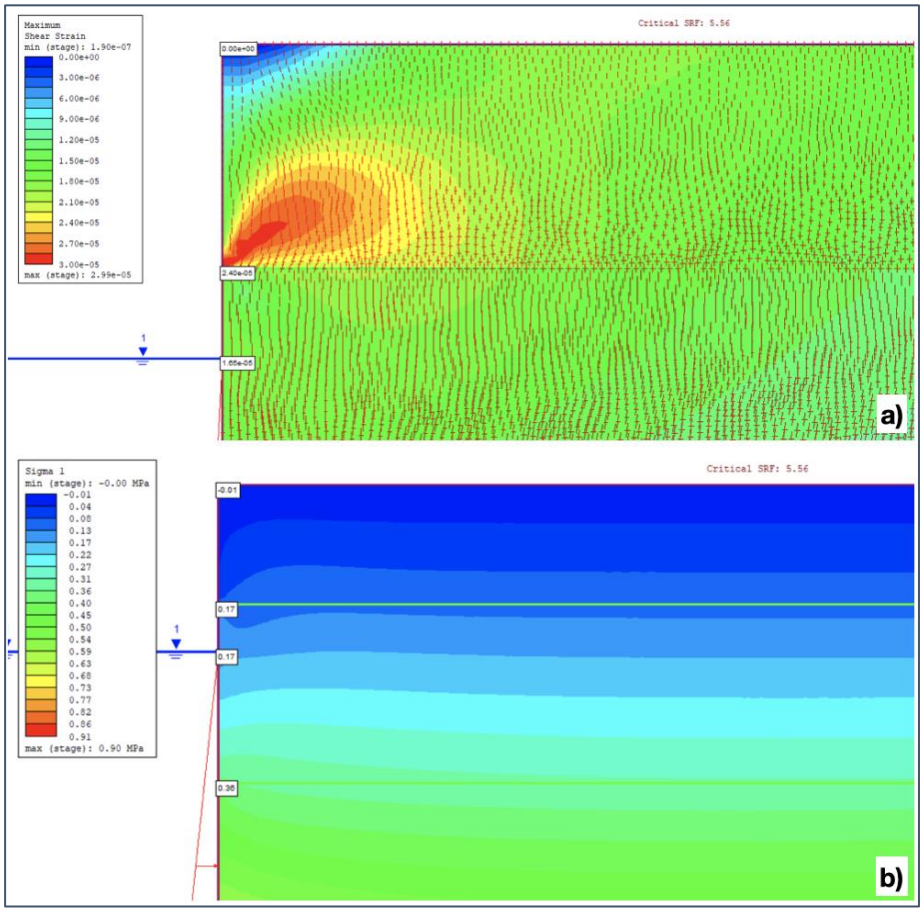

Figure 4-16: **a** Stress trajectories **b** σ_1 contour plot

As the critical SRF was found at 5.56, total failure of the cliff then occurred at a SRF of 5.57. The cliff was viewed to fail in shear, with the shear plain starting at about 60m inland, to a depth of about 40m from the top of the shelf. The shear failure involved horizontal movement of the cliff edge with a vertical drop of the maximum shelf height within the sheared zone. After failure, the stresses at the top of the shelf were viewed to no longer exist in tension, with the stress value increasing from -10kPa to 20kPa on the surface. However, the increase in stress with depth outside the shear zone remained unchanged. The failure SRF model was also observed to have a wide variety of the stress trajectories with the shear plane having predominantly horizontal principle stress trajectories. The resultant of the stresses was altered due to high shear stresses experienced along the shear plain, thus changing the direction of the resultant stresses to a horizontal angle as seen in Figure 4-16.

The maximum strain on the failure SRF was then experienced around the material boundary between the granular and upper firn ice with the boundary magnitude being $1.12e^{-02}$ and the maximum on the model being $1.50e^{-02}$ right above the boundary line. The strain distribution observed was in direct correlation to the displacement contours of the model. The failure shear strain and stress trajectories can be viewed in Figure 4-17. The failure parameters for the SRF of 5.57 were the calculated to give 45kPa and 5.39° for cohesion and friction angle respectively.

The failure patterns viewed on the failure model showed both shear and tensile failures occurring on the shelf edge. Tensile failure was primarily observed at the top of the shelf which is the driving force for development of crevasses. These developed crevasses have the potential to grow deeper through actions like crack propagation, hydrofracturing, shear property reductions, and as seen in the model, additional shear failure of the rest of the material. Multiple tensile failure locations on the top of the shelf signified the development of multiple tensile cracks which have the potential to develop into blocks and cause toppling failure of the shelf. In addition to this failure, there was a clearly defined plane of shear failure on the shelf edge. This was attributed to the geometry of the cliff and shear strength parameters input to the model. This was seen to be a catalyst for planar failure on the ice shelf.

A combination of the mentioned failure types led to bulging out of the material as seen in Figure 4-17, which could in turn fail in crumbling due to shear at the cantilever boundary induced. An example of this can be seen in Figure 4-18. The failure observed from the model was therefore interpreted to show a number of failure types, which was one of the difficulties noted by Bassis & Walker (2012) when modelling failure of ice. However, the failure types noted were planar, toppling, and crumbling based on the structure of the model used.

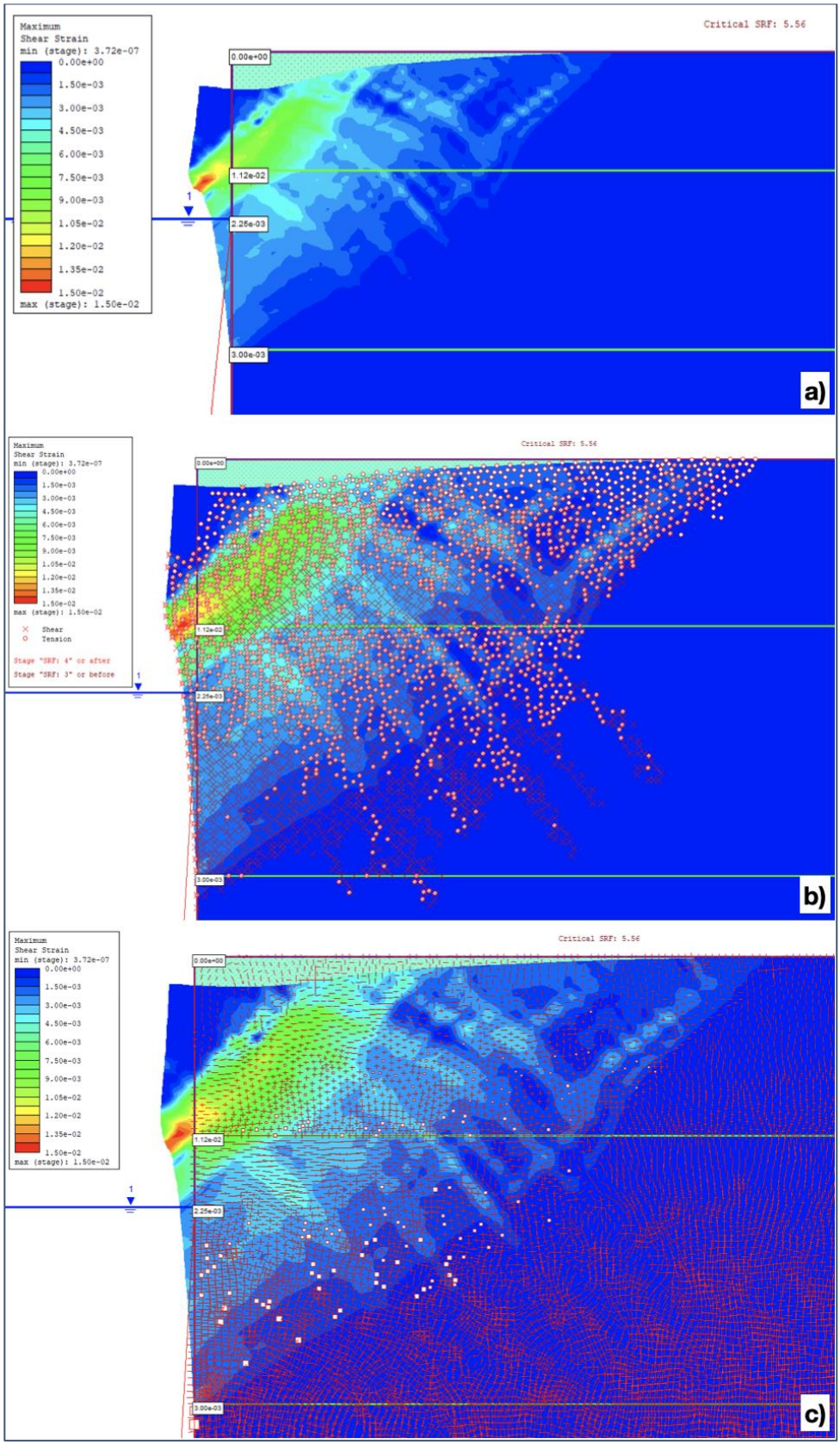

Figure 4-17: **a** Shear strain failure contour plot; **b** Shear & tensile failures; **c** Failure stress trajectories

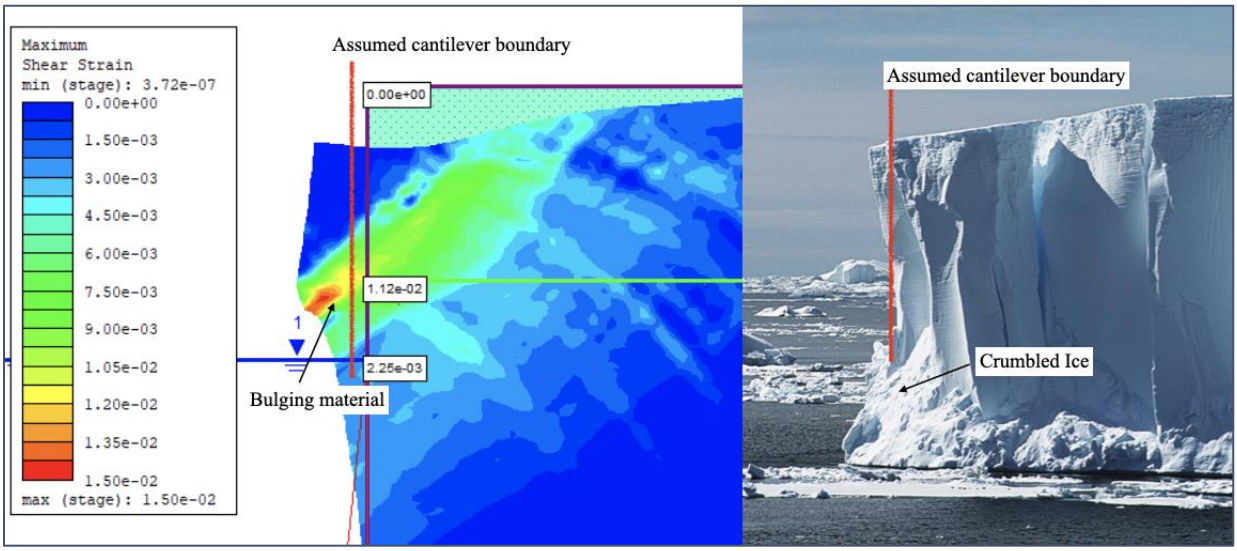

Figure 4-18: Assumed crumbling zone

A notable limit to the model was that majority of the failure was observed to occur in the top granular ice. This was determined to be due to the relatively lower strength of the top layer when compared to the denser and stronger lower layers of ice. With this, the maximum shear stress occurring close to the material boundary was assessed as a consequence of discontinuous change in properties from the top granular layer to the upper firn layer of the model. In addition to the discontinuity in physical properties, the high magnitude of displacement computed in that area played a role in the magnitude of shear strain experienced. The position of the material boundaries therefore had an impact on the failure observed. Despite the availability of literature supporting granular ice at the modelled depth, a deeper coring exercise would be required to obtain an in-depth analysis of the ice layers and their gradual change with depth.

Despite majority of the failure viewed in the granular material section, the model showed development of tensile failure in the lower stiffer upper firn material as well. The angle at which the shear occurred was seen to load the lower material to a position where tensile forces were experienced. This was interpreted as a further widening of cracks below the granular ice after failure had occurred. This increased the shear strain experienced by the material and increased the likelihood of toppling failure through crack deepening and widening. However, it was noted that due to the low deviatoric stresses experienced in the ice shelf, the crack and crevasse propagation would stop at a depth where the stress concentrations at the crack tip are less than the glaciostatic stresses in the shelf (Rist *et al.*, 2002). These stresses would prevent the fracture toughness of the ice to be reached.

The base scenario was not an actual representative of the shear because the shelf currently has cracks on the surface as seen in Figure 1-2. The following Sections therefore provide an analysis of the results of more representative shelf scenarios with crack discontinuities added.

4.6 Scenario analysis

To determine the effects of cracks or crevasses on the shelf, two case scenarios were chosen. They included a horizontal variation of crack location keeping the crack depth constant and a vertical variation of crack depth keeping the horizontal position constant. The crack scenarios were analysed to determine the critical combinations of crack location and depth on the shelf under the limits of data used for the models.

4.6.1 Horizontal variation

For this scenario, a 1m wide crack with a 3m depth was modelled. For each of the distances away from the shelf edge, a SRF equating to a FS was obtained. Using the values, a graph of FS against horizontal distance from shelf edge was plotted, with the output in Figure 4-19. The results from the graph show a critical horizontal depth at 13m from the edge of the cliff. This critical distance had a FS of 4.24 and was the lowest along the shelf surface.

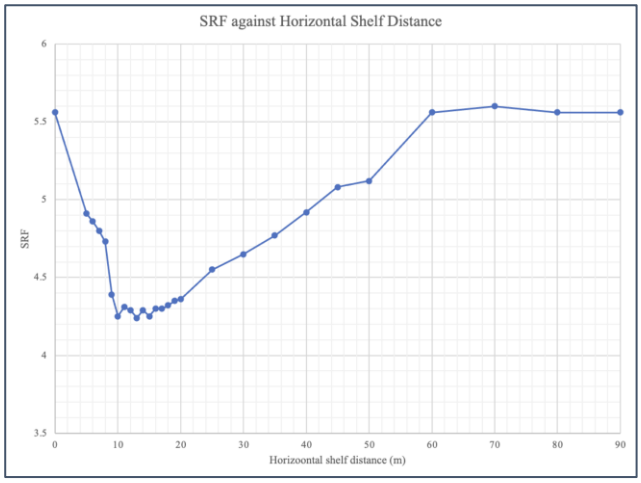

Figure 4-19: SRF against horizontal crack distance graph

The variation between SRF and horizontal distance plotted showed the existence of 4 crack location trends. These location trends have been termed as regimes to collectively describe the models that were ran. In the first regime, between 0m and 8m from the shelf edge, the cracks were observed to have an increasing effect on cliff instability. This was eluded to by the reduction of SRF the further inland the crack was. This was explained by the increased influence the crack had on the cliff shear plane through the nullification of tensile strength within the crack. Following that, the cracks between 9m and 20m were viewed to exist within the shear plane and greatly reduce the stability of the shelf. Their presence reduced the cohesion and hence shear strength in the top section of the model, further reducing the SRF required for failure. It is within this regime that the critical SRF was determined at 13m shown in Figure 4-20. The critical shear failure parameters at that SRF were a cohesion of 59kPa and angle of friction of 7.075° following

Equation 3-15. The next regime was between 25m and 50m. As the crack distance from the shear plane continuously increased, the SRF value computed increased as well. This finally led to the fourth regime, between 60m and 90m, where the SRF of the models were relatively equal to the SRF of the base cliff model without cracks. This therefore showed the distance where cracks had no effect on the overall stability of the shelf edge shear failure.

A detailed analysis of the critical horizontal distance at 13m was then carried out to understand the model results. Firstly, the stress contours of the model were assessed to determine the magnitudes of stresses within the shelf model. The top of the ice shelf was observed to exist in tension with a magnitude of 10kPa, shown by -0.01MPa on the model. The stresses at the bottom of the crack were also observed to be in tension with an equal magnitude of 10kPa. The tension of 10kPa caused full yielding of the ice at the bottom of the crack, with the yield contour showing 100% at the crack tip which dropped to 20% yield at about 11m below the bottom of the crack as observed in Figure 4-21. The crack tip also experienced the maximum shear strain on the critical SRF model with a magnitude of $1.10e^{-03}$. This was also evidenced by the displacement vectors showing widening of the crack with magnitudes of $3.15e^{-0.4}$m and $1.05e^{-04}$m on the right and left crack faces respectively as observed in Figure 4-22.

At the critical SRF, tensile failure was observed at the bottom of the crack before development of the shear plane failure of the entire shelf. This was understood to be due to stress concentrations at the tip of the crack leading to further crack initiation and propagation. The stress concentrations at the crack tip led to an increase in the stress intensity at the bottom of the crack. When the stress intensity increased to a value equal to the fracture toughness of ice, crack nucleation and propagation occurred. However, due to the Mohr Coulomb criterion used, this was shown by the yielded zone under the crack tip. It was also aggravated by the tension experienced by the shelf surface due to moment caused by water pressure on the deeper sections of the shelf. In addition to the tensile failure at the crack bottom, the maximum shear strain of the critical model was also located at the bottom of the crack. This was due to the tensile stresses and high amount of deformation experienced at the crack bottom.

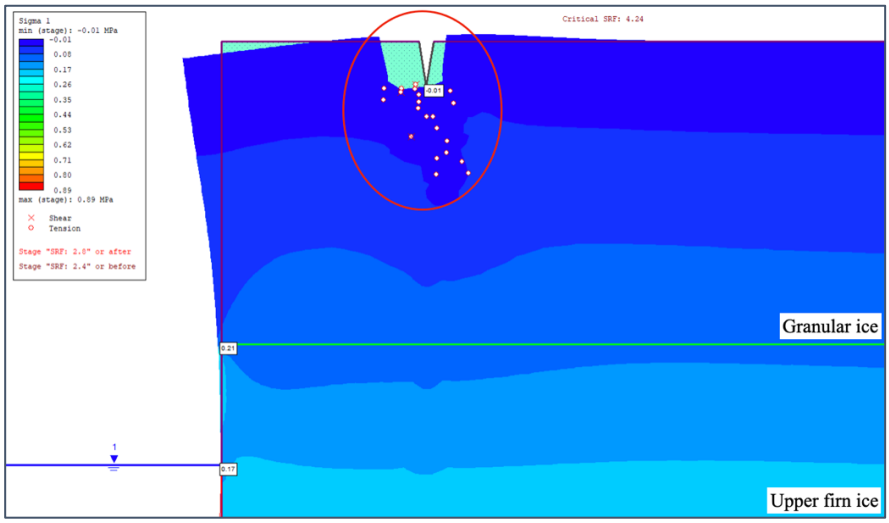

Figure 4-20: Critical HV SRF stress contour showing crack failure

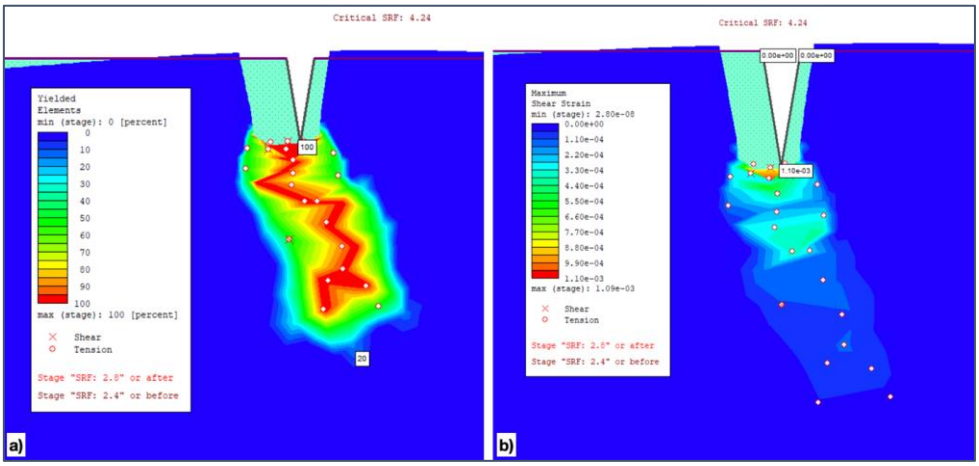

Figure 4-21: **a** Critical HV yield contours; **b** Critical HV shear strain contour

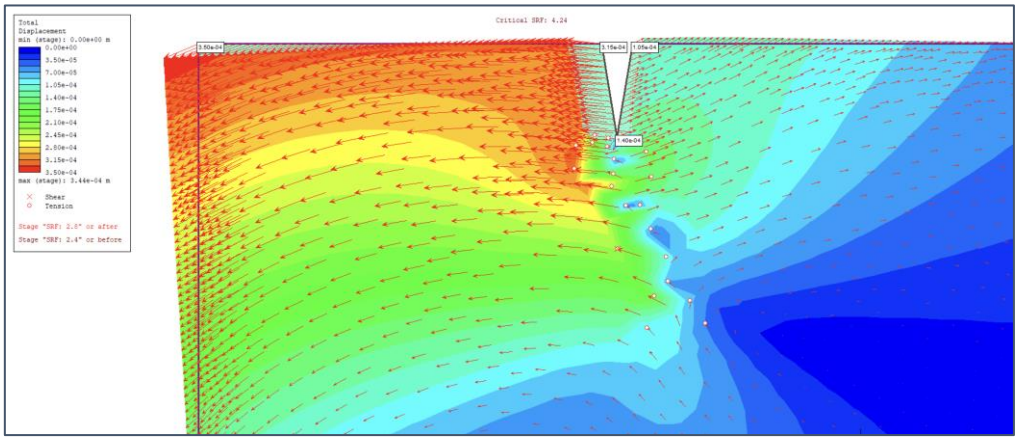

Figure 4-22: Critical HV displacement vectors

With critical SRF being 4.24, the failure SRF was found at a value of 4.25. The failure observed was a full shear failure of the cliff edge with the development of an angled shear plane. The shear plane and shear failure led to further widening of the crack by about 0.06m and more tensile failure at the crack bottom as depicted in Figure 4-23. The entire shear zone was also observed to have yielded to a 100% contour, with failure in the yielded zone occurring in both shear and tension marked on the model in Figure 4-23. According to Equation 4-1, the maximum shear stress experienced in the failure region was calculated to be 0.125MPa, from the maximum deviatoric stresses in the region which was 0.25MPa.

$$\tau = \frac{(\sigma_1 - \sigma_3)}{2} \qquad \text{Equation 4-1}$$

where τ = shear stress,

σ_1 = major principle stress, and

σ_3 = minor principle stress.

In addition to the stresses, the maximum shear strains were observed just above the material boundary between the granular and upper firn ice. The shear strain at the boundary was observed to be $1.14e^{-02}$ and the maximum experienced in the entire model observed to be $1.82e^{-02}$. The shear strains viewed were further correlated to the displacement vectors showing a high shear strain at areas of high deformation in Figure 4-24. The highest deformation was however observed at the top of cliff edge with a magnitude of $7.02e^{-02}$.

For the failure model at a SRF of 4.25, the shear strength parameters; *c* and phi, due to the strength reduction were 59kPa and 7.059° respectively. The failure model was observed to primarily fail due to the formation of a shear plane with a decrease of the mentioned strength parameters. In addition to the shear failure, tension failure was also experienced throughout the model in areas where the tensile stress exceeds the tensile strength of the ice. As the tensile strength of ice was entire based on the cohesion, which was defined as the ice bond strength by Kulyakhtin & Høyland (2014), the tensile failure occurred when freeze bonds in the ice were broken by the build-up of tension.

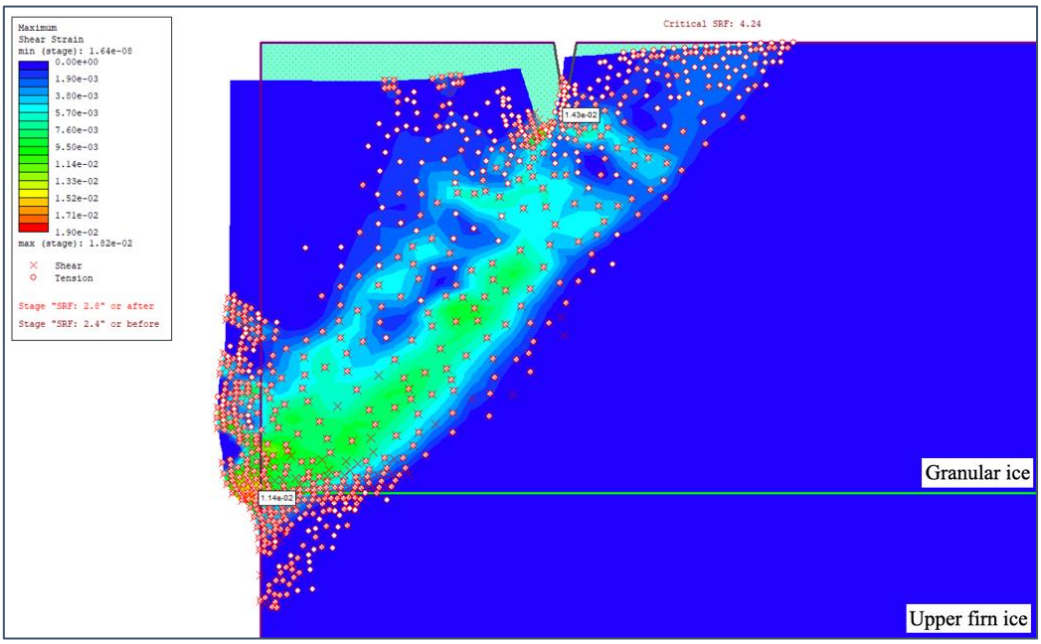

Figure 4-23: Failure HV shear strain contours

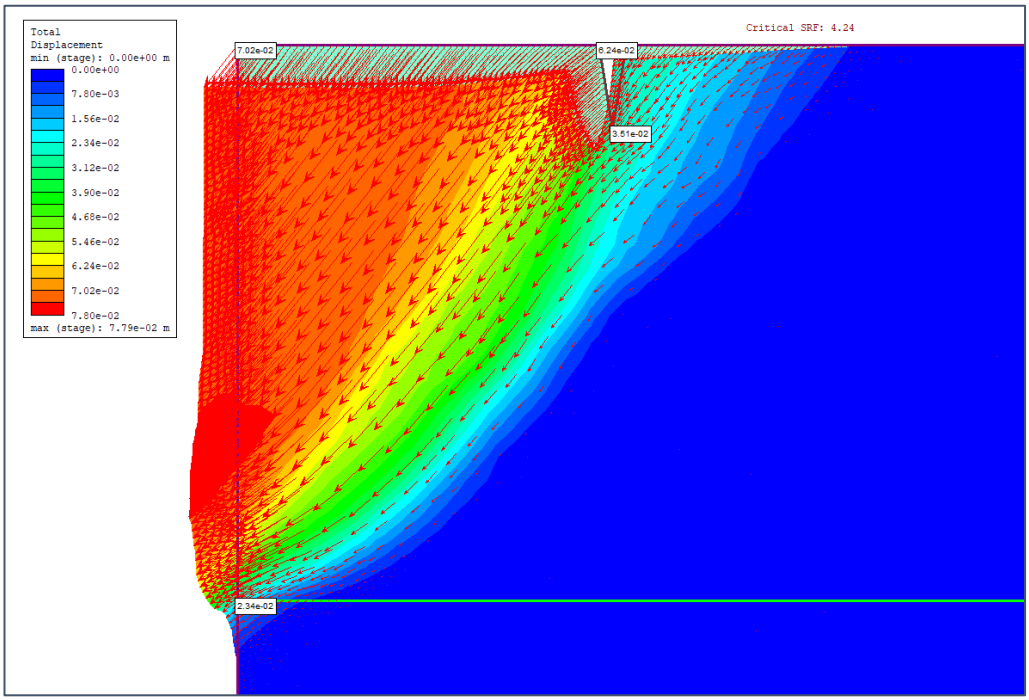

Figure 4-24: Failure HV displacement contours

Despite the cracking, the model was computed and considered safe with the high FS of 4.24. This is currently representative of the shelf edge as failure of the study area has not occurred. The model was also more representative than the base model due to the presence of a surface discontinuity, which are present in the shelf. It also shows deformation of the shelf edge outwards toward the open water. This was assessed to be a factor that would lead to crumbing of the shelf edge ice vertically downwards into the ocean. Despite the use of one crack scenario, which is less than what was found on the shelf edge, the deformation and function of the cliff edge was reminiscent of the actual shelf. A similar occurrence was observed in Figure 4-18.

4.6.2 Vertical variation

To communicate the results of the analyses, a graph of SRF against crack depth was plotted. The graph plotted showed negative a trend between SRF and crack depth where the SRF of the cliff reduced with increase of crack depth in Figure 4-25. To further assess the trend observed, the maximum shear strains experienced were also compared to their individual crack depths. This showed a positive trend with the maximum shear strain in the model, increasing with an increase in crack depth. Like the horizontal variations earlier, the maximum shear strains were observed at the bottom of the cracks in the critical SRF models, and at the material boundaries in the failure SRF models.

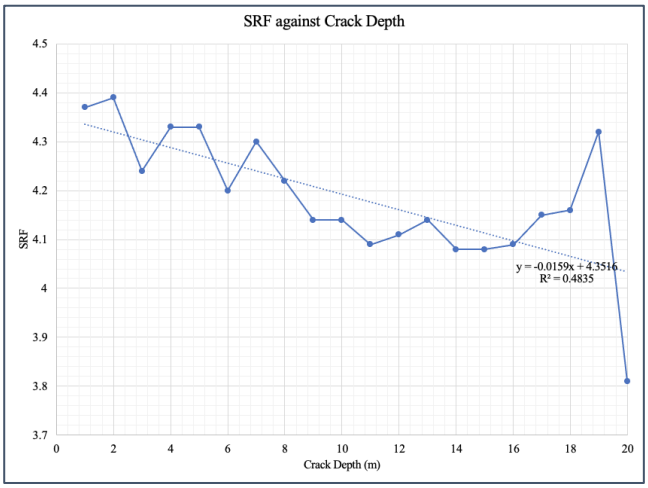

Figure 4-25: SRF against crack depth graph

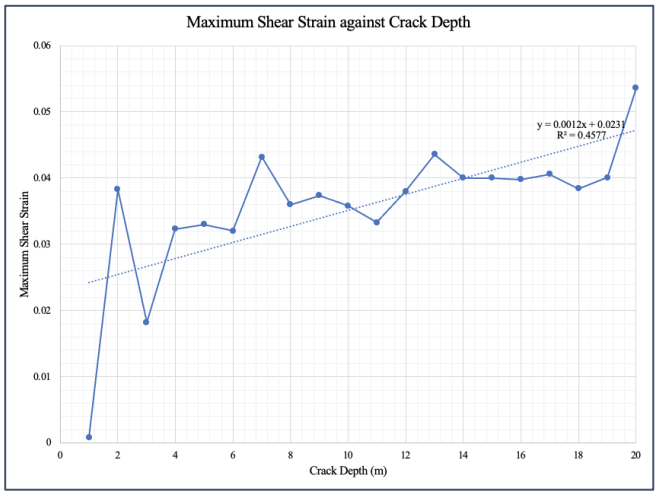

Figure 4-26: Maximum shear strain against crack depth graph

The vertical scenarios were carried out at a constant horizontal location of 13m from the shelf edge and constant crack width of 1m. Through analysis of the plotted graph in Figure 4-25, the existence of a crack within the shear zone significantly reduced the FS of the cliff with a drop of FS from 5.56 to 4.37 with a 1m deep crack. There was then a relatively consistent drop in SRF with increase in crack depth, seen due to the increase in shear strain experienced in the model observed in Figure 4-26. The increase in crack depths therefore caused increasing amounts of deformation to the ice material, eventually leading to the critical SRF values viewed in the plotted graph.

With that, the sequence of cliff failure according to the model is as follows. Cracks were formed through crack nucleation at the top of the shelf, which are made deeper through further propagation in tensile failure. The deeper cracks then led to formation of blocks with the potential to topple from the cliff structure. As the ice blocks deform outwards toward the ocean, crumbling of the overhanding material is assumed to occur due to shear. This is then proceeded by plane

failure through the formation of a shear plane. Contrary to the shear failure, in a scenario with multiple cracks with sufficient depth, toppling failure can be assumed to occur as well when the ice mass behind a toppling block fails and pushes the outer block over it base, as observed in the experiments in Figure 2-18.

4.7 Summary of chapter

In summary of the results, the sequence of results described in this Chapter followed the sequence of methods carried out. The main sections involved core characterisation, physical property results, strength results and finally, cliff modelling. Discussions were made for each of the Sections, describing results obtained in detail and their link to published literature sources.

Firstly, core characterisation was carried in terms of grainsize distribution, ice lens percentages and RQD. The grainsizes found in the shelf ice were fine grained, medium grained and large grained granular ice with bands of ice lenses through the core lengths. The percentages calculated for each were 19.6%, 62.4% and 17.9% respectively. The medium size was the most abundant on the shelf. It was followed by fine grained and finally large grained. This was assumed to be due to the ease of the finer grains to melt and refreeze into the medium grained ice, as compared to the medium grained to large grained metamorphism. It was also observed that the densities of the grainsizes decreased with increase in grainsize. This was attributed to the increase in porosity and air voids within the bigger grainsizes. The density of each of the grainsizes was tested to obtain the following values. Fine grained values had a density of 473.2kg/m^3, medium grained with 469.7kg/m^3 and large grained with 406.2kg/m^3. Leading to a trend where the density reduced with an increase in grainsize.

The ice lenses then had a percentage range of 0 - 33% of core length and an average density of 813.0kg/m^3. However, no trends were observed with regard to formation location or density. The concentrations of the lenses were plotted into an approximate study area map to show critical site areas with high ice lens concentrations. These showed critical areas with significant meltwater concentrations. These areas were marked as high risk due to the increased possibility of hydrofracturing in crevasses formed. The RQD of each of the cores was then calculated to give values within the 43 - 100% range. An average of all RQD reading was got as 76% with a standard deviation of 14.5%. The RQD was then finally taken as the degree of jointing with the value obtained reducing the maximum RMR and shear strength properties. This reduction of strength properties accounted for the joints or discontinuities represented by the RQD.

The physical properties of the ice were then tested and calculated. This was done in terms of density, Poisson's ratio, and elastic modulus. Taking an average for the entire shelf, the average density was calculated to be 569.9kg/m^3 with a standard deviation of 157.7kg/m^3. The average Poisson's ratio of the ice was then determined as 0.37 with a standard deviation of 0.06, and lastly Elastic modulus with an average value of 1.66GPa and standard deviation of 0.87GPa. The density of 569.9±157.5kg/m^3 was observed to be in agreement with authors like MacDonell

et al. (2021) and other granular ice density readings. Contrary to the density readings, elastic modulus readings for granular ice were observed to exist between literature values for snow and crystalline ice. Snow was seen to have values of 1MPa while crystalline ice had values of 9.0GPa. Therefore, the *E* values of 1.66±0.87GPa for granular ice were acceptable. Similar to *E*, Poisson's ratio for crystalline ice was observed to be about 0.31. With granular ice being less stiff, the value of 0.37±0.06 was justified.

Following the physical properties were the strength properties of the material. These were based on the UCS, shear strength and tensile strength of the material. The average UCS obtained was 0.9MPa with a standard deviation of 0.27MPa at a strain rate of $10^{-4.3}s^{-1}$ for ductile failure. Using the RMR method, a rating of 50 was got for the ice, giving a cohesion value of 0.25MPa and friction angle of 30°. These, together with the UCS, were used to calculate a shear strength of 0.77MPa for the material. The tensile strength was finally obtained as 0.25MPa, due to its direct relation to the cohesion value determined. The UCS values obtained were viewed to be similar to laboratory created snow in Wang, E. *et al.* (2021) but weaker than crystalline ice tested by a number of authors. In terms of shear strength, a similar relationship was observed with the value obtained higher than snow but less than crystalline ice. This was also the case for friction angle values. With that, the shear strength was viewed to be less than the strength of crystalline ice. All the properties exhibited higher strengths than snow values but weaker than crystalline ice. This was attributed to the higher strength of ice bonds in the crystalline ice than granular ice, whose are in turn stronger than snow bonds.

Finally, the software modelling was conducted and broken down into 3 phases: the base model, horizontal crack variation and vertical crack depth variation. A base model was built and run to give a critical FS of 5.56. During the horizontal variations, the critical crack location was found at 13m from the shelf edge with the lowest FS value of 4.24. Finally, for the increase in crack depth at the critical horizontal location, the FS was viewed to decrease. Together with that, an increase in maximum shear strain was observed with increase in crack depth.

The critical base FS was 5.56, giving a critical cohesion value of 45kPa and angle of friction of 5.4°. Failure occurred in both tension and shear, due to the tension which the model experienced at the surface and Mohr Coulomb failure criterion used. In the horizontal variation, 4 failure regimes were observed. The critical regime existed between a 9 - 20m crack distance away from the shelf edge. This was critical because the crack existed within the shear zone of the cliff. It negated the tensile strength of the top layer of shelf, thus aggravating the failure. The critical location was at 13m with a FS of 4.24. The failure types observed were crevasse formation through crack propagation, which could in turn become toppling failure when cracks reached a significant depth. When shear occurred, planar failure was observed, with an assumed crumbling of the overhanging part of the ice. Finally, the increasing crack depth at the critical horizontal location led to decrease in SRF. This was viewed to be due to the increase in shear strain experienced by the model at higher crack depths. Multiple deep cracks were also viewed as the catalyst of formation of toppling blocks and toppling failure.

5 Conclusions and Recommendations

To characterise the granular ice found in the study area on the Fimbul ice shelf, the material properties were tested. These included density, Young's modulus, Poisson's ratio, and various strength parameters. To then apply the obtained knowledge into the problem presented, a slope stability analysis was carried out for the ice shelf cliff using Rocscience's RS2 FEM software.

The output from the material property tests were material parameters that quantitatively defined the behaviour of the material. These were used as layer parameters for the granular layer of the ice shelf model, which in turn output factor of safety values for the cliff. These values were used to quantify the safety of the cliff, withing the limits of the scope of study. This Chapter therefore extracts the key conclusions from the study and offers reference to recommendations and future work that could be developed from this study.

5.1 Conclusions

In relation to the initial objectives, the following are the research conclusions:

The Fimbul granular ice on the shelf comprised of both granular and crystalline ice. The granular ice was divided into fine, medium, and large grainsizes, with the medium grainsize being the most abundant on the shelf. The granular sizes showed no definite arrangement with depth into the ice shelf. The crystalline ice existed in form of ice lenses which were formed through freezing of precipitation or recrystallised meltwater. These also existed at random heights, but concentrations showed areas on the ice shelf with higher meltwater and increased possibilities crevasse formation through hydrofracturing or tensile failure at crack tips.

In terms of the physical properties, the dominant density on the shelf was that of the medium grained samples with an average of 469.7kg/m^3. This was however influenced by the ice lenses, raising the average material density to 569.9±157.46kg/m^3. The elastic modulus and Poisson's ratios were obtained using non-destructive acoustic methods giving average values of 1.66±0.87GPa and 0.37±0.06 respectively. This showed the relatively high deformity potential of the material in both the axial and lateral directions.

The deformity of the material was observed during UCS test with the ductile failure observed. The average strength of the material was found to be 0.9±0.27MPa. This value was further used in the RMR alongside other factors to obtain the cohesion and angle of friction shear strength properties as 0.25MPa or 250kPa and 30° respectively. These further led to the determination of a shear strength of 0.77MPa or 770kPa which was implemented in the modelling phase.

Failure on the shelf was analysed and viewed in the granular material in 3 different methods. First was a slip surface induced by shear failure on the base shelf model with a FS of 5.56. When carrying out the case studies on crack location, the critical horizontal crack location was viewed at 13m from the shelf edge due to its position in the shear failure zone. The FS of

this scenario was 4.24. The SRF/FS was then viewed to have a negative relationship with crack depth where the SRF reduced with increase in crack depth. This was concluded to be due to the increase in shear strain that occurred with an increase in crack depth.

In conclusion, the material properties obtained through property and characterisation tests were used in the cliff model which gave FS values of 3.81 to 5.56. Therefore, the cliff can be currently viewed as stable, based on the scope of this study. However, this is subject to change due to the rising levels of global warming on the planet which would have a direct impact on reduction of shear strength parameters and amount of melting on the ice shelf, and hence a factor to hydrofracturing and loss of shelf stability.

5.2 Recommendations addressing Study Limitations

To further studies on the shelf and reduce the limitations experienced in this study, the following recommendations have been made:

1. During the recent Antarctic voyage, limitations to the equipment used meant that the cores retrieved only offered direct information about the top 2m of the ice shelf. To understand the stratigraphy of the shelf for more detailed layer modelling, drilling and study of deeper cores would provide more accurate information about the ice.
2. In addition to the deeper coring, a more detailed site investigation could be carried out on the shelf. This could involve a survey marking accurate crack locations and tests like the CPT to obtain layering data and strength characteristics about the shelf. In addition to the surveys, detailed information about the tidal levels and wave action on the shelf could be investigated. This could all be used for more realistic 3D cliff stability modelling of the shelf edge.
3. Obtaining information about the micro-scale features of the ice samples was heavily limited by the unavailability of equipment capable of preparing and observing thin sections of granular ice. The use of more specialised equipment like Scanning Electron Microscopes may be implemented to obtained more detailed material properties like quantitative grainsize measurements.
4. Determination of elastic modulus, UCS, and strain were each carried out using different equipment, which induced an array of errors and levels of uncertainty to the results obtained. To prevent this limitation, use of a constant strain rate load press, equipped with both load and displacement sensors, would be recommended to measure all the mentioned parameters in real time by the more accurate piece of equipment.
5. In contrast to using the limited classification methods (RQD & RMR) to obtain shear strength, the direct shear method could be adopted and modified for the ice samples. This would directly enable the calculation of cohesion and angle of friction properties for the specific material.

References

Adhikary, D., Dyskin, A., Jewell, R. & Stewart, D. 1997. A study of the mechanism of flexural toppling failure of rock slopes. *Rock mechanics and rock engineering.* 30(2):75.

Aksoy, C. 2008. Review of rock mass rating classification: historical developments, applications, and restrictions. *Journal of mining science.* 44:51-63.

Alemdag, S., Akgun, A., Kaya, A. & Gokceoglu, C. 2014. A large and rapid planar failure: causes, mechanism, and consequences (Mordut, Gumushane, Turkey). *Arabian Journal of Geosciences.* 7:1205-1221.

Alley, K., Scambos, T., Miller, J., Long, D. & MacFerrin, M. 2018. Quantifying vulnerability of Antarctic ice shelves to hydrofracture using microwave scattering properties. *Remote Sensing of Environment.* 210:297-306.

Andrews, R. 1985. Measurement of the fracture toughness of glacier ice. *Journal of Glaciology.* 31(108):171-176.

Bassis, J.N. & Walker, C.C. 2012. Upper and lower limits on the stability of calving glaciers from the yield strength envelope of ice. *Proceedings of the Royal Society A: Mathematical, Physical and Engineering Sciences.* 468(2140):913-931.

Bassis, J.N., Berg, B., Crawford, A. & Benn, D. 2021. Transition to marine ice cliff instability controlled by ice thickness gradients and velocity. *Science.* 372(6548):1342-1344.

Bieniawski, Z. Ed. 1979. The geomechanics classification in rock engineering applications. OnePetro.

Böhm, A.M., Herrnring, H. & und Polach, F.v.B. 2022. Data from uniaxial compressive testing of laboratory-made granular ice. *Data in Brief.* 42:108236.

British Antarctic Survey, L. 2023. *Antartica Overview Map*. Available: https://lima.usgs.gov [2023, 05/11/2023].

Brotons, V., Tomás, R., Ivorra, S., Grediaga, A., Martínez-Martínez, J., Benavente, D. & Gómez-Heras, M. 2016. Improved correlation between the static and dynamic elastic modulus of different types of rocks. *Materials and structures.* 49(8):3021-3037.

Burgin, M. 2016. *Theory of knowledge: structures and processes.* World scientific.

Campbell, I.B. & Claridge, G.G.C. 1987. *Antarctica: soils, weathering processes and environment.* Elsevier.

Cole, D.M. 2001. The microstructure of ice and its influence on mechanical properties. *Engineering fracture mechanics.* 68(17-18):1797-1822.

Craig, R.F. 2004. *Craig's soil mechanics.* CRC press.

Crawford, A.J., Benn, D.I., Todd, J., Åström, J.A., Bassis, J.N. & Zwinger, T. 2021. Marine ice-cliff instability modeling shows mixed-mode ice-cliff failure and yields calving rate parameterization. *Nature communications.* 12(1):1-9.

Deere, D. & Deere, D. Eds. 1988. The rock quality designation (RQD) index in practice.

Dierckx, M. & Tison, J.L. 2013. Marine ice deformation experiments: an empirical validation of creep parameters. *Geophysical research letters.* 40(1):134-138.

Doake, C. 2001. Ice-shelf stability. *Encyclopedia of Ocean Sciences.*1282 - 1290.

Eberhardt, E. 2003. Rock slope stability analysis–utilization of advanced numerical techniques. *Earth and Ocean sciences at UBC.*41.

Han, H., Li, Z., Huang, W., Lu, P. & Lei, R. 2015. The uniaxial compressive strength of the Arctic summer sea ice. *Acta oceanologica sinica.* 34(1):129-136.

Hanessian, J. 1960. The Antarctic Treaty 1959. *International & Comparative Law Quarterly.* 9(3):436-480.

Hoek, E. & Bray, J.D. 1981. *Rock slope engineering.* CRC Press.

Howland, A. & Gardiner, V. 1986. The natural process of degradation of an overconsolidated clay under differing climatic conditions as illustrated by the Weald Clay. *International Geomorphology.* 1986(Part 1):139-154.

Hutchings, J.K., Heil, P., Lecomte, O., Stevens, R., Steer, A. & Lieser, J.L. 2015. Comparing methods of measuring sea-ice density in the East Antarctic. *Annals of Glaciology.* 56(69):77-82.

Jaeger, J.C., Cook, N.G. & Zimmerman, R. 2009. *Fundamentals of rock mechanics.* John Wiley & Sons.

Ji, S., Di, S. & Long, X. 2017. DEM simulation of uniaxial compressive and flexural strength of sea ice: parametric study. *Journal of Engineering Mechanics.* 143(1):C4016010.

Jiang, Q., Liu, X., Wei, W. & Zhou, C. 2013. A new method for analyzing the stability of rock wedges. *International Journal of Rock Mechanics and Mining Sciences.* 60:413-422.

Kennicutt, M.C., Chown, S.L., Cassano, J.J., Liggett, D., Massom, R., Peck, L.S., Rintoul, S.R., Storey, J.W. et al. 2014. Polar research: six priorities for Antarctic science. *Nature.* 512(7512):23-25.

Kinar, N. & Pomeroy, J. 2015. Measurement of the physical properties of the snowpack. *Reviews of Geophysics.* 53(2):481-544.

Kovacs, A. 1997. Estimating the full-scale flexural and compressive strength of first-year sea ice. *Journal of Geophysical Research: Oceans.* 102(C4):8681-8689.

Kulyakhtin, S. & Høyland, K.V. Eds. 2014. Study of the volumetric behaviour of ice rubble based on bi-axial compression data. American Society of Mechanical Engineers. V010T007A027.

Kundu, J., Sarkar, K., Singh, A.K. & Singh, T. 2020. Continuous functions and a computer application for Rock Mass Rating. *International Journal of Rock Mechanics and Mining Sciences.* 129:104280.

Lawn, B. 1993. Fracture of brittle solids. *(No Title).*194.

Li, Y., Qiu, X., Ge, Y., Wang, J. & Chen, S. Eds. 2018. Research on the Failure Criterion of Snow-Ice Constitutive Model. IEEE. 409-412.

Libbrecht, K.G. 2001. Morphogenesis on ice: The physics of snow crystals. *Engineering and Science.* 64(1):10-19.

Ligneau, C., Sovilla, B. & Gaume, J. 2022. Numerical investigation of the effect of cohesion and ground friction on snow avalanches flow regimes. *Plos one.* 17(2):e0264033.

Lou, X. & Wu, Y. 2022. Influence of temperature and fiber content on direct shear properties of plain ice and fiber-reinforced ice. *Cold Regions Science and Technology.* 194:103458.

Lucian, C. & Wangwe, E. 2013. The usefulness of rock quality designation (RQD) in determining strength of the rock. *International Refereed Journal of Engineering and Science.* 2(9):36-40.

Luka, W. & Keith, M. 2021. *Mapping and Ground Penetrating Radar (GPR) survey of surface cracking and crevasse on the SANAE IV Re-supply traverse, Antarctica.* Unpublished.

MacDonell, S., Fernandoy, F., Villar, P. & Hammann, A. 2021. Stratigraphic analysis of firn cores from an antarctic ice shelf firn aquifer. *Water.* 13(5):731.

Masterson, D. 2009. State of the art of ice bearing capacity and ice construction. *Cold Regions Science and Technology.* 58(3):99-112.

McCallum, A. 2014. Cone penetration testing (CPT) in Antarctic firn: an introduction to interpretation. *Journal of Glaciology.* 60(219):83-93. DOI:10.3189/2014JoG12J214.

Nguyen, N.H., Bui, H.H., Nguyen, G.D. & Kodikara, J. 2017. A cohesive damage-plasticity model for DEM and its application for numerical investigation of soft rock fracture properties. *International Journal of Plasticity.* 98:175-196.

Nøst, O.A. 2004. Measurements of ice thickness and seabed topography under the Fimbul Ice Shelf, Dronning Maud Land, Antarctica. *Journal of Geophysical Research: Oceans.* 109(C10).

Pantelidis, L. 2009. Rock slope stability assessment through rock mass classification systems. *International Journal of Rock Mechanics and Mining Sciences.* 46(2):315-325.

Pappalardo, G. & Mineo, S. 2022. Static elastic modulus of rocks predicted through regression models and Artificial Neural Network. *Engineering Geology.* 308:106829.

Park, H. & West, T. 2001. Development of a probabilistic approach for rock wedge failure. *Engineering Geology.* 59(3-4):233-251.

Paronuzzi, P., Rigo, E. & Bolla, A. 2013. Influence of filling–drawdown cycles of the Vajont reservoir on Mt. Toc slope stability. *Geomorphology.* 191:75-93.

Pattyn, F. 2018. The paradigm shift in Antarctic ice sheet modelling. *Nature communications.* 9(1):1-3.

Petrovic, J.J. 2003. Review Mechanical properties of ice and snow. *Journal of Materials Science.* 38(1):1-6. DOI:10.1023/A:1021134128038.

Podolskiy, E.A., Chambon, G., Naaim, M. & Gaume, J. 2015. Evaluating snow weak-layer failure parameters through inverse finite element modelling of shaking-platform experiments. *Natural Hazards and Earth System Sciences.* 15(1):119-134.

Pollard, D. & DeConto, R. n.d. The birth and death of ice sheets: Understanding the past and predicting the future.

Pollard, D., DeConto, R.M. & Alley, R.B. 2015. Potential Antarctic Ice Sheet retreat driven by hydrofracturing and ice cliff failure. *Earth and Planetary Science Letters.* 412:112-121.

Pustogvar, A. & Kulyakhtin, A. 2016. Sea ice density measurements. Methods and uncertainties. *Cold Regions Science and Technology*. 131:46-52.

Raghuvanshi, T.K. 2019. Plane failure in rock slopes–A review on stability analysis techniques. *Journal of King Saud University-Science*. 31(1):101-109.

Randhawa, K.S. 2018. The measurement of the Young's modulus of ice with ultrasonic waves. Technische Universität Hamburg.

Reiweger, I., Gaume, J. & Schweizer, J. 2015. A new mixed-mode failure criterion for weak snowpack layers. *Geophysical research letters*. 42(5):1427-1432.

Rist, M., Sammonds, P., Oerter, H. & Doake, C. 2002. Fracture of Antarctic shelf ice. *Journal of Geophysical Research: Solid Earth*. 107(B1):ECV 2-1-ECV 2-13.

Rosu-Finsen, A., Davies, M.B., Amon, A., Wu, H., Sella, A., Michaelides, A. & Salzmann, C.G. 2023. Medium-density amorphous ice. *Science*. 379(6631):474-478.

Salaamah, A.F., Fathani, T.F. & Wilopo, W. 2018. Correlation of P-wave velocity with rock quality designation (RQD) in volcanic rocks. *Journal of Applied Geology*. 3(2):62-72.

Scambos, T., Fricker, H.A., Liu, C.-C., Bohlander, J., Fastook, J., Sargent, A., Massom, R. & Wu, A.-M. 2009. Ice shelf disintegration by plate bending and hydro-fracture: Satellite observations and model results of the 2008 Wilkins ice shelf break-ups. *Earth and Planetary Science Letters*. 280(1-4):51-60.

Schulson, E.M. 2001. Brittle failure of ice. *Engineering fracture mechanics*. 68(17-18):1839-1887.

Schulson, E.M. & Duval, P. 2009. *Creep and fracture of ice*. Cambridge university press.

Serré, N. 2011. Mechanical properties of model ice ridge keels. *Cold Regions Science and Technology*. 67(3):89-106.

Shazly, M., Prakash, V. & Lerch, B.A. 2009. High strain-rate behavior of ice under uniaxial compression. *International Journal of Solids and Structures*. 46(6):1499-1515. DOI:https://doi.org/10.1016/j.ijsolstr.2008.11.020.

Singh, B. & Goel, R.K. 1999. *Rock mass classification: a practical approach in civil engineering*. Elsevier.

Sinha, N.K. 1989. Elasticity of natural types of polycrystalline ice. *Cold Regions Science and Technology*. 17(2):127-135.

Sinha, N.K. & Shokr, M. 2015. *Sea ice: physics and remote sensing*. John Wiley & Sons.

Skatulla, S., Audh, R.R., Cook, A., Hepworth, E., Johnson, S., Lupascu, D.C., MacHutchon, K., Marquart, R. et al. 2022. Physical and mechanical properties of winter first-year ice in the Antarctic marginal ice zone along the Good Hope Line. *The Cryosphere*. 16(7):2899-2925.

Spaulding, N., Meese, D., Baker, I., Mayewski, P.A. & Hamilton, G.S. 2010. A new technique for firn grain-size measurement using SEM image analysis. *Journal of Glaciology*. 56(195):12-19.

Stead, D. & Wolter, A. 2015. A critical review of rock slope failure mechanisms: the importance of structural geology. *Journal of Structural Geology*. 74:1-23.

Turner, J., Lu, H., King, J., Marshall, G.J., Phillips, T., Bannister, D. & Colwell, S. 2021. Extreme temperatures in the Antarctic. *Journal of Climate.* 34(7):2653-2668.

Turner, J., Barrand, N.E., Bracegirdle, T.J., Convey, P., Hodgson, D.A., Jarvis, M., Jenkins, A., Marshall, G. et al. 2014. Antarctic climate change and the environment: an update. *Polar record.* 50(3):237-259.

Vignon, É., Roussel, M.L., Gorodetskaya, I., Genthon, C. & Berne, A. 2021. Present and future of rainfall in Antarctica. *Geophysical research letters.* 48(8):e2020GL092281.

Wang, E., Fu, X., Han, H., Liu, X., Xiao, Y. & Leng, Y. 2021. Study on the mechanical properties of compacted snow under uniaxial compression and analysis of influencing factors. *Cold Regions Science and Technology.* 182:103215.

Wang, Q., Li, Z., Lei, R., Lu, P. & Han, H. 2018. Estimation of the uniaxial compressive strength of Arctic sea ice during melt season. *Cold Regions Science and Technology.* 151:9-18. DOI:https://doi.org/10.1016/j.coldregions.2018.03.002.

Weller, G. 1992. Antarctica and the detection of environmental change. *Philosophical Transactions of the Royal Society of London. Series B: Biological Sciences.* 338(1285):201-208.

White, G. & McCallum, A. 2018. Review of ice and snow runway pavements. *International Journal of Pavement Research and Technology.* 11(3):311-320. DOI:https://doi.org/10.1016/j.ijprt.2017.11.002.

Wyllie, D.C. & Mah, C. 2004. *Rock slope engineering.* CRC Press.

Yasui, M., Schulson, E.M. & Renshaw, C.E. 2017. Experimental studies on mechanical properties and ductile-to-brittle transition of ice-silica mixtures: Young's modulus, compressive strength, and fracture toughness. *Journal of Geophysical Research: Solid Earth.* 122(8):6014-6030.

Zhang, L. 2016. Determination and applications of rock quality designation (RQD). *Journal of Rock Mechanics and Geotechnical Engineering.* 8(3):389-397.

Zhang, Y., Zhang, Y., Guo, R. & Cui, B. 2022. Method for Testing Shear and Tensile Strengths of Freshwater/Seawater Ice. *Water.* 14(9):1363.

Zhang, Y., Qian, Z., Lv, S., Huang, W., Ren, J., Fang, Z. & Chen, X. 2022. Experimental Investigation of Uniaxial Compressive Strength of Distilled Water Ice at Different Growth Temperatures. *Water.* 14(24):4079.

Appendices

List of Appendices

The appendices have been segmented into the following categories:

Appendix A Core log sheets

Appendix B SolidWorks drawings

Appendix C Material property results

Appendix D Ethics Clearance

Appendix A – Core log sheets

2021/2022 Antarctic Ice Core logging	Core Number	Coordinates	-70,258S	-2,702W
		Shelf Region	E1	
	1	Length	≈111cm	
		Set temp.	- 20 degrees C	
		Actual temp.	-20 +- 2 degrees C	

Lens location	Stratigraphy	Core Image	Test Sections	Description
		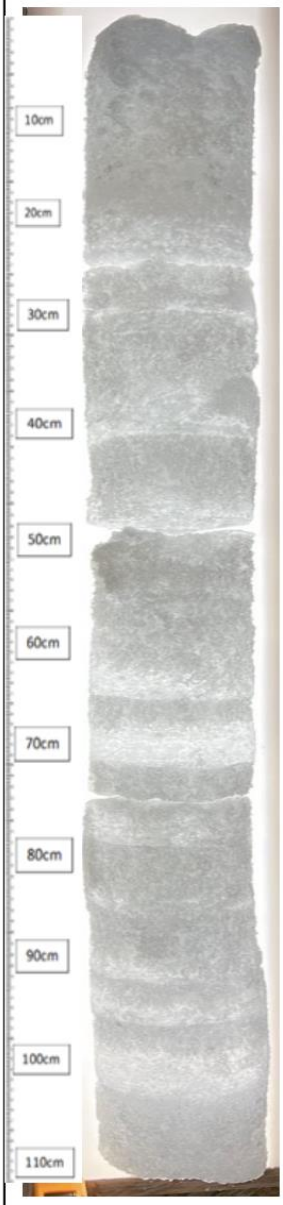		Ice core mostly comprised of medium grained ice with scattered ice lenses
			C1-1	Mixed ice section used for calibration of compression tests
			C1-2	Mixed ice section used for calibration of compression tests

KEY

- Fine grained
- Medium grained
- Large grained
- Sample extracted
- Ice lens

2021/2022 Antarctic Ice Core logging	Core Number	Coordinates	-70,2578S -2,7023W
		Shelf Region	E2
	2	Length	≈105cm
		Set temp.	- 20 degrees C
		Actual temp.	-20 +- 2 degrees

Lens location	Stratigraphy	Core Image	Test Sections	Description
		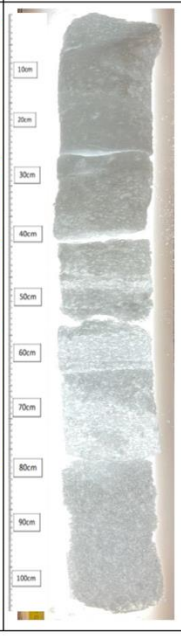	C2-2	Top part of the core is an ice lens with a high granular particles Right size for compression testing
			2/01/E1	Large Ice lens allowed high leeway for failure, thus ideal location for Thin section analysis
			C2-1	Compression test done on large granular section location at bottom of sample, very uniform granule size.

2021/2022 Antarctic Ice Core logging	Core Number	Coordinates	-70,2571S -2,7019W
		Shelf Region	D2
	3	Length	≈115cm
		Set temp.	- 20 degrees C
		Actual temp.	-20 +- 2 degrees

Lens location	Stratigraphy	Core Image	Test Sections	Description
		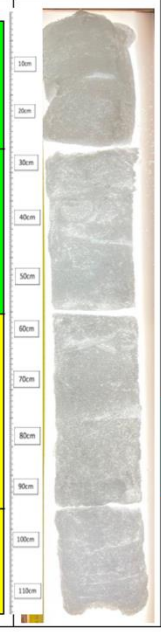		Top of the core has a large ice lens with high bubble concentrations. Lower ice lens contains the same lens characteristics
				Ice lenses with granular ice throughout the core
			C3-1	Ice lens with granular ice. Sufficient length for compressions testing

2021/2022 Antarctic Ice Core logging	Core Number	Coordinates	-70,2581S -2,7016W
		Shelf Region	F2
	4	Length	≈120cm
		Set temp.	- 20 degrees C
		Actual temp.	-20 +- 2 degrees C

Lens location	Stratigraphy	Core Image	Test Sections	Description
		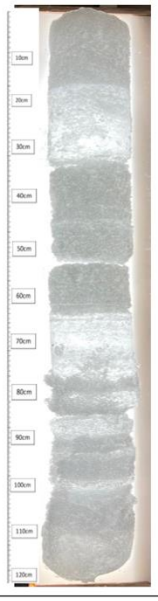	4/01/F2	Large ice lens allowed ideal location to perform both a thin section analysis along with a density test, will hopefully allow for test cross reference.
			D4-1	
			C4-1	Compression test chosen for large uniform section of grain size
			D4-2	Uniform Ice lens section used for density
			4/02/F2	Thick ice lens ideal for thin section refinement

2021/2022 Antarctic Ice Core logging	Core Number	Coordinates	-70,2569S -2,7013W
		Shelf Region	C2
	5	Length	≈110cm
		Set temp.	- 20 degrees C
		Actual temp.	-20 +- 2 degrees C

Lens location	Stratigraphy	Core Image	Test Sections	Description
		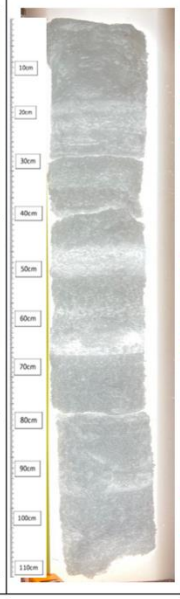	D5-A	2 sections with similar, yet slightly differing grain distributions identified as ideal targets for density comparison.
			D5-B	
			5/01/C2	
			D5-C	A clustering of ice lenses and density tests done in a nearby region to allow for 4 similar sets of cross reference.
			5/02/C2	
			D5-D	
			D5-E	Density test performed on the bottom of the sample of likely uniform density.

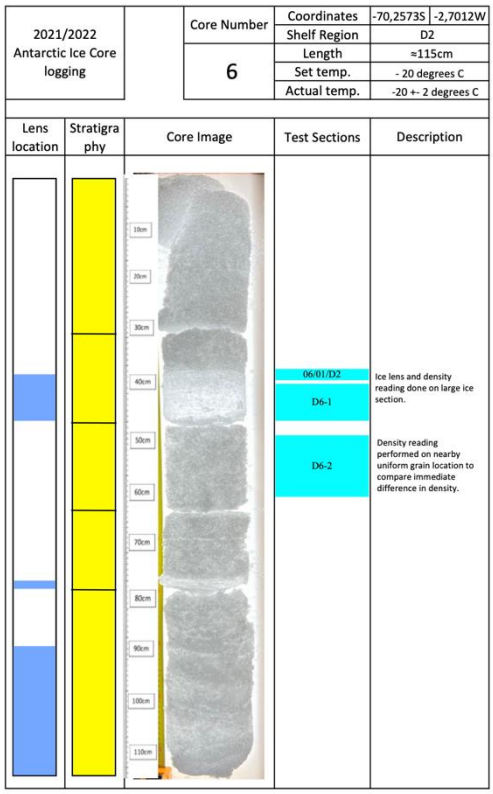
2021/2022 Antarctic Ice Core logging
Core Number
6
Coordinates -70,2573S -2,7012W
Shelf Region D2
Length ≈115cm
Set temp. - 20 degrees C
Actual temp. -20 +- 2 degrees C
Lens location
Stratigraphy
Core Image
Test Sections
Description
06/01/D2
Ice lens and density reading done on large ice section.
D6-1
D6-2
Density reading performed on nearby uniform grain location to compare immediate difference in density.

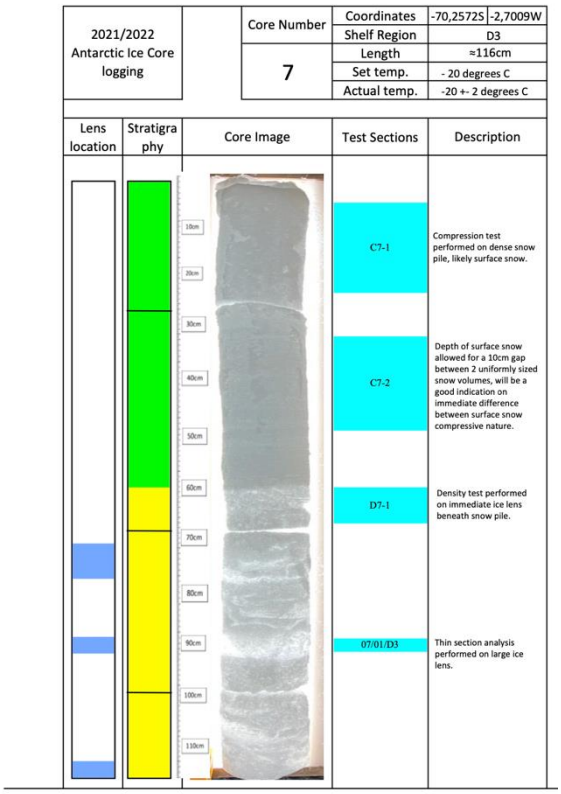
2021/2022 Antarctic Ice Core logging
Core Number
7
Coordinates -70,2572S -2,7009W
Shelf Region D3
Length ≈116cm
Set temp. - 20 degrees C
Actual temp. -20 +- 2 degrees C
Lens location
Stratigraphy
Core Image
Test Sections
Description
C7-1
Compression test performed on dense snow pile, likely surface snow.
C7-2
Depth of surface snow allowed for a 10cm gap between 2 uniformly sized snow volumes, will be a good indication on immediate difference between surface snow compressive nature.
D7-1
Density test performed on immediate ice lens beneath snow pile.
07/01/D3
Thin section analysis performed on large ice lens.

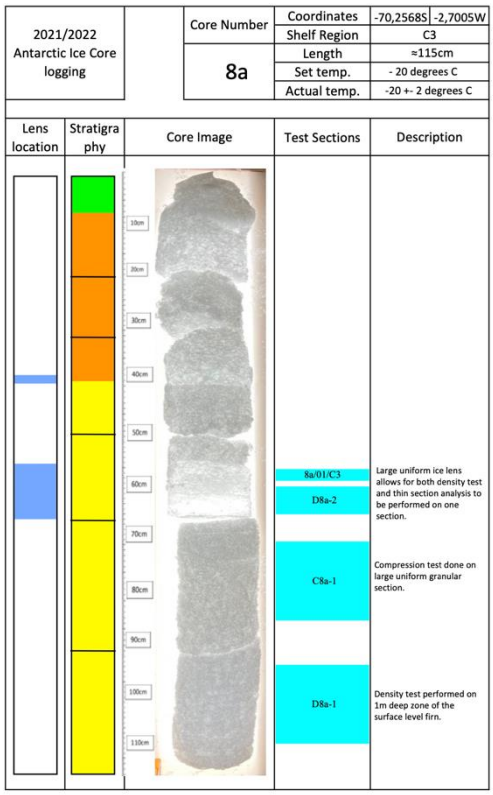
2021/2022 Antarctic Ice Core logging
Core Number
8a
Coordinates -70,2568S -2,7005W
Shelf Region C3
Length ≈115cm
Set temp. - 20 degrees C
Actual temp. -20 +- 2 degrees C
Lens location
Stratigraphy
Core Image
Test Sections
Description
8a/01/C3
Large uniform ice lens allows for both density test and thin section analysis to be performed on one section.
D8a-2
C8a-1
Compression test done on large uniform granular section.
D8a-1
Density test performed on 1m deep zone of the surface level firn.

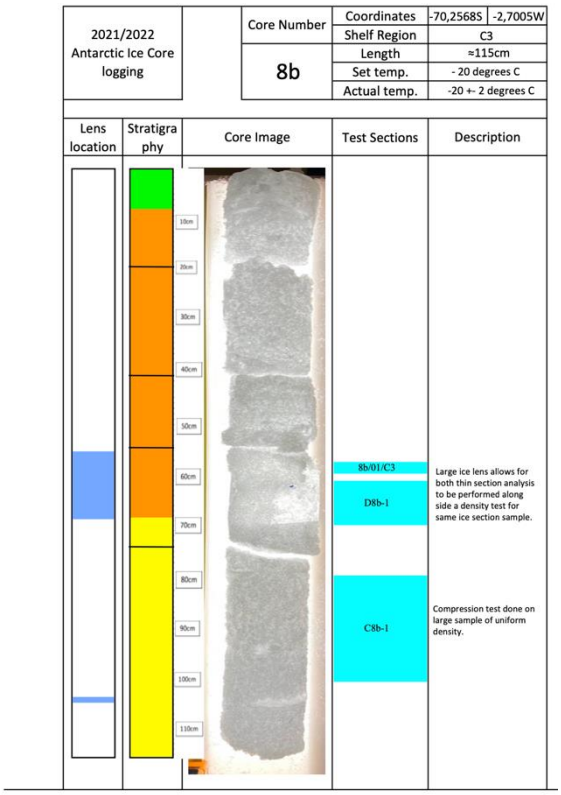
2021/2022 Antarctic Ice Core logging
Core Number
8b
Coordinates -70,2568S -2,7005W
Shelf Region C3
Length ≈115cm
Set temp. - 20 degrees C
Actual temp. -20 +- 2 degrees C
Lens location
Stratigraphy
Core Image
Test Sections
Description
8b/01/C3
Large ice lens allows for both thin section analysis to be performed along side a density test for same ice section sample.
D8b-1
C8b-1
Compression test done on large sample of uniform density.

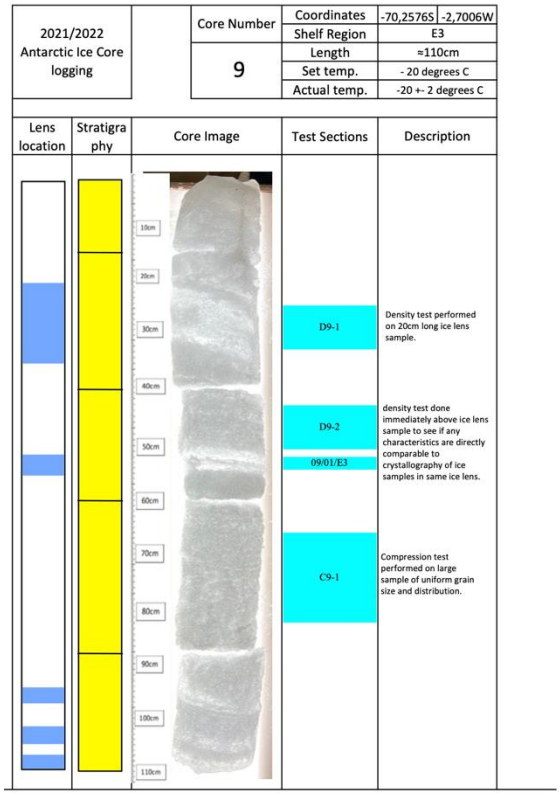
2021/2022 Antarctic Ice Core logging
Core Number
9
Coordinates
-70,2576S -2,7006W
Shelf Region
E3
Length
≈110cm
Set temp.
- 20 degrees C
Actual temp.
-20 +- 2 degrees C
Lens location
Stratigra phy
Core Image
Test Sections
Description
D9-1
Density test performed on 20cm long ice lens sample.
D9-2
density test done immediately above ice lens sample to see if any characteristics are directly comparable to crystallography of ice samples in same ice lens.
09/01/E3
C9-1
Compression test performed on large sample of uniform grain size and distribution.

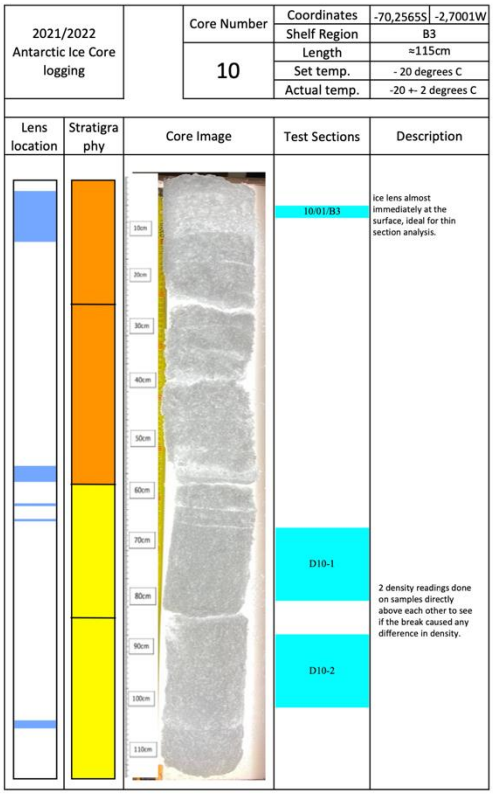
2021/2022 Antarctic Ice Core logging
Core Number
10
Coordinates
-70,2565S -2,7001W
Shelf Region
B3
Length
≈115cm
Set temp.
- 20 degrees C
Actual temp.
-20 +- 2 degrees C
Lens location
Stratigra phy
Core Image
Test Sections
Description
10/01/B3
ice lens almost immediately at the surface, ideal for thin section analysis.
D10-1
D10-2
2 density readings done on samples directly above each other to see if the break caused any difference in density.

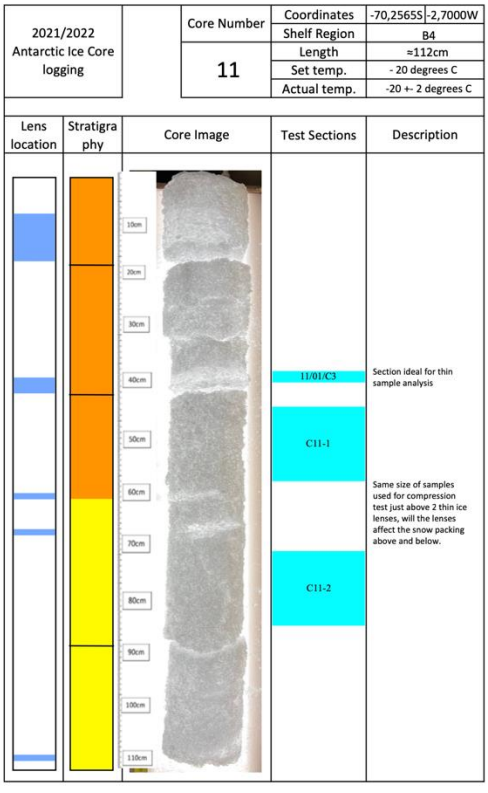
2021/2022 Antarctic Ice Core logging
Core Number
11
Coordinates
-70,2565S -2,7000W
Shelf Region
B4
Length
≈112cm
Set temp.
- 20 degrees C
Actual temp.
-20 +- 2 degrees C
Lens location
Stratigra phy
Core Image
Test Sections
Description
11/01/C3
Section ideal for thin sample analysis
C11-1
Same size of samples used for compression test just above 2 thin ice lenses, will the lenses affect the snow packing above and below.
C11-2

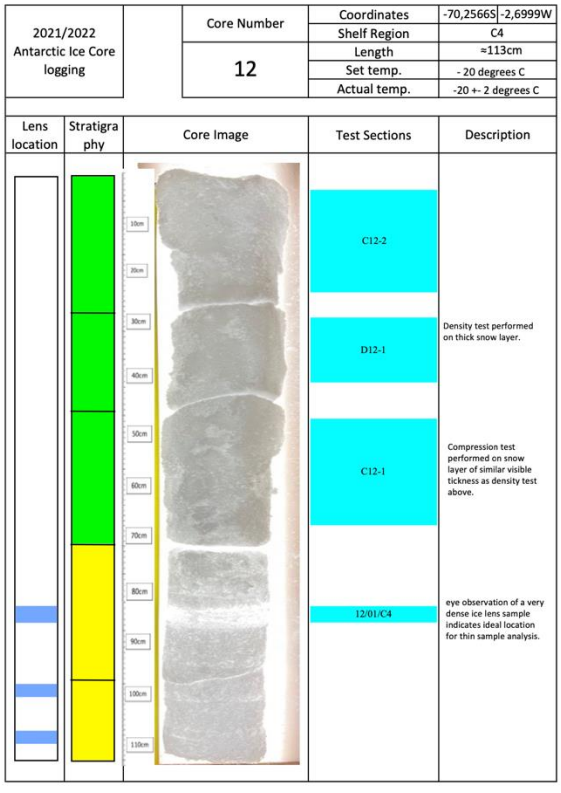
2021/2022 Antarctic Ice Core logging
Core Number
12
Coordinates
-70,2566S -2,6999W
Shelf Region
C4
Length
≈113cm
Set temp.
- 20 degrees C
Actual temp.
-20 +- 2 degrees C
Lens location
Stratigra phy
Core Image
Test Sections
Description
C12-2
D12-1
Density test performed on thick snow layer.
C12-1
Compression test performed on snow layer of similar visible tickness as density test above.
12/01/C4
eye observation of a very dense ice lens sample indicates ideal location for thin sample analysis.

2021/2022 Antarctic Ice Core logging	Core Number	Coordinates	-70,2572S -2,7002W
		Shelf Region	D3
	13a	Length	≈108cm
		Set temp.	- 20 degrees C
		Actual temp.	-20 +- 2 degrees C

Lens location	Stratigraphy	Core Image	Test Sections	Description
		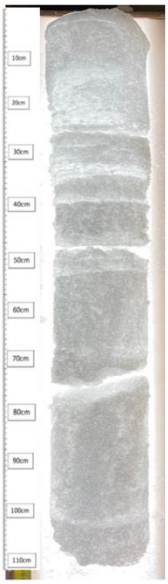	D13-1	Density and thin section analysis performed on large ice lens.
			13/01/D3	
			C13-2	
			D13-2	Density test performed on highly granular layer.
			C13-1	Compression test performed on highly granular layer. visible tickness as density test above.

2021/2022 Antarctic Ice Core logging	Core Number	Coordinates	-70,2572S -2,7002W
		Shelf Region	D3
	13b	Length	≈110cm
		Set temp.	- 20 degrees C
		Actual temp.	-20 +- 2 degrees C

Lens location	Stratigraphy	Core Image	Test Sections	Description
		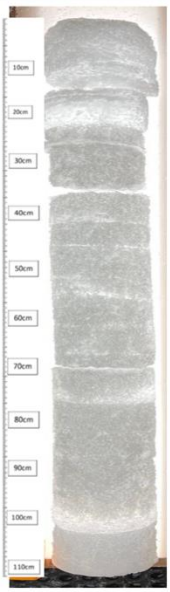		

2021/2022 Antarctic Ice Core logging	Core Number	Coordinates	-70,2573S -2,6998W
		Shelf Region	D4
	14	Length	≈107cm
		Set temp.	- 20 degrees C
		Actual temp.	-20 +- 2 degrees C

Lens location	Stratigraphy	Core Image	Test Sections	Description
		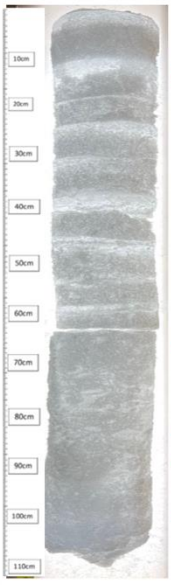	14/01/D4	Multiple small ice lenses to choose from in this sample, this allowed largest room for error when preparing sample.
			C14-1	Mixed section with ice lenses
			D14-1	Compression and density tests performed on large ice free bottom layers.

2021/2022 Antarctic Ice Core logging	Core Number	Coordinates	-70,2575S -2,6999W
		Shelf Region	E4
	15	Length	≈108cm
		Set temp.	- 20 degrees C
		Actual temp.	-20 +- 2 degrees C

Lens location	Stratigraphy	Core Image	Test Sections	Description
		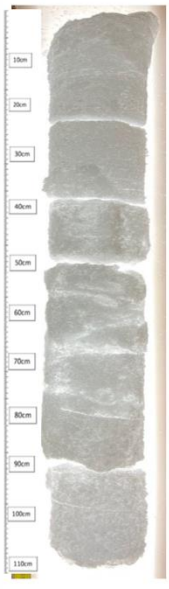	15/01/D4	Thin section analysis performed in center of very large ice lens, interesting to observe the size of c-axis within the sample.
			D15-1	
			D15-2	

2021/2022 Antarctic Ice Core logging	Core Number	Coordinates	-70,2577S -2,6999W
		Shelf Region	E4
	16	Length	≈117cm
		Set temp.	- 20 degrees C
		Actual temp.	-20 +- 2 degrees C

Lens location	Stratigraphy	Core Image	Test Sections	Description
		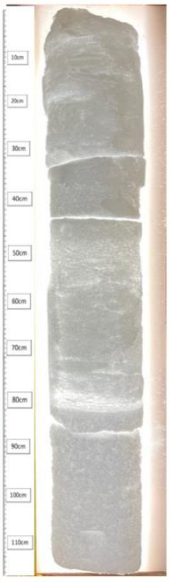	C16-1 C16-2 C16-3 C16-4	Ice lenses with fine grains within

2021/2022 Antarctic Ice Core logging	Core Number	Coordinates	-70,2578S -2,6997W
		Shelf Region	E4
	17	Length	≈101cm
		Set temp.	- 20 degrees C
		Actual temp.	-20 +- 2 degrees C

Lens location	Stratigraphy	Core Image	Test Sections	Description
		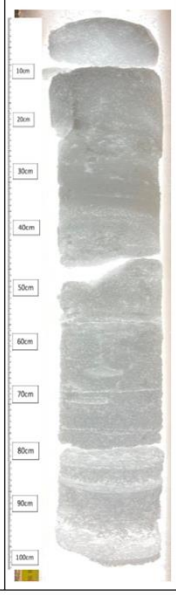	C17-1 C17-2	

2021/2022 Antarctic Ice Core logging	Core Number	Coordinates	-70,2562S -2,6990W
		Shelf Region	B4
	18	Length	≈114cm
		Set temp.	- 20 degrees C
		Actual temp.	-20 +- 2 degrees C

Lens location	Stratigraphy	Core Image	Test Sections	Description
		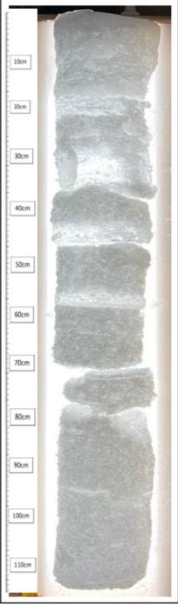		

2021/2022 Antarctic Ice Core logging	Core Number	Coordinates	-70,2568S -2,6992W
		Shelf Region	C4
	19	Length	≈119cm
		Set temp.	- 20 degrees C
		Actual temp.	-20 +- 2 degrees C

Lens location	Stratigraphy	Core Image	Test Sections	Description
		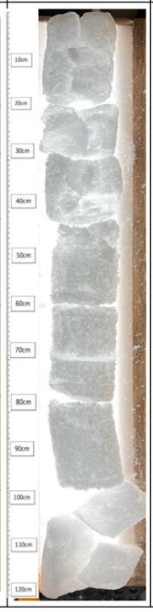		

2021/2022 Antarctic Ice Core logging	Core Number	Coordinates	-70,2575S	-2,6993W
		Shelf Region	D4	
	20	Length	≈105cm	
		Set temp.	- 20 degrees C	
		Actual temp.	-20 +- 2 degrees C	

Lens location	Stratigraphy	Core Image	Test Sections	Description
		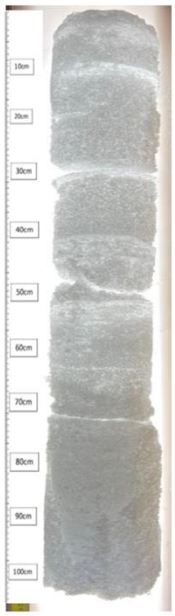	C20-2	Compression on a mixed sample of sufficient height
			C20-1	Compression test performed on thick deep snow sample.

2021/2022 Antarctic Ice Core logging	Core Number	Coordinates	-70,2578S	-2,6991W
		Shelf Region	E4	
	21	Length	≈120cm	
		Set temp.	- 20 degrees C	
		Actual temp.	-20 +- 2 degrees C	

Lens location	Stratigraphy	Core Image	Test Sections	Description
		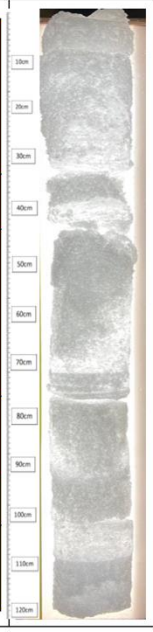		

2021/2022 Antarctic Ice Core logging	Core Number	Coordinates	-70,2561S	-2,6986W
		Shelf Region	B5	
	22	Length	≈112cm	
		Set temp.	- 20 degrees C	
		Actual temp.	-20 +- 2 degrees C	

Lens location	Stratigraphy	Core Image	Test Sections	Description
		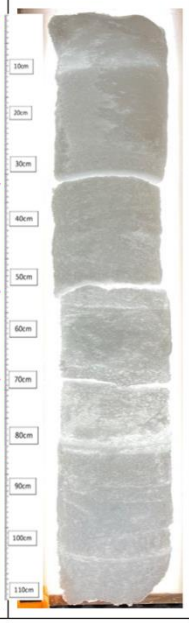		

2021/2022 Antarctic Ice Core logging	Core Number	Coordinates	-70,2577S	-2,6987W
		Shelf Region	E5	
	23	Length	≈110cm	
		Set temp.	- 20 degrees C	
		Actual temp.	-20 +- 2 degrees C	

Lens location	Stratigraphy	Core Image	Test Sections	Description
		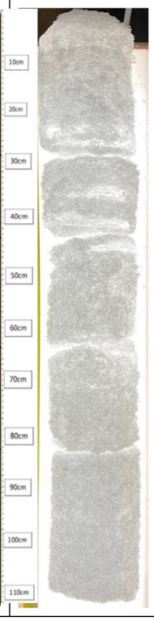	C23-1	

2021/2022 Antarctic Ice Core logging	Core Number	Coordinates	-70,2565S	-2,6983W
		Shelf Region	B5	
	24	Length	≈120cm	
		Set temp.	- 20 degrees C	
		Actual temp.	-20 +- 2 degrees C	

Lens location	Stratigraphy	Core Image	Test Sections	Description
		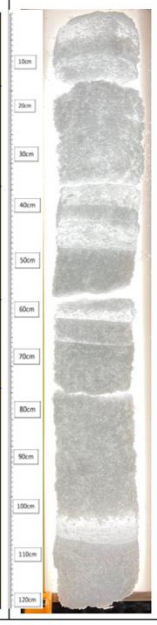	C24-1	

2021/2022 Antarctic Ice Core logging	Core Number	Coordinates	-70,2571S	-2,6982W
		Shelf Region	D5	
	26	Length	≈107cm	
		Set temp.	- 20 degrees C	
		Actual temp.	-20 +- 2 degrees C	

Lens location	Stratigraphy	Core Image	Test Sections	Description
		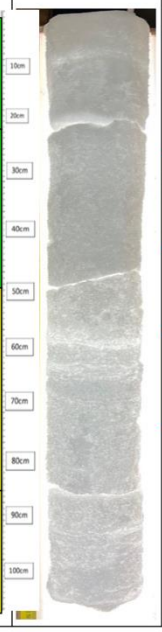	C26-1 C26-2	Mixed section of sufficent compression height

2021/2022 Antarctic Ice Core logging	Core Number	Coordinates	-70,2559S	-2,6980W
		Shelf Region	A5	
	28	Length	≈117cm	
		Set temp.	- 20 degrees C	
		Actual temp.	-20 +- 2 degrees C	

Lens location	Stratigraphy	Core Image	Test Sections	Description
		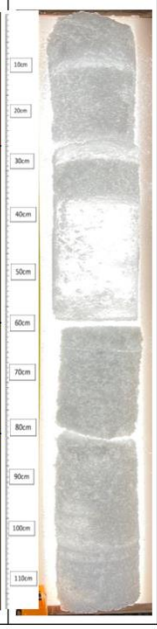	28/01/A5 C28-1 C28-2	One of the most dense ice lenses using the initial visual test, will be very interesting to observe crystallography and if there is a large compression value. Compression test done on uniform highly granular sample at the bottom of the sample as a reference for high value above.

2021/2022 Antarctic Ice Core logging	Core Number	Coordinates	-70,2562S	-2,6980W
		Shelf Region	B5	
	29	Length	≈122cm	
		Set temp.	- 20 degrees C	
		Actual temp.	-20 +- 2 degrees C	

Lens location	Stratigraphy	Core Image	Test Sections	Description
		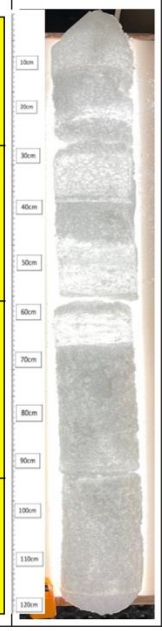		

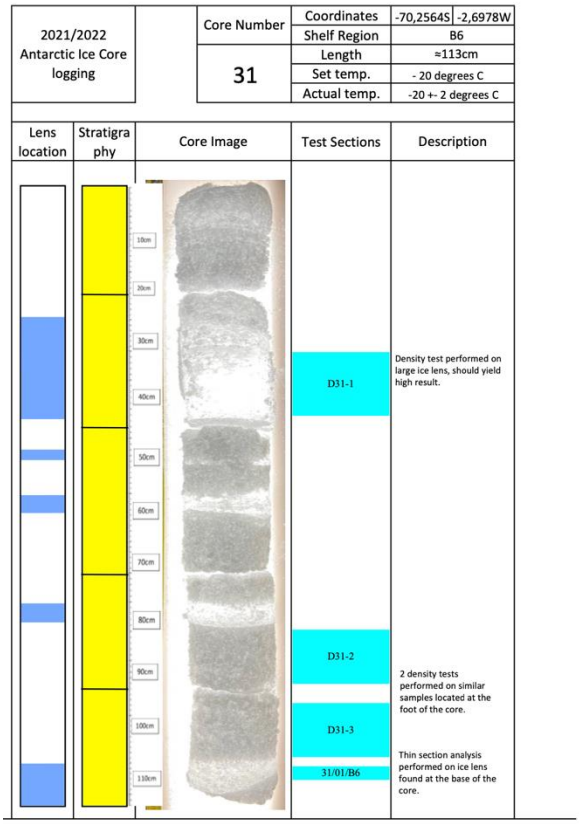
2021/2022 Antarctic Ice Core logging
Core Number
31
Coordinates -70,2564S -2,6978W
Shelf Region B6
Length ≈113cm
Set temp. - 20 degrees C
Actual temp. -20 +- 2 degrees C
Lens location
Stratigra phy
Core Image
Test Sections
Description
D31-1
Density test performed on large ice lens, should yield high result.
D31-2
D31-3
2 density tests performed on similar samples located at the foot of the core.
31/01/B6
Thin section analysis performed on ice lens found at the base of the core.

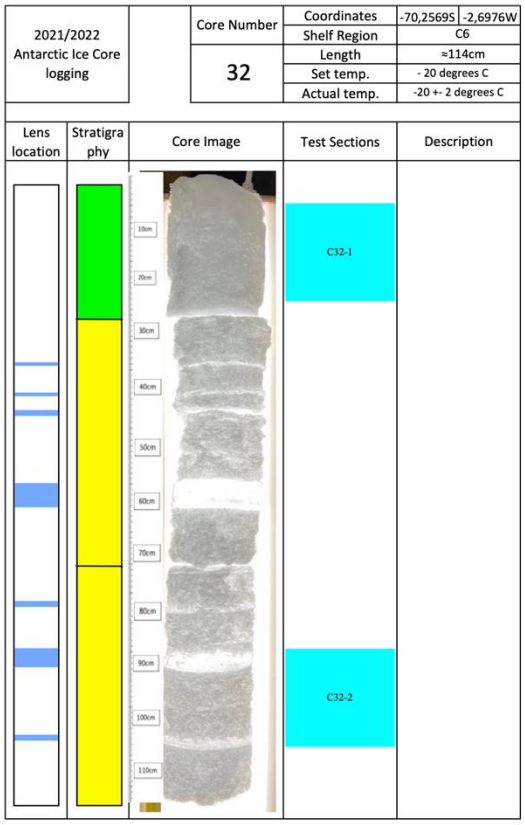
2021/2022 Antarctic Ice Core logging
Core Number
32
Coordinates -70,2569S -2,6976W
Shelf Region C6
Length ≈114cm
Set temp. - 20 degrees C
Actual temp. -20 +- 2 degrees C
Lens location
Stratigra phy
Core Image
Test Sections
Description
C32-1
C32-2

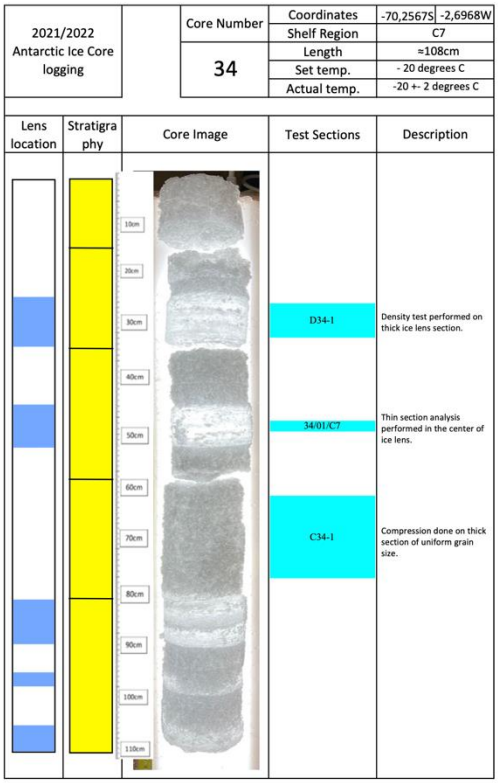
2021/2022 Antarctic Ice Core logging
Core Number
34
Coordinates -70,2567S -2,6968W
Shelf Region C7
Length ≈108cm
Set temp. - 20 degrees C
Actual temp. -20 +- 2 degrees C
Lens location
Stratigra phy
Core Image
Test Sections
Description
D34-1
Density test performed on thick ice lens section.
34/01/C7
Thin section analysis performed in the center of ice lens.
C34-1
Compression done on thick section of uniform grain size.

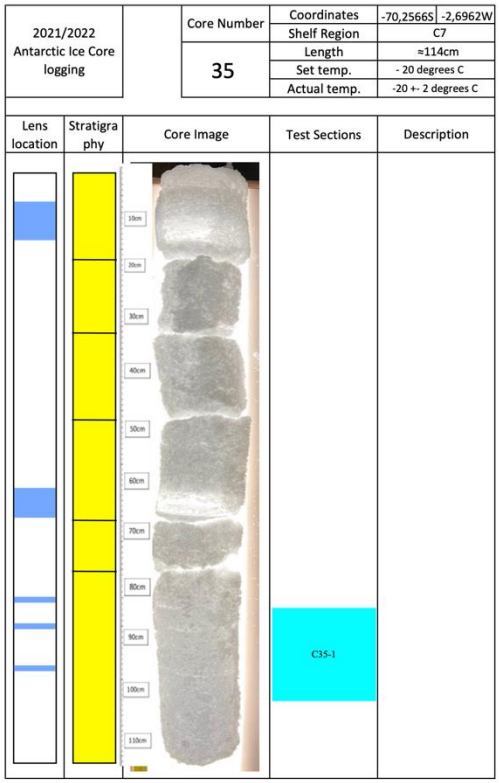
2021/2022 Antarctic Ice Core logging
Core Number
35
Coordinates -70,2566S -2,6962W
Shelf Region C7
Length ≈114cm
Set temp. - 20 degrees C
Actual temp. -20 +- 2 degrees C
Lens location
Stratigra phy
Core Image
Test Sections
Description
C35-1

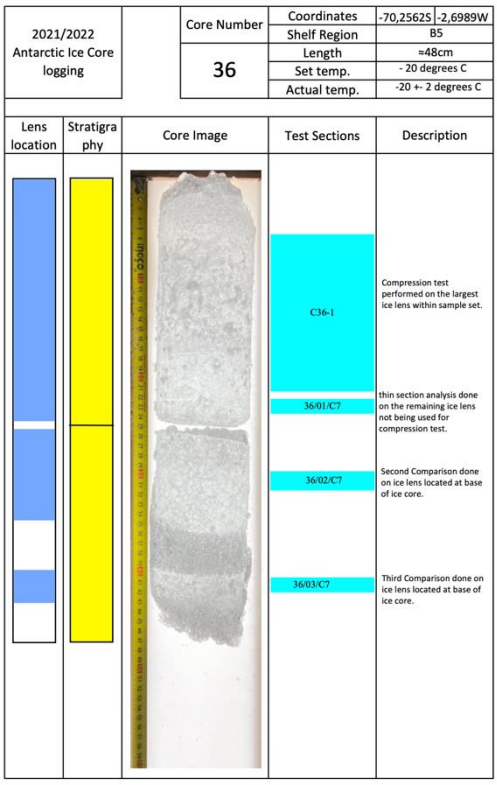
2021/2022 Antarctic Ice Core logging
Core Number
36
Coordinates
-70,2562S -2,6989W
Shelf Region
B5
Length
≈48cm
Set temp.
- 20 degrees C
Actual temp.
-20 +- 2 degrees C
Lens location
Stratigra phy
Core Image
Test Sections
Description
C36-1
Compression test performed on the largest ice lens within sample set.
36/01/C7
thin section analysis done on the remaining ice lens not being used for compression test.
36/02/C7
Second Comparison done on ice lens located at base of ice core.
36/03/C7
Third Comparison done on ice lens located at base of ice core.

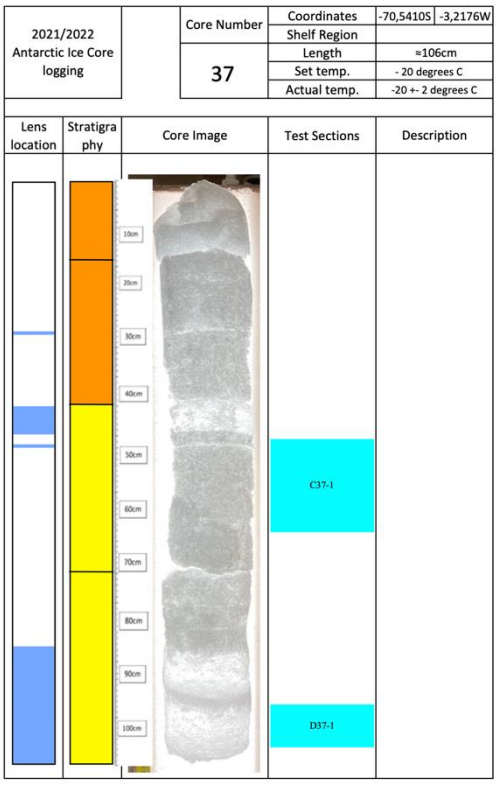
2021/2022 Antarctic Ice Core logging
Core Number
37
Coordinates
-70,5410S -3,2176W
Shelf Region
Length
≈106cm
Set temp.
- 20 degrees C
Actual temp.
-20 +- 2 degrees C
Lens location
Stratigra phy
Core Image
Test Sections
Description
C37-1
D37-1

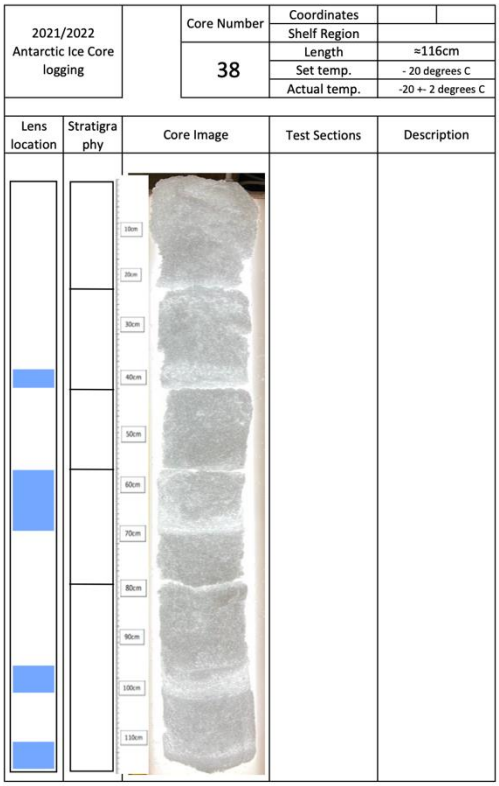
2021/2022 Antarctic Ice Core logging
Core Number
38
Coordinates
Shelf Region
Length
≈116cm
Set temp.
- 20 degrees C
Actual temp.
-20 +- 2 degrees C
Lens location
Stratigra phy
Core Image
Test Sections
Description

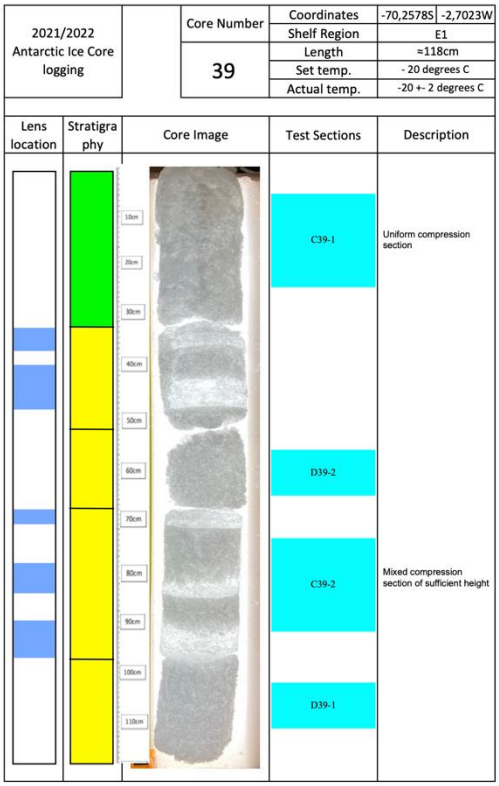
2021/2022 Antarctic Ice Core logging
Core Number
39
Coordinates
-70,2578S -2,7023W
Shelf Region
E1
Length
≈118cm
Set temp.
- 20 degrees C
Actual temp.
-20 +- 2 degrees C
Lens location
Stratigra phy
Core Image
Test Sections
Description
C39-1
Uniform compression section
D39-2
C39-2
Mixed compression section of sufficient height
D39-1

Appendix B – SolidWorks drawings

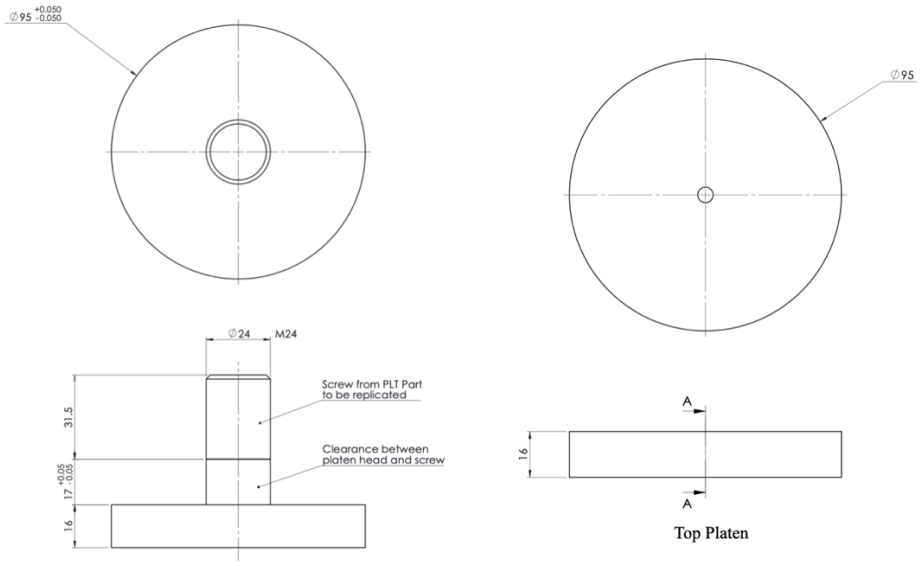

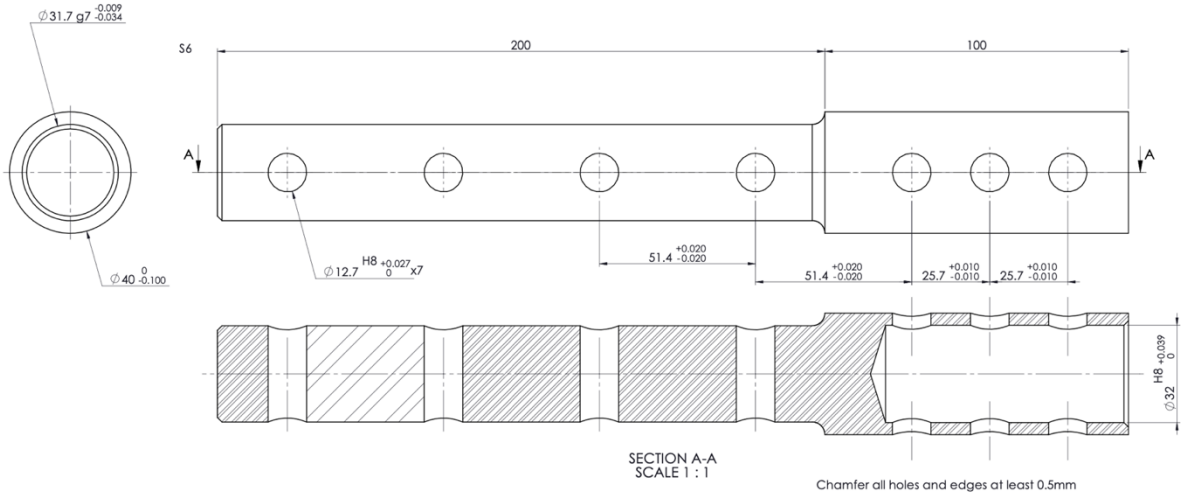

Pole Extension

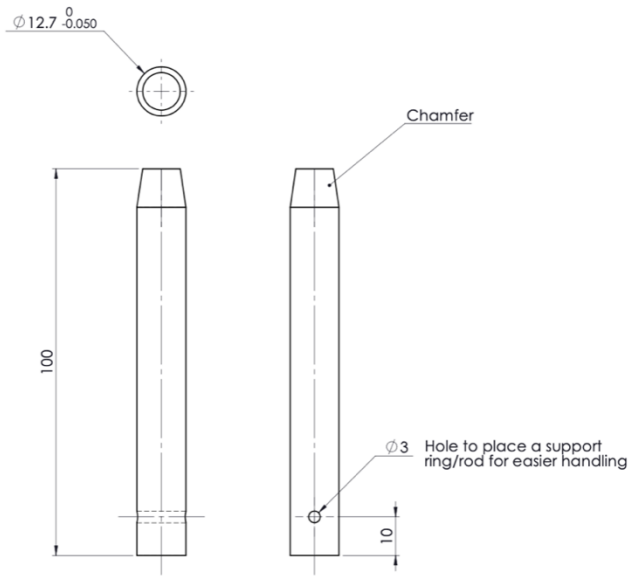

Fastening Pins

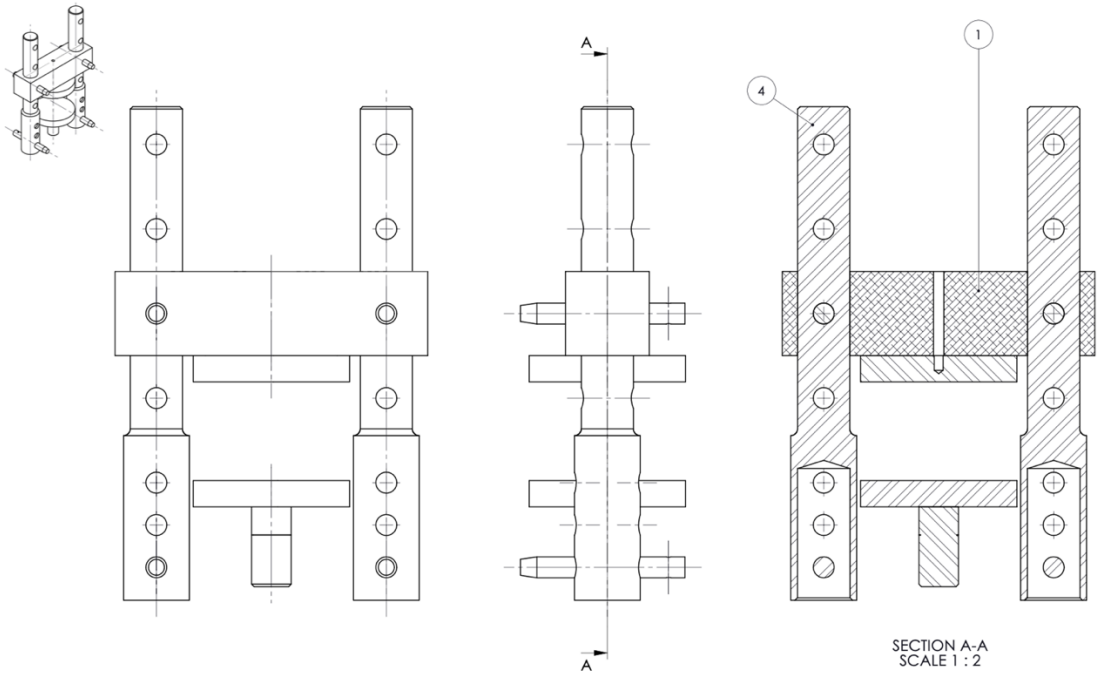

Assembly

Appendix C – Result tables

Core Coordinates

Core Number	Latitude	Longitude
1	-70.2578	-2.7023
2	-70.2578	-2.7022
3	-70.2571	-2.7019
4	-70.2581	-2.7016
5	-70.2569	-2.7013
6	-70.2573	-2.7012
7	-70.2572	-2.7009
8	-70.2568	-2.7005
9	-70.2576	-2.7006
10	-70.2565	-2.7001
11	-70.2565	-2.7000
12	-70.2566	-2.6999
13	-70.2572	-2.7002
14	-70.2573	-2.6998
15	-70.2575	-2.6999
16	-70.2577	-2.6999
17	-70.2578	-2.6997
18	-70.2562	-2.6990
19	-70.2568	-2.6992
20	-70.2575	-2.6993
21	-70.2578	-2.6991
22	-70.2561	-2.6986
23	-70.2577	-2.6987
24	-70.2565	-2.6983
25	-70.2566	-2.6982
26	-70.2571	-2.6982
27	-70.2573	-2.6982
28	-70.2559	-2.6980
29	-70.2562	-2.6980
30	-70.2563	-2.6979
31	-70.2564	-2.6978
32	-70.2569	-2.6976
33	-70.2562	-2.6971
34	-70.2567	-2.6968
35	-70.2566	-2.6962

Ice lens percentages

Core	Length (mm)	Lens length (mm)	Lens % (%)
1	1000	90	9.0
2	1000	170	17.0
3	1100	30	2.7
4	1100	370	33.6
5	1100	140	12.7
6	1100	110	10.0
7	1100	55	5.0
8	1100	50	4.5
8b	1100	110	10.0
9	1100	175	15.9
10	1120	20	1.8
11	1100	40	3.6
12	1100	40	3.6
13	1100	120	10.9
13b	1000	130	13.0
14	1000	140	14.0
15	1100	20	1.8
16	1000	30	3.0
17	1000	70	7.0
18	1100	150	13.6
19	1100	80	7.3
20	1000	70	7.0
21	1150	260	22.6
22	1100	40	3.6
23	1100	70	6.4
24	1100	120	10.9
26	1000	0	0.0
28	1100	260	23.6
29	1100	200	18.2
31	1100	220	20.0
32	1100	90	8.2
34	1000	260	26.0
35	1100	70	6.4
36	450	400	88.9
37	1000	180	18.0
38	1100	80	7.3
39	1100	165	15.0

		Grainsize percentages					
		Fine grained		**Medium grained**		**Large grained**	
Core	**Length (mm)**	**Length (mm)**	**(%)**	**Length (mm)**	**(%)**	**Length (mm)**	**(%)**
1	1000	200	20.0	800	80.0	0	0.0
2	1000	310	31.0	210	21.0	480	48.0
3	1100	560	50.9	540	49.1	0	0.0
4	1100	180	16.4	470	42.7	450	40.9
5	1100	440	40.0	660	60.0	0	0.0
6	1100	0	0.0	1100	100.0	0	0.0
7	1100	600	54.5	500	45.5	0	0.0
8	1100	80	7.3	690	62.7	330	30.0
8b	1100	80	7.3	420	38.2	600	54.5
9	1100	0	0.0	1100	100.0	0	0.0
10	1120	0	0.0	530	47.3	590	52.7
11	1100	0	0.0	490	44.5	610	55.5
12	1100	710	64.5	390	35.5	0	0.0
13	1100	0	0.0	340	30.9	760	69.1
13b	1000	0	0.0	1000	100.0	0	0.0
14	1000	0	0.0	1000	100.0	0	0.0
15	1100	770	70.0	330	30.0	0	0.0
16	1000	1000	100.0	0	0.0	0	0.0
17	1000	200	20.0	800	80.0	0	0.0
18	1100	500	45.5	380	34.5	220	20.0
19	1100	0	0.0	380	34.5	720	65.5
20	1000	0	0.0	720	72.0	280	28.0
21	1150	0	0.0	230	20.0	920	80.0
22	1100	830	75.5	270	24.5	0	0.0
23	1100	0	0.0	610	55.5	490	44.5
24	1100	0	0.0	1100	100.0	0	0.0
26	1000	500	50.0	500	50.0	0	0.0
28	1100	0	0.0	940	85.5	160	14.5
29	1100	0	0.0	1100	100.0	0	0.0
31	1100	0	0.0	1100	100.0	0	0.0
32	1100	270	24.5	830	75.5	0	0.0
34	1000	0	0.0	1000	100.0	0	0.0
35	1100	0	0.0	1100	100.0	0	0.0
36	450	0	0.0	450	100.0	0	0.0
37	1000	0	0.0	580	58.0	420	42.0
38	1100	330	30.0	770	70.0	0	0.0

Density Readings

Core	Sample	Density	Core	Sample	Density
27	C27-1	478.15	6	D6-2	472.80
36	C36-1	860.34	12	C12-1	393.01
5	D5-A	642.30	12	D12-1	408.97
5	D5-B	721.22	14	C14-1	585.13
5	D5-D	474.32	14	D14-1	624.53
5	D5-E	458.03	15	D15-1	733.56
9	C9-1	467.62	15	D15-2	359.74
9	D9-2	530.05	20	C20-1	472.78
1	C1-1	471.99	37	D37-1	838.25
1	D1-1	538.31	28	C28-1	892.80
4	D4-1	896.21	31	D31-1	883.05
4	D4-2	881.20	31	D31-2	418.75
4	C4-1	457.39	31	D31-3	462.54
2	C2-1	449.83	3	C3-1	508.82
2	C2-2	770.90	20	C20-2	522.63
10	D10-1	525.73	13	C13-2	567.13
10	D10-2	448.74	16	C16-1	501.84
7	C7-1	517.90	16	C16-2	642.51
7	C7-2	529.62	16	C16-3	605.03
7	D7-1	520.36	16	C16-4	407.25
37	C37-1	430.08	39	C39-1	546.76
34	C34-1	469.56	39	C39-2	646.36
34	D34-1	868.74	12	C12-2	401.83
11	C11-1	406.19	17	C17-1	577.26
11	C11-2	510.65	17	C17-2	551.35
13	C13-1	563.73	23	C23-1	463.12
13	D13-1	840.30	24	C24-1	416.86
13	D13-2	611.36	26	C26-1	424.79
8	C8-1	417.90	26	C26-2	490.76
8	D8-1	419.08	32	C32-1	539.16
8	D8-2	863.45	32	C32-2	554.66
8B	D8b-1	815.92	35	C35-1	568.36
8B	C8b-1	387.07	6	D6-1	888.14

RQD

Core	Length (cm)	Sum >10 (cm)	RQD (%)
1	110	51	46
2	105	83	79
3	113	105	93
4	120	95	79
5	110	98	89
6	114	104	91
7	115	103	90
8a	115	103	90
8b	115	104	90
9	109	90	83
10	115	81	70
11	111	86	77
12	112	93	83
13	110	66	60
13b	110	67	61
14	107	46	43
15	108	107	99
16	115	115	100
17	100	66	66
18	112	92	82
19	120	113	94
20	105	75	71
21	120	89	74
22	113	93	82
23	110	72	65
24	120	94	78
26	105	78	74
28	115	94	82
29	121	112	93
31	110	87	79
32	114	67	59
34	110	74	67
35	112	78	70
36	43	24	56
37	105	97	92
38	112	91	81
39	115	72	63
N	113	60	53

Ultrasound tests

Core	Sample	Density (kg/m3)	V_p (m/s)	V_s (m/s)	M (GPa)	G (GPa)	v	E (GPa)
1	C1-1	651.5	3354	979	7.33	0.62	0.45	1.82
1	C1-2	639.0	2847	780	5.18	0.39	0.46	1.13
39	C39-1	546.7	2738	1640	4.10	1.47	0.22	3.59
39	C39-2	646.3	2829	988	5.17	0.63	0.43	1.81
7	C7-1	499.0	2579	1403	3.32	0.98	0.29	2.53
7	C7-2	521.0	2520	1270	3.31	0.84	0.33	2.23
8	C8a-1	417.6	2176	855	1.98	0.31	0.41	0.86
8	C8b-1	380.4	2245	737	1.92	0.21	0.44	0.59
9	C9-1	460.9	2480	1147	2.83	0.61	0.36	1.65
3	C3-1	508.8	2938	1578	4.39	1.27	0.30	3.29
20	C20-1	461.3	2088	1148	2.01	0.61	0.28	1.56
20	C20-2	522.7	2055	885	2.21	0.41	0.39	1.13
13	C13-1	560.2	2946	990	4.86	0.55	0.44	1.58
13	C13-2	567.2	2541	865	3.66	0.42	0.43	1.22
16	C16-1	501.8	1980	910	1.97	0.42	0.37	1.14
16	C16-2	642.6	2885	1298	5.35	1.08	0.37	2.97
16	C16-3	606.5	2460	1090	3.67	0.72	0.38	1.99
16	C16-4	407.2	1957	799	1.56	0.26	0.40	0.73
11	C11-2	485.6	2767	1233	3.72	0.74	0.38	2.03
12	C12-1	385.1	1855	751	1.33	0.22	0.40	0.61
12	C12-2	401.9	1968	872	1.56	0.31	0.38	0.84
17	C17-1	577.3	2700	1583	4.21	1.45	0.24	3.58
17	C17-2	551.3	2553	1198	3.59	0.79	0.36	2.15
23	C23-1	463.1	1930	808	1.72	0.30	0.39	0.84
24	C24-1	416.9	2129	712	1.89	0.21	0.44	0.61
26	C26-1	424.8	1948	830	1.61	0.29	0.39	0.81
26	C26-2	490.7	1852	983	1.68	0.47	0.30	1.24
32	C32-1	539.1	2701	1047	3.93	0.59	0.41	1.67
32	C32-2	554.7	2169	928	2.61	0.48	0.39	1.33
35	C35-1	568.4	2753	1211	4.31	0.83	0.38	2.30

UCS

Core	Sample	Area (mm^2)	F (kN)	σ (MPa)
1	C1-1	5726.69	4.2	0.73
1	C1-2	5883.34	2.2	0.37
39	C39-1	6402.79	7.1	1.11
39	C39-2	6042.10	7.14	1.18
7	C7-1	6425.50	8.17	1.27
7	C7-2	6225.33	7.16	1.15
8	C8a-1	5849.40	3.24	0.55
8	C8b-1	5948.78	4.18	0.70
9	C9-1	5961.09	5.07	0.85
3	C3-1	6083.51	6.47	1.06
20	C20-1	6205.77	4.76	0.77
20	C20-2	6309.53	5.06	0.80
13	C13-1	6075.21	7.8	1.28
13	C13-2	6050.37	5.85	0.97
16	C16-1	6282.80	4.48	0.71
16	C16-2	6256.14	8.3	1.33
16	C16-3	6360.31	6.39	1.00
16	C16-4	6002.21	3.75	0.62
11	C11-2	6053.13	6.02	0.99
12	C12-1	6469.62	3.23	0.50
12	C12-2	6422.66	3.94	0.61
17	C17-1	6225.33	7.91	1.27
17	C17-2	6228.13	8.28	1.33
23	C23-1	5987.12	5.63	0.94
24	C24-1	6233.73	3.62	0.58
26	C26-1	5973.41	3.22	0.54
26	C26-2	6183.45	5.53	0.89
32	C32-1	6343.36	5.94	0.94
32	C32-2	6187.63	6.01	0.97
35	C35-1	6469.62	6.27	0.97

Strain rate

Core	Sample	h_i (mm)	h_f (mm)	t (s)	ΔL (mm)	L (mm)	$\dot{\varepsilon}$	$\Delta\dot{\varepsilon}$
1	C1-1	30.4	33	300	2.6	140.71	0.0185	6.159E-05
1	C1-2	53.86	58.84	300	4.98	175.02	0.0285	9.485E-05
39	C39-1	50.2	55.7	340	5.5	179.37	0.0307	9.018E-05
39	C39-2	50.2	53.52	320	3.32	179.92	0.0185	5.766E-05
7	C7-1	50.6	56.1	400	5.5	180.59	0.0305	7.614E-05
7	C7-2	50	54.32	400	4.32	180.15	0.0240	5.995E-05
8	C8a-1	60.24	64.3	150	4.06	170.29	0.0238	1.589E-04
8	C8b-1	47.8	53.62	400	5.82	181.95	0.0320	7.997E-05
9	C9-1	46.92	50.62	400	3.7	178.29	0.0208	5.188E-05
3	C3-1	48.11	51.8	400	3.69	183.22	0.0201	5.035E-05
20	C20-1	42.36	46.82	400	4.46	188.47	0.0237	5.916E-05
20	C20-2	50.28	53.52	400	3.24	180.45	0.0180	4.489E-05
13	C13-1	60.88	65.72	500	4.84	171.12	0.0283	5.657E-05
13	C13-2	50.66	53.5	400	2.84	179.48	0.0158	3.956E-05
16	C16-1	47.46	51.01	400	3.55	182.53	0.0194	4.862E-05
16	C16-2	51	54.24	500	3.24	179.95	0.0180	3.601E-05
16	C16-3	47.64	49.52	500	1.88	182.36	0.0103	2.062E-05
16	C16-4	47.46	51.34	400	3.88	183.36	0.0212	5.290E-05
11	C11-2	65.14	68	240	2.86	165.63	0.0173	7.195E-05
12	C12-1	41	48.72	500	7.72	189.17	0.0408	8.162E-05
12	C12-2	56.12	60	400	3.88	175.71	0.0221	5.520E-05
17	C17-1	47	53.1	500	6.1	183.09	0.0333	6.663E-05
17	C17-2	51.2	54.4	500	3.2	179.83	0.0178	3.559E-05
23	C23-1	48.5	51.7	400	3.2	182.43	0.0175	4.385E-05
24	C24-1	43.82	46.58	400	2.76	187.05	0.0148	3.689E-05
26	C26-1	49.72	52.92	400	3.2	180.72	0.0177	4.427E-05
26	C26-2	48.48	51.3	500	2.82	181.59	0.0155	3.106E-05
32	C32-1	49.18	52.68	400	3.5	180.51	0.0194	4.847E-05
32	C32-2	50.87	53.1	400	2.23	180.21	0.0124	3.094E-05
35	C35-1	48	50.4	400	2.4	180.63	0.0133	3.322E-05

Appendix D – Ethics clearance

Application for Approval of Ethics in Research (EiR) Projects
Faculty of Engineering and the Built Environment, University of Cape Town

ETHICS APPLICATION FORM

Please Note:
Any person planning to undertake research in the Faculty of Engineering and the Built Environment (EBE) at the University of Cape Town is required to complete this form **before** collecting or analysing data. The objective of submitting this application *prior* to embarking on research is to ensure that the highest ethical standards in research, conducted under the auspices of the EBE Faculty, are met. Please ensure that you have read, and understood the **EBE Ethics in Research Handbook** (available from the UCT EBE, Research Ethics website) prior to completing this application form: http://www.ebe.uct.ac.za/ebe/research/ethics1

APPLICANT'S DETAILS		
Name of principal researcher, student or external applicant		Jonathan Arthur Olivu Econi
Department		Department of Civil Engineering
Preferred email address of applicant:		econi.arthur.7@gmail.com
If Student	Your Degree: e.g., MSc, PhD, etc.	MSc in Engineering specialising in Geotechnical Engineering
	Credit Value of Research: e.g., 60/120/180/360 etc.	120
	Name of Supervisor (if supervised):	Prof. Denis Kalumba
If this is a researchcontract, indicate the source of funding/sponsorship		N/A
Project Title		Slope Stability Analysis of the Fimbul Ice Shelf, Antarctica.

I hereby undertake to carry out my research in such a way that:

- there is no apparent legal objection to the nature or the method of research; and
- the research will not compromise staff or students or the other responsibilities of the University;
- the stated objective will be achieved, and the findings will have a high degree of validity;
- limitations and alternative interpretations will be considered;
- the findings could be subject to peer review and publicly available; and
- I will comply with the conventions of copyright and avoid any practice that would constitute plagiarism.

APPLICATION BY	Full name	Signature	Date
Principal Researcher/ Student/External applicant	Jonathan Arthur Olivu Econi		17/03/2021
SUPPORTED BY	Full name	Signature	Date
Supervisor (where applicable)	Denis Kalumba		17.03.2021

APPROVED BY	Full name	Signature	Date
HOD (or delegated nominee) Final authority for all applicants who have answered NO to all questions in Section 1; and for all Undergraduate research (Including Honours).	Alphose Zingoni		02.04.2021
Chair: Faculty EIR Committee For applicants other than undergraduate students who have answered YES to any of the questions in Section 1.			